Characterization of Nanoscale Junctions in Carbon Nanotubes and Graphene for Novel Device Applications

by

Chang-Hua Liu

A dissertation submitted in partial fulfillment
of the requirements for the degree of
Doctor of Philosophy
(Electrical Engineering)
in The University of Michigan
2014

Doctoral Committee:

Assistant Professor Zhaohui Zhong, Chair
Professor L. Jay Guo
Professor Nicholas A. Kotov
Professor Theodore B. Norris

Dedicated To My Family

Acknowledgements

The completion of my graduate degree has been a long but amazing journey that has included numerous fantastic learning experiences and has been a sustained period of intensive intellectual growth. I am privileged to complete this journey in the wonderful academic environment of Ann Arbor. I am also grateful to have many people in my life who continuously supported me throughout these years. Without your encouragement, writing this dissertation would not have been possible.

At UMich, I would like to first express my sincerest gratitude to my advisor, Prof. Zhaohui Zhong, for the opportunity to work with him. I appreciate the enormous freedom that he allowed me in exploring different research projects and determining my research interests during my Ph.D. studies. Whenever I encountered obstacles, his intuitive insights always led me in the right direction; his encouragement always reinvigorated my enthusiasm for research. In addition, I am continually impressed by his insights, inspirational ideas and dedication to research and teaching. He demonstrates the attitudes a researcher should possess. Additionally, I would like to thank my thesis committee, Prof. Ted Norris, Prof. Nicholas Kotov and Prof. L. Jay Guo, for their insightful comments and precious time.

I would also like to give my sincere appreciation to my lab mates, Seunghyun, Girish, Kyunghoon, Che-Hung, Kang and Rui, who are friendly and enthusiastic. I enjoyed their company and the fun times we have had over the past five years. I especially thank Chung-

Chiang, who always kindly taught me clean room processes and shared his experiences with me, and Nanditha for teaching me how to develop research plans. I also want to acknowledge my colleagues in CUOS and in the EECS department, Dr. John Nees, Cheng Zhu, Tao Ling, You-Chia, Momchil, Jessica, Dong Sun, Yi-Kuei, Chris, Chu-Hsiang, Luke, Hyunsoo and Sudarshan. I was very fortunate to know you and am glad we could share the happiness and bitterness of research life with each other. In addition, I greatly appreciate your help on my optical measurement setups and clean room processes. I would also like to thank Prof. John Hart, Dr. Yongyi, JingJing and Sameh for helping me with carbon nanotube growth, and I thank all the staff at LNF and EMAL for providing very supportive training and for keeping the facility in good condition.

Finally, and most importantly, I would like to thank my entire family and Ying-Yu. Although we have been separated by distance, I know our emotional connections have been strengthened, and I am grateful to have your endless love and spiritual encouragements throughout my life. I look forward to sharing my next journey in life with you.

Ann Arbor, December 2013

Table of Contents

List of Figures

Abstract

As materials and device architectures shrink to the nanoscale, the underlying device principles will cross over from the classical to quantum mechanical regime, which could lead to novel device behavior and provide new opportunities. In this thesis, I discuss some of the most fundamental nanoscale electronic/optoelectronic elements, including p-n, Schottky and tunneling junctions based on carbon nanotubes and graphene. By characterizing these nanoscale junctions using electrical and optical spectroscopic techniques, unconventional device operation principles were unveiled. More importantly, these fundamental understandings combined with the novel design of the device structures provided us with the ability to tailor material properties and engineer novel carbon-based optoelectronics.

First, we demonstrate a tunable diode based on a fully suspended single-walled carbon nanotube structure. The turn-on voltage of the diode under forward bias can be continuously and widely tuned by controlling gate voltages. Additionally, the same device design could be configured into a backward diode by tuning the band-to-band tunneling current in the reverse bias region. A nanotube backward diode is demonstrated for the first time with nonlinearity exceeding the ideal diode. These suggest that a tunable nanotube diode could be a unique building block for developing next generation programmable circuits.

Second, we present spatio-temporal photocurrent measurements of graphene p-n and graphene-metal junctions. The results explicitly confirm that the hot carrier photoresponse of

graphene is related to its doping level, mobility and optical excitation power. Furthermore, our photocurrent measurements reveal the formation of an ultrafast photo-Dember process in graphene. These results not only mark the first time lateral photo-Dember effect is observed in atomically thin 2D materials, but also hint at the possibility of efficient terahertz generation in graphene.

Finally, we develop a graphene-based hot carrier photodetector, which consists of a pair of graphene monolayers separated by a thin tunnel barrier. The optical illumination of this device causes hot carriers in graphene tunnel vertically to the nearby graphene layer and these pile-up photocarriers induce a strong photogating effect on the graphene channel conductance. This novel device structure and sensing scheme provide a viable route for achieving ultra-broad spectral, room temperature and high photoresponsivity photodetection.

Chapter 1

Introduction

1.1 Introduction

Optoelectronic devices have long been the subject of extensive research due to their significant impacts on every aspect of our life, including lighting, imaging, communication, energy harvesting and sensing [1-2]. To date, most optoelectronics are based on junctions within bulk bandgap semiconductors. Importantly, the development of these devices relies on the fundamental understanding obtained over the past several decades regarding light-matter interactions in bulk semiconductors. However, to achieve a high-performance device with diverse functionalities, novel photoactive materials, device architectures and device disciplines must be implemented.

In this regard, the use of nanomaterials to fabricate nanoscale devices is envisioned as a promising approach [3-8]. One of the primary reasons for miniaturization lies in better device performances, such as faster speed, less power consumption and lightweight, which have been witnessed with the constant evolution of the microelectronics industry. Another more interesting reason for miniaturization is that nanodevices may display new functionalities. As electronic or optoelectronic materials continue to shrink in size, the dimensionality of the materials is

eventually reduced. Thus, the quantum mechanical effects play the significant roles. These effects lead to unique properties of low dimensional materials that are unlike those of bulk materials in all domains, including their electrical, optical and mechanical properties. Having the capability to tailor these nanomaterials and their unique properties is essential for achieving unconventional devices.

In this thesis, our aim is to develop novel electronics and optoelectronics by exploiting the extraordinary properties of carbon based nanomaterials. In particular, we focus on utilizing one dimensional single-walled carbon nanotubes (SWNTs) and two dimensional graphene. Their remarkable electrical, optical, and mechanical properties have been the subject of intensive research since their discovery in 1991 [9] and 2004 [10] respectively. In this chapter, I will provide a brief introduction to the physical structure of carbon nanotubes (CNTs) and graphene (section 1.2), their electrical properties (sections 1.3 and 1.4) and their synthesis processes (section 1.5). This chapter concludes with a summary and outline of this thesis (section 1.6).

1.2 Physical structure of carbon nanotubes and graphene

Carbon is the sixth element in the periodic table and contains four valence electrons. It can easily bond itself or other atoms with sp, sp^2, and sp^3 hybridized orbits. The flexibility of carbon bonding yields a wide variety of organic compounds and carbon allotropes, and interestingly, differences in carbon bonding can result in distinct properties. For example, diamond, which is composed of carbon atoms stacked tightly together in a face-centered cubic sp^3 crystalline structure, is optically transparent and highly abrasive and acts as an electrical insulator and an efficient thermal conductor. Conversely, crystalline graphite, which consists of parallel sheets of sp^2 carbon atoms, is opaque, an excellent lubricant and a good electrical

conductor. In addition, the thermal conductivity between parallel carbon sheets is poor.

Furthermore, even if carbon atoms are held together with the same covalent bond, different physical structures of carbon molecules can yield different properties. This phenomenon has been witnessed since the discovery of diverse sp^2 graphitic materials, such as the 0 dimensional fullerenes, 1 dimensional CNTs and 3 dimensional graphite. Essentially, the most basic building block of these low dimensional nanomaterials is graphene, which is a flat monolayer of carbon atoms densely packed in a honeycomb crystal lattice, as illustrated in Fig. 1.1.

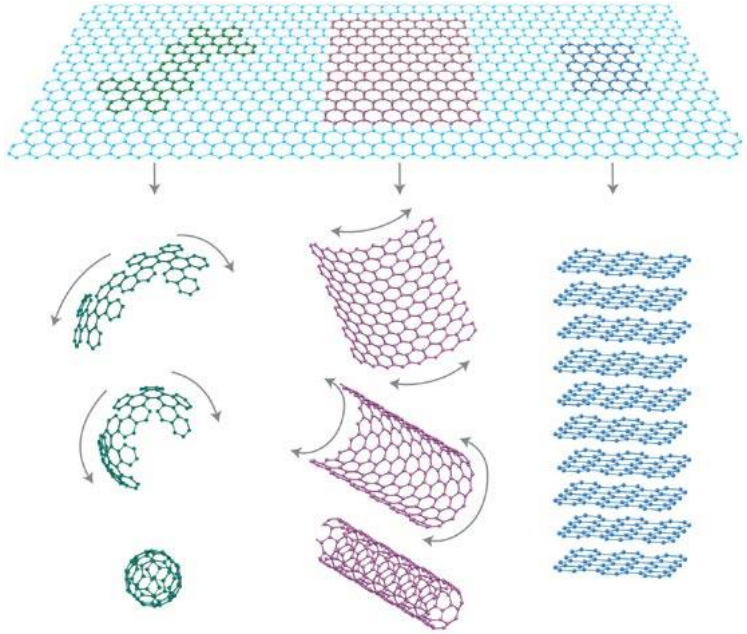

Figure 1.1 Diverse forms of sp^2 graphitic materials composed of a basic building block - graphene. Graphene can be wrapped up into 0D fullerenes, rolled into 1D CNTs or stacked into 3D graphite [11].

In particular, the atomic structure of SWNTs can differ depending on the rolling angle (chirality) of the graphene sheet, as illustrated in Fig. 1.2. By connecting two crystallographically equivalent sites A and A′, a single wall carbon nanotube (SWNT) is formed. These two sites not

only represent the circumference of the tube but also determine the chiral vector $\boldsymbol{C}_h = n\boldsymbol{a}_1 + m\boldsymbol{a}_2$, where $\boldsymbol{a}_1$ and $\boldsymbol{a}_2$ represent the unit vectors of the graphene lattice and a pair of integers, n and m, denotes the chiral numbers. Generally, if n = m, these nanotubes are called armchair CNTs, and for zigzag nanotubes, m = 0. All other chiral numbers correspond to chiral nanotubes as illustrated in Fig. 1.2. The diameter of a CNT (d_t) can be determined by the chiral vectors and can be expressed as

$$d_t = \frac{|\boldsymbol{C}_h|}{\pi} = \frac{a}{\pi}\sqrt{n^2 + nm + m^2}. \quad (1.1)$$

The chiral angle θ, which is defined by the angle between the chiral vector and the lattice vector a_1, can be calculated as follows:

$$\cos\theta = \frac{\boldsymbol{C}_h \cdot a1}{|\boldsymbol{C}_h||a1|} = \frac{2n+m}{2\sqrt{n^2+nm+m^2}}. \quad (1.2)$$

Importantly, we will see that chirality is closely related to the electronic properties of CNTs in the following sections.

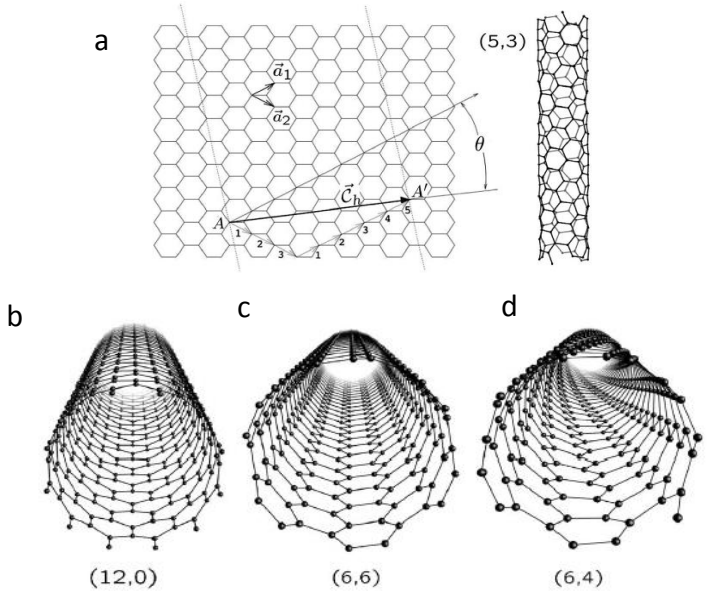

Figure 1.2 Rolling a graphene sheet into a nanotube cylinder. (a) Vector definition of graphene for converting to a (5, 3) carbon nanotube. Atomic structures of (b) zigzag, (c) armchair and (d) chiral nanotubes [12].

1.3 Electronic band structure of graphene

Because SWNTs can be visualized as seamlessly rolled-up graphene sheets, these two materials should share a similar electronic band structure. In this section, we will first describe the band structure of graphene.

As mentioned previously, graphene is a single atomic layer of sp^2-hybridized carbon arranged in a honeycomb structure. Each carbon atom contains four available valence electrons. Three of these electrons form C-C σ bonds with their nearest neighbor electrons, while the fourth electron in the $2p_z$ orbital forms π bonds extending out of the graphene plane. Because the energy of σ electrons is far below the Fermi energy, only the energy and interaction of π electrons make significant contributions to the electronic properties in the tight binding calculation. Detailed calculations are given in Wallace 1947 [13] and McClure et al. 1956 [14]. Here we give the derived energy dispersion relation:

$$E(k_x, k_y) = \pm t\sqrt{1 + 4cos^2\left(\frac{k_x a}{2}\right) + 4\,cos\left(\frac{k_x a}{2}\right)cos\left(\frac{k_y a\sqrt{3}}{2}\right)}, \quad (1.3)$$

where t = 2.5 eV is the interaction integral and a = 0.246 nm is the lattice constant of graphene. Fig. 1.3a shows the energy dispersion diagram based on equation (1.3). From this diagram, we can see that the upper conduction band (π^*) is symmetric with the lower valence band (π), and the two bands touch at the K and K' points within the graphene hexagonal first Brillouin zone, which causes graphene to have a zero bandgap with semimetal properties. In addition, the electrons have the same electronic properties as holes. More importantly, the energy-momentum relation is linear in the vicinity of the K and K' points, leading to a Dirac cone band structure (Fig. 1.3b). The energy dispersion within this Dirac cone region can be described as

$$E(k) = \pm\hbar v_F|k|, \quad (1.4)$$

where $\hbar v_F \sim 8 \times 10^5$ m/s is the Fermi velocity. This linear dispersive property leads to massless

charge carriers, analogous to the relativistic massless carriers described by the Dirac theory.

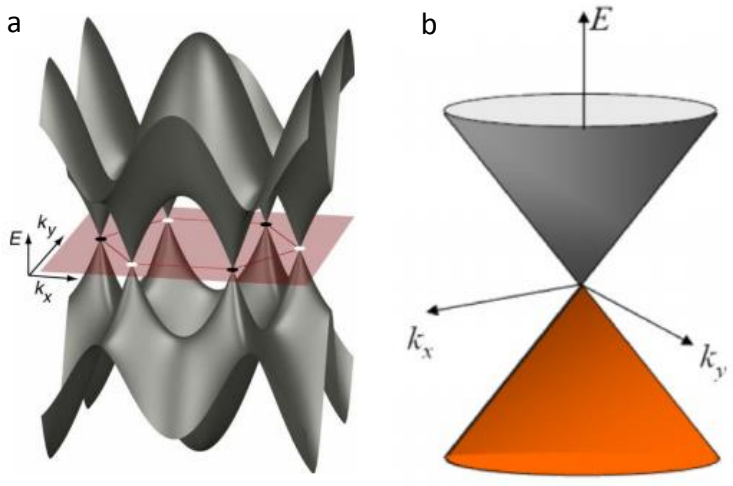

Figure 1.3 (a) Energy band structure of graphene. (b) Energy band structure in the vicinity of the Dirac point [15].

1.4 Electrical band structure of carbon nanotubes

Similarly, SWNTs should share the same electronic band structure as graphene due to their graphitic nature. However, because a SWNT can be viewed as a single sheet of graphene rolled into a cylinder of a few nanometers, additional quantization arising from electron confinement around the nanotube circumference must be considered. Thus, the energy states of SWNTs can be visualized as multiple cross-sectional planes cutting through the graphene band structure. As illustrated in Fig. 1.4a, these cross-sectional planes cut through the Dirac cone, leading to multiple allowed energy subbands. Geometrically, we can see each subband exist at the different transverse k spaces. If the cross-sectional cutting does not pass through the Dirac K or K' point, a semiconducting SWNT with bandgaps could be created (Fig. 1.4b). In contrast, metallic nanotubes should be formed if the cross-sectional cutting passes through the Dirac point (Fig. 1.4c). In fact, the intersection between the quantized energy states and the K or K' point is dependent on how the graphene sheet is rolled up into a nanotube (chirality). Based on

theoretical calculations, if n - m is not divisible by three, the SWNTs will be truly semiconducting. For SWNTs with a small bandgap, $n - m = 3i$ and i is an integer, while for metallic SWNTs, the two chiral numbers will be equal to each other ($n = m$) [16-18]. Thus, 2/3 of grown SWNTs statistically exhibit semiconductor properties, whereas the remaining 1/3 exhibit metallic properties. Theoretical calculations also indicate that the band gap energy (E_g) of a semiconducting SWNT is related to its diameter (d_t):

$$E_g = \frac{0.78\ eV}{d_t\ (nm)}. \quad (1.5)$$

This result indicates that E_g scales as $1/d_t$, which is also in good agreement with previous experimental works [19].

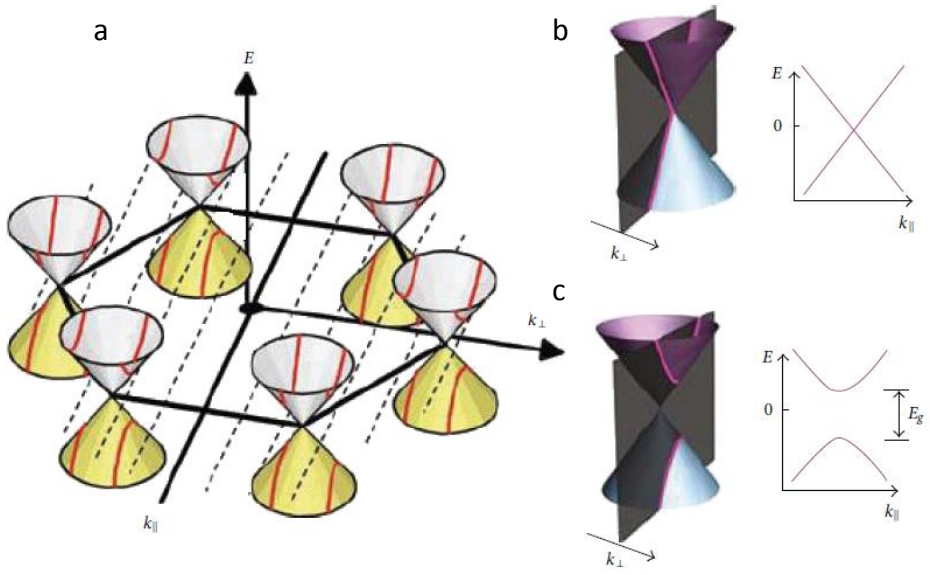

Figure 1.4 Electronic band structure of a SWNT. (a) Quantization of energy states due to electron confinement around the SWNT circumference. (b) Energy band structure of a metallic SWNT. (c) Energy band structure of a semiconducting SWNT [20].

Another important property of one dimensional materials is the presence of the Van Hove singularity [21], where the density of states (DOS) is infinite at the band gap energy. Because each SWNT has multiple energy subbands, we can see several Van Hove singularities at the band edges. Each singularity is labeled with the index of the subband (Fig. 1.5). Importantly, these prominent peaks in the DOS could favor strong optical absorption and emission transitions. Therefore, diverse optical spectroscopic techniques could be applied to characterize the electronic properties of SWNTs [22-23].

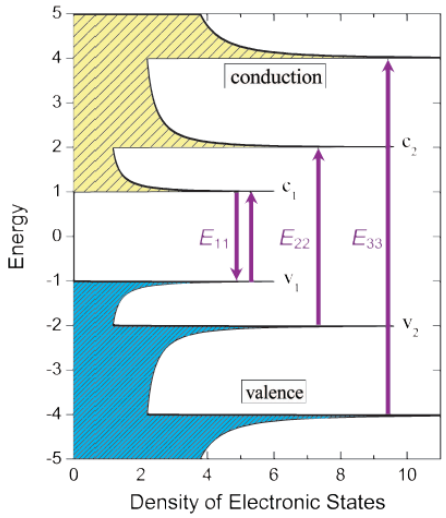

Figure 1.5 Electronic density of states in a semiconducting SWNT [24].

1.5 Synthesis of carbon nanotubes and graphene

The last decade has been an exciting period with the discovery of diverse techniques for growing carbon nanomaterials. These critical breakthroughs further motivated many efforts to investigate their material properties and growth mechanisms. However, for device applications, knowing whether the synthesized nanomaterials can be processed in a controllable manner and be compatible with existing nanofabrication techniques is important. Furthermore, high-performance nanodevices usually rely on the capability of growing high quality, high uniformity,

reproducible and large scale nanomaterials. In this thesis, we focus on using the chemical vapor deposition (CVD) method to synthesize SWNTs and graphene because this method includes several of the key advantages mentioned above. In this section, we will describe the synthesis process.

1.5.1 Carbon nanotubes synthesis

SWNTs were first discovered in 1993 [25-26], reported independently by IBM and NEC research groups. Both groups observed that the covaporization of carbon and transition metals could catalyze the formation of SWNTs, which inspired the later development of synthesis techniques. So far, three different established techniques of SWNT synthesis are frequently used: (1) arc discharge, (2) laser ablation, and (3) CVD method [27-29]. Among these synthesis techniques, CVD method provides a promising pathway for realizing CNT electronics because of its low set-up cost, high yield, and ease of scale-up. The growth mechanism of CVD method has been debated. However, it is commonly accepted that CVD is a thermal dehydrogenation reaction. By feeding transition metal catalysts (Fe, Co, Ni, Cu or Mo) with hydrocarbon vapor and inert gas at high temperature, the decomposition of carbon-containing gas causes the carbon to dissolve into catalysts. Once the catalyst reaches the carbon-solubility limit, the dissolved carbon precipitates out and forms a crystallized CNT. This precipitation process may occur either at the top or bottom of the catalyst depending on the catalyst-substrate interaction, as illustrated in Fig. 1.6. When the interaction is weak, carbon precipitation will push the catalyst out of the substrate, leading to top growth. In contrast, a strong catalyst-substrate interaction will lead to bottom growth [27].

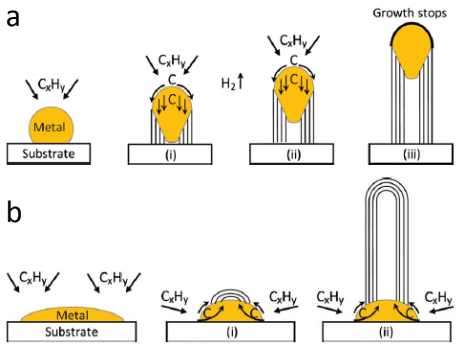

Figure 1.6 The mechanisms of CNT growth. Schematic drawing of (a) top growth and (b) bottom growth [29].

By controlling the growth conditions, CNTs synthesized using the CVD method can exist in diverse forms. For instance, a vertically aligned CNT forest has been grown on a Fe/Al_2O_3 thin film [30]. Single crystal substrates, such as quartz or sapphire, can guide CNT growth, leading to high density and horizontally aligned CNTs [31]. In addition, the synthesis of ultralong CNTs [32] and suspended CNTs [33] has been demonstrated as depicted in Fig. 1.7. All of these developments enable diverse and exciting applications in CNT-based devices.

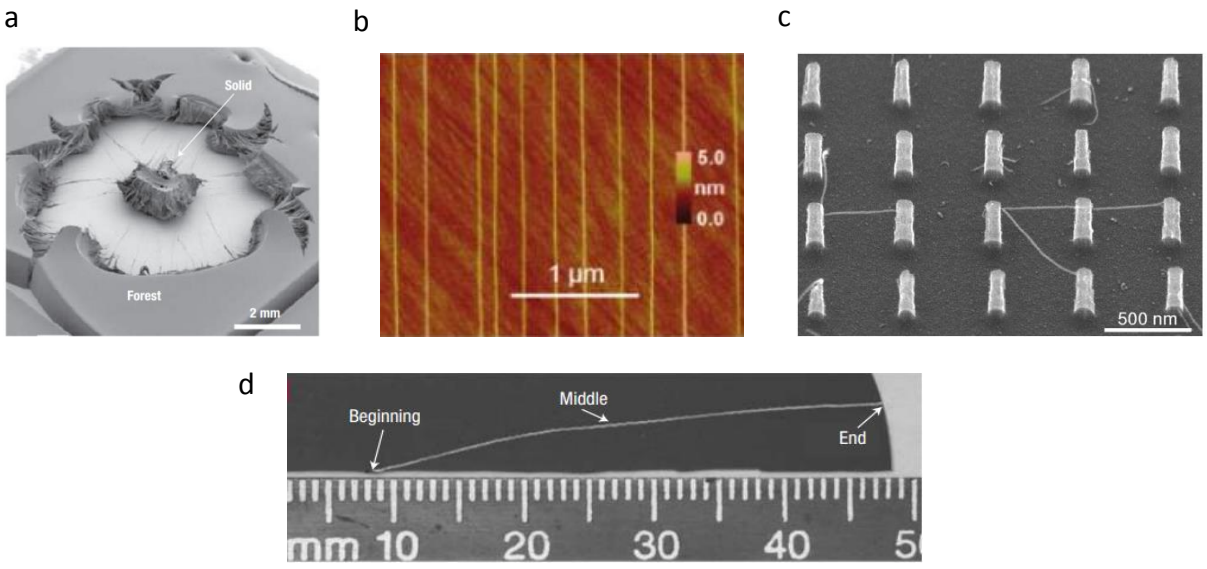

Figure 1.7 Various types of grown CNTs: (a) Vertically aligned CNT forests, (b) Horizontally aligned CNTs, (c) Suspended CNTs between pillars and (d) A centimeter ultralong CNT. [30-33]

1.5.2 Graphene synthesis

The most common methods of preparing graphene can be divided into three categories: (1) exfoliated graphene, (2) epitaxial graphene, and (3) CVD graphene [10, 34-35]. The highest quality graphene is obtained from mechanically exfoliated graphene, in which adhesive tape is utilized to repeatedly split graphite crystals into thinner flakes. However, it is very challenging to control the flake thickness, size and location, limiting industrial applications of exfoliated graphene. An alternative synthesis method is epitaxial growth, which converts silicon carbide (0001) into graphene via the sublimation of silicon atoms under a high growth temperature (~1500°C) and ultra-high vacuum. Although the epitaxial approach can produce wafer scale graphene, this method requires precise control of the growth conditions. In addition, the high cost of SiC substrates could limit the applications of epitaxial graphene. In the CVD method, graphene is synthesized by injecting carbon-containing gas and hydrogen into a furnace (~1000°C) to interact with the transition metals, e.g., Ni, Cu, Ru and Ir. The growth mechanism might vary with the used transition metals. However, for CVD growth on Cu, it is generally accepted that hydrogen initially catalyzes the metal surfaces and leads to grain growth in transition metals. After this process, the graphene starts to nucleate into several small flakes and grows along preferential crystallographic directions. Eventually, these flakes coalesce into a continuous film as the growth time is increased (Fig. 1.8) [36-37].

Among different transition metals, CVD synthesis on Cu foil is highly attractive and shows promise due to the capability of producing large scale and uniform polycrystalline graphene films (~ 95% coverage) [38-39]. In addition, the CVD method on Cu is a relatively inexpensive and readily accessible approach compared with the epitaxial method. Thus, CVD graphene is widely used for electronic and optoelectronic applications. However, graphene

grown on Cu still exhibits several considerable imperfections such as domain sizes, wrinkles and defects. These imperfections limit the performance of graphene-based devices [40-43].

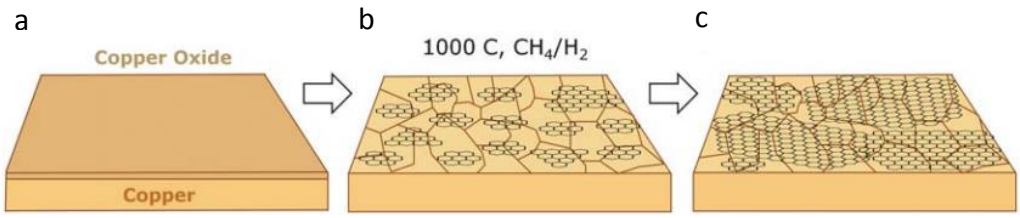

Figure 1.8 The growth mechanism of graphene on Cu. (a) Annealing of a Cu foil with native oxide in H_2 (b) Nucleation of graphene islands. (c) Coalescing of graphene flakes into a film [36].

1.6 Thesis summary and outline

In this chapter, we described the unique structures, electrical properties and the synthesis process of CNTs and graphene. Their unique properties have attracted significant interest for electronic or optoelectronic applications. In chapter 2, we will provide a full summary of recent studies on the hot carrier photoresponse in graphene and their applications. Chapter 3 will describe our experimental tools and measurement techniques for characterizing the nanoscale junctions within CNTs and graphene devices. Chapter 4 will present a novel diode based on a CNT. Our CNT diode can demonstrate fully tunable *I-V* characteristics in both forward and reverse bias regions. Chapter 5 will present our studies on the hot carrier photoresponse from graphene p-n and graphene/metal junctions. Our measurements reveal the formation of a photo-Dember field in a 2D material for the first time. In chapter 6, we will demonstrate hot carrier photodetectors based on graphene. Our proposed novel device architecture and sensing scheme can detect broad spectrum light with high responsivity at room temperature.

References:

[1] S. L. Chuang, Wiley-Interscience, New York (1995).

[2] M. A. Green, Univ. New South Wales (1998).

[3] Y. Li et al., Mater. Today 9, 18 (2006).

[4] M. Grundmann, Springer, (2002).

[5] G. Konstantatos, and E. H. Sargent, Nat. Nanotechnol. 5, 391 (2010).

[6] R. W. Kelsall, I. W. Hamley, and M. Geoghegan, Wiley-VCH, Weinheim (2005).

[7] W. Lu, and C. M. Lieber, Nat. Mater. 6, 841 (2007).

[8] G. Cao, Imperial College Press, New York (2004).

[9] S. Iijima, Nature 354, 56 (1991).

[10] K. S. Novoselov et al., Science 306, 666 (2004).

[11] A. K. Geim, and K. S. Novoselov, Nat. Mater. 6, 183 (2007).

[12] J. C. Charlier, X. Blase, and S. Roche, Rev. Mod. Phys. 79, 677 (2007).

[13] P. R. Wallace, Phys. Rev. 71, 622 (1947).

[14] J. W. McClure, Phys. Rev. 104, 666 (1956).

[15] E. Y. Andrei, G. H. Li, and X. Du, Rep. Prog. Phys. 75 (2012).

[16] M. S. Dresselhaus, G. Dresselhaus, and R. Saito, Carbon 33, 883 (1995).

[17] G. D. M.S. Dresselhaus, and Ph., and Avouris, Springer-Verlag, Berlin (2001).

[18] P. Avouris, MRS Bull. 29, 403 (2004).

[19] H. Kataura et al., Synth. Met. 103, 2555 (1999).

[20] D. Fathi, Journal of Nanotechnology (2011).

[21] L. Vanhove, Phys. Rev. 89, 1189 (1953).

[22] S. M. Bachilo et al., Science 298, 2361 (2002).

[23] M. J. O'Connell et al., Science 297, 593 (2002).

[24] Weisman, R. B. and S. Subramoney, The Electrochemical Society Interfac, 42 (2006).

[25] S. Iijima, and T. Ichihashi, Nature 363, 603 (1993).

[26] D. S. Bethune et al., Nature 363, 605 (1993).

[27] C. H. See, and A. T. Harris, Ind. Eng. Chem. Res. 46, 997 (2007).

[28] E. T. Thostenson, Z. F. Ren, and T. W. Chou, Compos. Sci. Technol. 61, 1899 (2001).

[29] M. Kumar, and Y. Ando, J. Nanosci. Nanotechnol. 10, 3739 (2010).

[30] D. N. Futaba et al., Nat. Mater. 5, 987 (2006).

[31] L. Ding et al., Nano Lett. 9, 800 (2009).

[32] L. X. Zheng et al., Nat. Mater. 3, 673 (2004).

[33] Y. Homma et al., Appl. Phys. Lett. 81, 2261 (2002).

[34] W. Choi et al., Crit. Rev. Solid State Mat. Sci. 35, 52 (2010).

[35] P. W. Sutter, J. I. Flege, and E. A. Sutter, Nat. Mater. 7, 406 (2008).

[36] C. Mattevi, H. Kim, and M. Chhowalla, J. Mater. Chem. 21, 3324 (2011).

[37] X. S. Li et al., Nano Lett. 9, 4268 (2009).

[38] X. S. Li et al., Science 324, 1312 (2009).

[39] S. Bae et al., Nat. Nanotechnol. 5, 574 (2010).

[40] Y. F. Zhang et al., ACS Nano 5, 4014 (2011).

[41] J. Martin et al., Nat. Phys. 4, 144 (2008).

[42] P. Y. Huang et al., Nature 469, 389 (2011).

[43] J. C. Meyer et al., Nano Lett. 8, 3582 (2008).

Chapter 2

Review of the photoexcited hot carrier photoresponse in graphene

2.1 Introduction

Electrons in band gap semiconductors can be excited into high energy states by absorbing photons. Directly converting these high energy hot carriers into electric energy with minimum loss is highly desirable for many highly efficient optoelectronic applications. However, in most conventional semiconductors, excited hot carriers rapidly relax to the band edge via electron-phonon scattering (~ ps). The energy absorbed by the phonons is then dissipated as heat, making it difficult for most devices to exploit the energy and thus significantly limiting the efficiency of current optoelectronics.

Taking photovoltaics as an example, the maximum theoretical efficiency of a single-junction device is only 31% (Shockley-Queisser limit) [1], and this low efficiency is primarily caused by phonon losses (Fig. 2.1a). To overcome this theoretical limit, ideas for utilizing hot carriers to enhance the power conversion efficiency have been proposed [2-3]. One of the ideas is to enhance the photovoltage of the device by directly capturing excited hot carriers before thermalization through energy-selective contacts (Fig. 2.1b). Because these hot carriers are

converted at their initial carrier temperature, the efficiency of the single junction device can be increased to 66%. An alternative approach is to enhance photocurrent generation by exploiting the carrier multiplication (CM) effect. This effect is a process whereby the absorption of a single photon results in multiple electron-hole pairs due to strong electron-electron coupling. Theoretically, a single junction with an ideal CM yield can lead to a power conversion efficiency of ~ 44%.

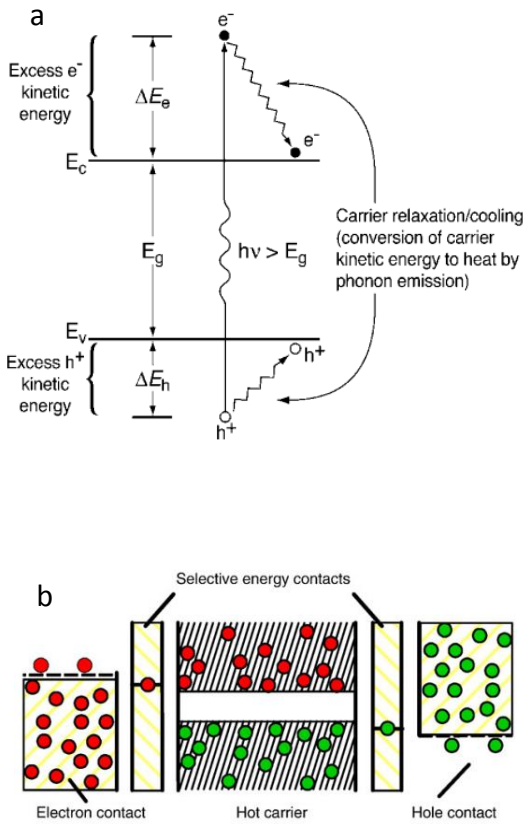

Figure 2.1 (a) Hot carriers rapidly relax to the band edge of semiconductors [4]. (b) Schematic drawing of the band diagram of a hot carrier photovoltaic [5-6].

At the heart of achieving hot carrier optoelectronics is to suppress the energy relaxation of the hot carriers. This suppression has been observed in several semiconductor nanocrystals and CNTs because the energy relaxation pathways of hot carriers can be greatly affected by

quantum confinement effects [7-10]. In contrast, graphene is a semi-metal nanomaterial, and it is expected that its unique massless dispersion band structure will lead to an unusual hot carrier photoresponse. In this chapter, we will present a brief review of the hot carrier photoresponse within semiconductors and graphene.

2.2 Suppression of hot carrier relaxation

2.2.1 Phonon bottleneck in nanocrystals

In bulk semiconductors, the photoexcitation of a semiconductor with photons above the semiconductor band gap will create hot electrons and holes out of equilibrium. To return to equilibrium, these hot carriers usually lose energy via multiple phonon emissions. Therefore, the hot carrier cooling rate is related to the electron-phonon scattering rate, and for each scattering process, the energy relaxation pathway is governed by momentum and energy conservation laws.

However, when reducing the dimensionality of semiconductors, the energy band structure will be quantized into discrete energy levels, which alter the energy relaxation pathways of hot carriers and potentially lead to more efficient optoelectronics. In fact, recent investigations of semiconductor nanocrystals have demonstrated novel relaxation pathways. As illustrated in Fig. 2.2, the conduction and valence energy bands become quantized due to the confinement of charge carriers into 0 dimensions. If the energy spacing between the quantized levels is larger than the highest optical phonon energy, the relaxation of excited hot carriers via optical phonon scattering will be impeded. Instead, hot carrier relaxation is only possible via slower multi-phonon emissions [11]. This phenomenon is typically called the phonon bottleneck effect. Importantly, because electron-optical phonon scattering is quenched, hot carriers can survive at the high energy states with a longer lifetime; this property is essential for developing hot carrier

optoelectronics.

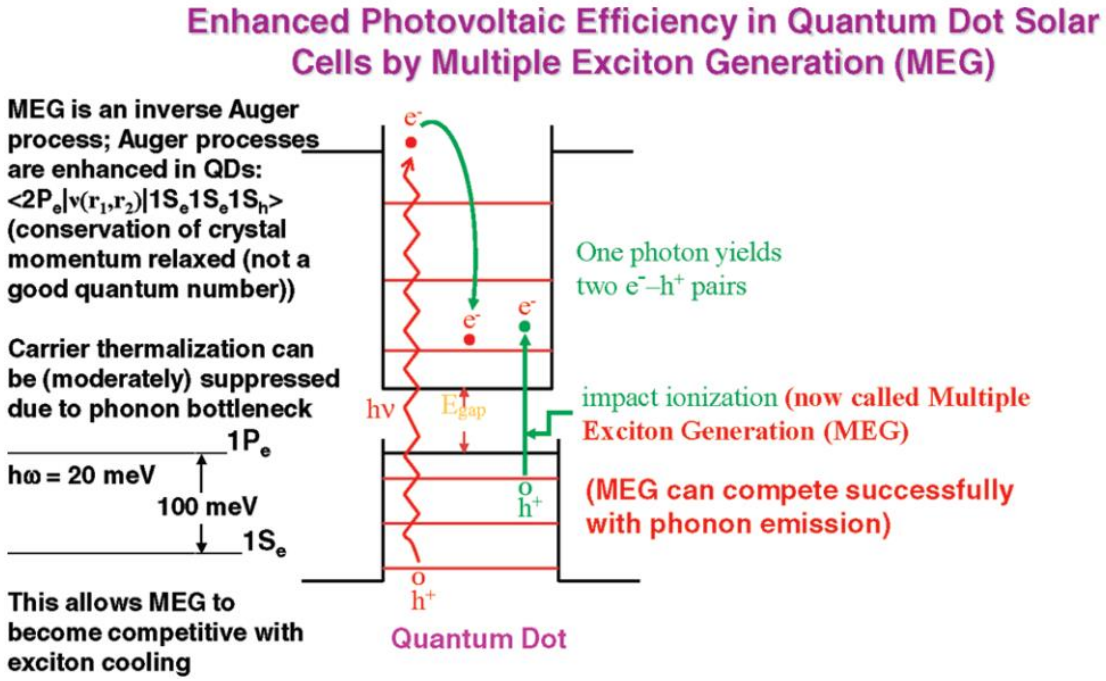

Figure 2.2 Phonon bottleneck in a semiconductor nanocrystal [11].

2.2.2 Phononic bandgap bottleneck

In semiconductors, excited hot carriers first scatter with high energy optical phonons close to the zone center, and these optical phonons then relax energy via the emission of acoustic phonons. Instead of restricting carrier-optical phonon interactions, the second approach to achieving the bottleneck effect involves constraining the scattering between optical and acoustic phonons. This inefficient optical-acoustic phonon interaction can build up the population of nonequilibrium optical phonons. Consequently, the optical phonons at elevated temperatures will slow the rate of hot carrier cooling.

This phenomenon has been generally observed in semiconductor binary compounds with

large differences between their anion and cation masses, such as BiN, InN and SnO [6, 12]. To understand how the bottleneck effect can occur in these materials, it is necessary to first examine their phonon dispersion relations. By treating these compounds as simple harmonic oscillators, the phonon energies can be derived using the equation

$$E_{acoustic} = \frac{h}{2}\sqrt{\frac{2T}{a}\frac{1}{M}}\ , (2.1)$$

which represents the maximum acoustic phonon energy at the Brillouin zone edge, and $E_{optical} = \frac{h}{2}\sqrt{\frac{2T}{a}\frac{1}{m}}$ (2.2) and $E_{optical} = \frac{h}{2}\sqrt{\frac{2T}{a}\left(\frac{1}{m}+\frac{1}{M}\right)}$ (2.3), which represent the minimum and maximum optical phonon energy respectively. Here, $\frac{T}{a}$ is a force constant, h is Planck's constant, and *M* and *m* are the atomic mass of the heavy and light atoms, respectively. Importantly, the above equations indicate that a wide phononic band gap (region of disallowed phonon energy) can be created if there is a large difference between *M* and *m*. The wide phononic gap suppresses optical phonon-acoustic phonon scattering because energy cannot be conserved, as demonstrated in Fig. 2.3. Thus, this inefficient scattering quenches the hot carrier cooling rate.

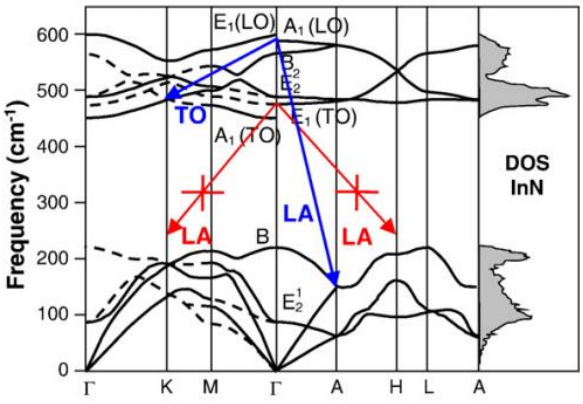

Figure 2.3 Phonon dispersion in InN demonstrating that the LO→2LA relaxation process is forbidden. The carrier must relax via the LO→TO+LA process, which results in a smaller loss of

energy [6].

2.2.3 Phonon bottleneck in graphene

Graphene does not have a quantized electronic band structure or a wide phononic band gap. Hence, the bottleneck effects occurring in nanocrystals and binary compounds cannot be applied to graphene. However, recent theoretical and experimental studies have demonstrated that hot electrons in graphene can be thermally decoupled from the lattice temperature even under weak illumination. The main reason lies in the very high optical phonon energy of graphene (~196 meV, near the zone center [13-15]) (Fig. 2.4), which can only relax high energy carriers rapidly. However, once the carriers cool below the optical phonon energy, they must scatter with multiple acoustic phonons to return to equilibrium. This acoustic phonon emission process is highly inefficient and creates a bottleneck for hot carrier cooling. Importantly, this unique property may lead to several unusual hot carrier photoresponses in graphene, which will be introduced in the following sections in this chapter.

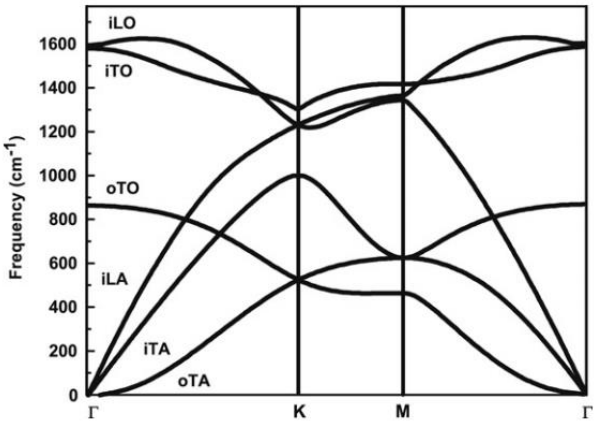

Figure 2.4 Phonon dispersion in graphene [13].

2.3 Dynamics of hot carrier cooling in graphene

2.3.1 Initial thermalization and cooling

Understanding the dynamics of hot carriers is not only of fundamental interest but is also important for developing novel optoelectronics. Among diverse measurement techniques, ultrafast pump-probe spectroscopy has been widely used to resolve carrier dynamics [16-18]. Initial optical pump-optical probe measurements have indicated that efficient carrier-carrier scattering in graphene results in the rapid thermalization of hot carriers immediately after optical excitation. These hot carriers are easily heated to a few thousand Kelvin due to the low electronic heat capacity of graphene. In the next few hundreds of femtoseconds, hot carriers lose energy to optical phonons and reach thermal equilibrium with the strongly coupled optical phonon temperature. Thus, the cooling rate of optical phonons becomes the main bottleneck to subsequent hot carrier cooling.

Fig. 2.5 presents the results of a typical pump-probe measurement [16]. The curve represents the transmission of the differential probe. By tuning the pump-probe time delay, we observe the decay of the curve because the transmission of the probe beam is sensitive to the hot carrier population induced by the pump beam. From the measurements, it is clear that each curve exhibits two distinct time scales. The initial fast decay within the first 70- to 120-fs range (τ_1) represents the rapid hot carrier thermalization process in graphene, and the slower relaxation time within the 1- to 2-ps range (τ_2) is determined by the optical phonon scattering rate.

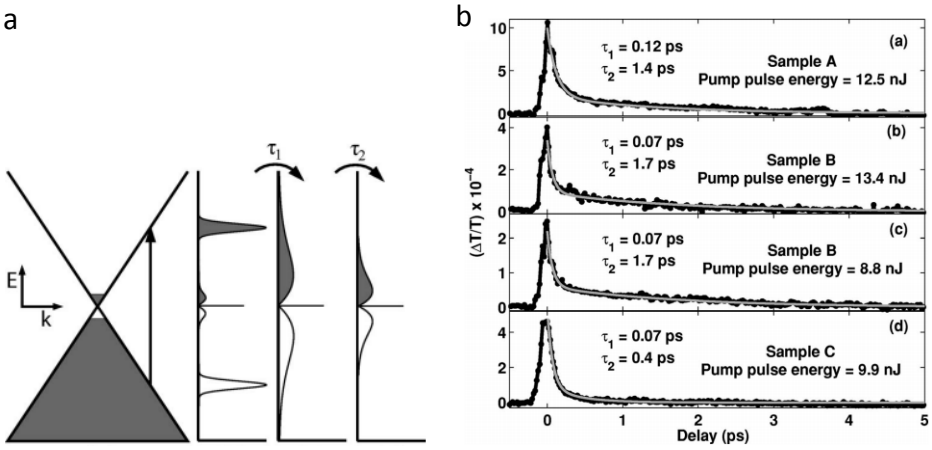

Figure 2.5 Dynamics of hot carrier cooling in graphene. (a) Photoexcited hot carriers thermalize within the timescale τ_1, and the subsequent cooling via optical phonon emissions occurs on a timescale τ_2. (b) Experimental results of the pump-probe measurements. The curves provide information about the thermalization timescale (τ_1) and relaxation timescale (τ_2) [16].

2.3.2 Cooling below the optical phonon energy

As described in section 2.2.3, when the hot carrier energy is below the optical phonon energy, carrier cooling will be dominated by acoustic phonon emission. However, the small Fermi surface and momentum conservation severely constrain the pathway of carrier relaxation as illustrated in Fig. 2.6a, rendering the carrier cooling inefficient. However, this slow relaxation process is difficult to observe using typical optical pump-optical probe spectroscopy, because this technique can only measure the relaxation of high energy hot carriers. Therefore, an optical pump-terahertz probe technique was employed to study hot carrier cooling as demonstrated in Figs. 2.6b and 2.6c [19]. Interestingly, the measured curve shows much slower decay. This provides direct evidence of inefficient cooling by acoustic phonons.

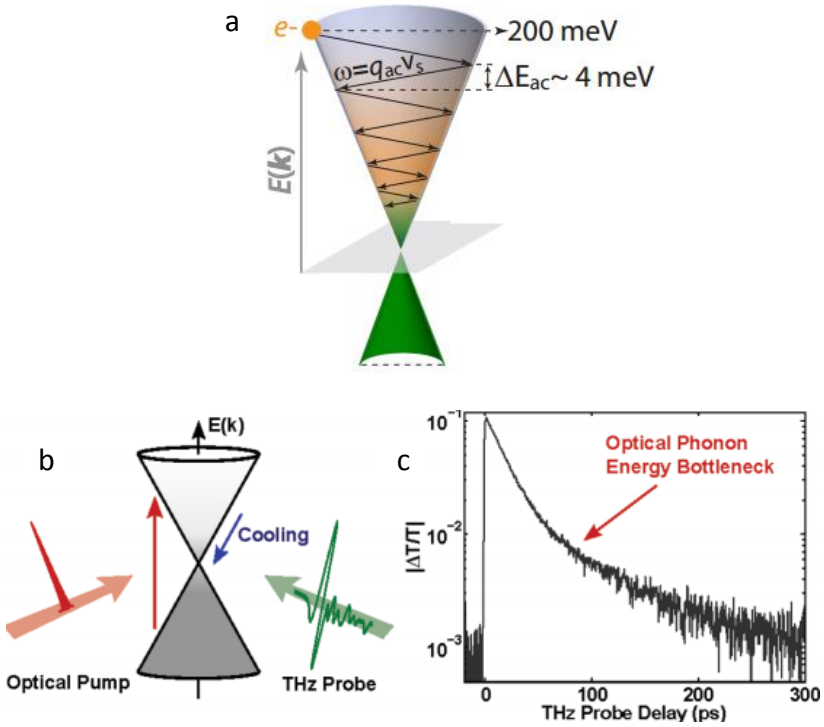

Figure 2.6 Slow hot carrier cooling by acoustic phonons. (a) Hot carrier relaxation in pristine graphene. Each relaxation step is restricted by momentum and energy conservation [20]. (b) Schematic drawing of optical pump-terahertz probe measurements on graphene. (c) Experimental results of pump-probe measurements. The faster decay is related to the hot phonon bottleneck while the slower decay (>60 ps) is due to the optical phonon energy bottleneck [19].

2.3.3 Supercollision (Disorder-assisted) cooling

Despite this promising progress, the resolved hot carrier relaxation time in the optical pump-terahertz probe measurement remains 1-2 orders of magnitude faster than the theoretical predictions (~ns) [21], which suggests that other mechanisms in addition to acoustic phonon emissions may also play an important role in assisting carrier cooling. To clarify this issue, the concept of disorder-assisted scattering (also called supercollision cooling) was recently proposed and experimentally confirmed by photocurrent and Johnson noise thermometry measurements

[20, 22-23]. The basic idea behind this supercollision model is that the impurities could provide alternative pathways for hot carrier cooling as shown in Fig. 2.7. Therefore, scattering via these impurities will not be constrained by the small Fermi surface in graphene. Moreover, because the impurities can provide large momentum space and energy for scattering, faster energy relaxation would be observed in disordered graphene than in disorder-free graphene.

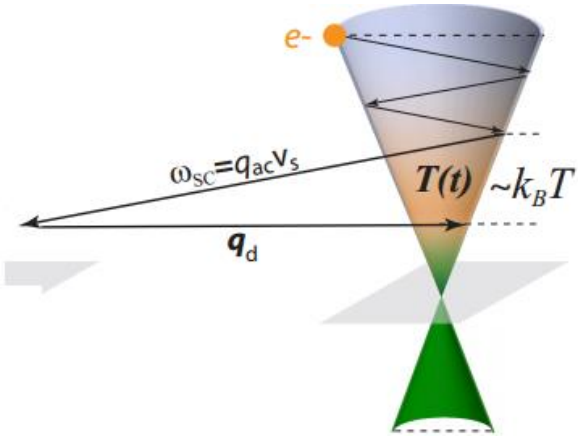

Figure 2.7 Hot carrier relaxation in disorder-graphene. The disorder relaxes momentum conservation, leading to faster cooling [20].

2.4 Hot carrier photoresponse in graphene

2.4.1 Nonlinear photoluminescence

The radiative recombination of an electron-hole pair results in light emission (photoluminescence). Its spectral emission is generally below the excitation photon energy, with the highest intensity near the semiconductor band gap energy. The blueshift of photoluminescence can also be observed in a few bulk semiconductors, demonstrating efficient intraband carrier-carrier scattering (Fig. 2.8a). However, their parabolic band structures limit the momentum exchange. Thus, the range of blueshifted photoluminescence usually appears in a

very narrow frequency range.

In contrast, graphene provides a unique electronic system that exhibits a linear dispersion band structure and strong carrier-carrier scattering. Therefore, under femtosecond pulse illumination, excited hot carriers can efficiently exchange momentum and energy, which boosts hot carriers to the higher energy level, as illustrated in Fig. 2.8b. This physical concept has also been experimentally confirmed in recent years. By exciting graphene with the 1.5 eV pulse laser, a very broadband photoluminescence (as high as 3.1 eV) from the graphene can be measured (Fig. 2.8c). These results agree with Planck's law, indicating that hot carriers in graphene would rapidly thermalize after excitation [24-25].

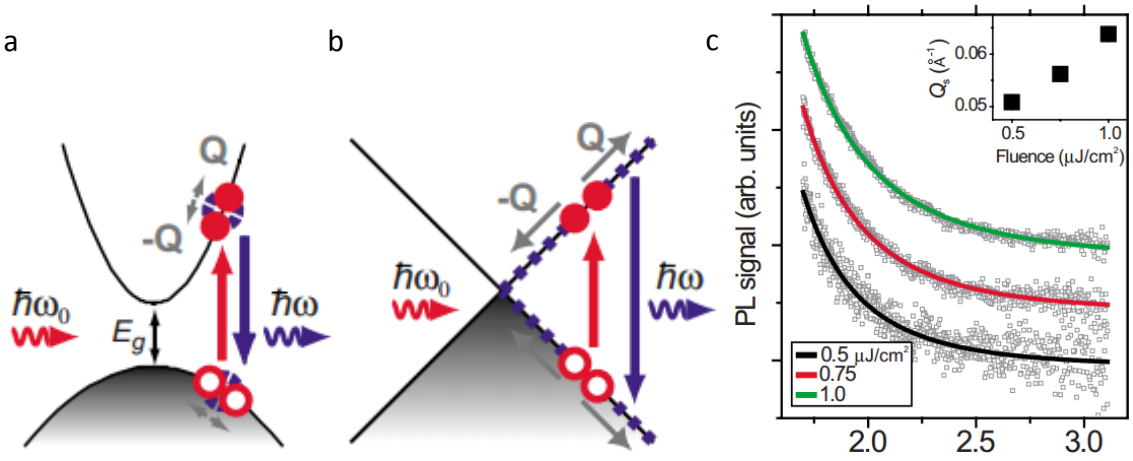

Figure 2.8 Nonlinear photoluminescence in graphene. (a) Inefficient carrier-carrier scattering in the parabolic band. (b) Efficient carrier-carrier scattering in the linear band. (c) The photoluminescence measured from graphene under 1.5 eV pulse excitation [24-25].

2.4.2 Carrier multiplication

When carriers are excited to a high energy level, they can relax their energy via two competing pathways: electron-electron and electron-phonon scattering. Recent studies have exploited optical pump-terahertz probe techniques and have further clarified that electron-electron scattering would be very efficient in highly doped graphene during the initial stage of hot carrier cooling. Therefore, carrier multiplication can be observed in doped graphene after pulse laser excitation [26]. As shown in Fig. 2.9, a photoexcited hot carrier triggers a cascade of intraband electron-electron scattering processes, where energy and momentum are transferred to electrons in the Fermi sea, producing multiple secondary hot carriers in the conduction band. The efficiency of carrier multiplication depends not only on the graphene doping level but also on the excitation photon energy. These observations suggest that graphene could be a promising photoactive material.

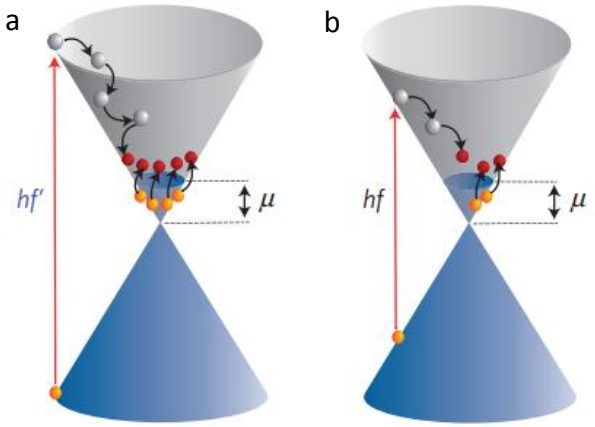

Figure 2.9 The hot carrier created by absorbing (a) a high energy photon and (b) a low energy photon will relax its energy to the electrons in the Fermi sea, which creates multiple hot electrons in the conduction band [26].

2.4.3 Hot carrier diffusion

Hot carrier diffusion in graphene has also been recently investigated. When graphene is excited by a tightly focused laser pulse, initially hot carriers with a point-like spatial profile are created. After a few picoseconds, these carriers will diffuse away from the excitation spot due to the density gradient (Fig. 2.10a-b). This spatio-temporal dynamics of hot carriers could be monitored using the high resolution ultrafast pump-probe technique (Fig. 2.10) and the measured results provide information about the carrier diffusion coefficient $D{\sim}12000\ cm^2s^{-1}$ in graphene [27].

This high diffusion coefficient within graphene arises from its high mobility (μ) and high carrier temperature (T_e) after excitation, which can be understood via the Einstein relation:

$$D = \frac{\mu K_B T_e}{2e} \quad (2.5)$$

where e is the electron charge and K_B is Boltzmann's constant.

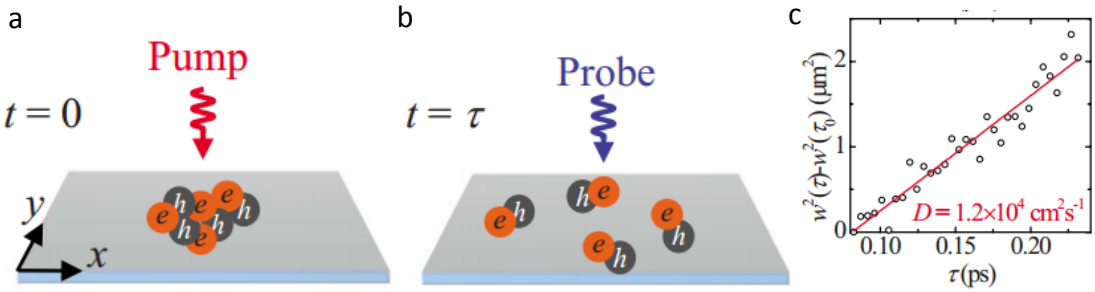

Figure 2.10 Hot carrier diffusion in graphene. (a) Hot carriers initially created by the femtosecond pump pulse. (b) The second probe pulse detects the hot carrier distribution after a delay time. (c) The carrier diffusion coefficient can be extracted by measuring the carrier distribution over time [27].

2.5 Converting photoexcited hot carriers into an electrical signal

The conversion of excited carriers into an electrical current is key in developing optoelectronics, such as photovoltaics and photodetectors. Thus, understanding the mechanisms

of photocurrent generation from graphene has recently been the subject of intensive research. Thus far, it has been demonstrated that photocurrent can be generated from graphene p-n and graphene-metal Schottky junctions, and the mechanisms of photocurrent generation are generally attributed to the photovoltaic effect or photo-thermoelectric effect, which will be discussed in this section.

2.5.1 Photovoltaic effect

Photocurrent generation from graphene was first observed from graphene-metal junctions [28-31]. When metal is deposited on top of graphene, the Fermi level of graphene will be pinned by the metal. As a result, the asymmetric chemical potential between the metal-controlled area and the gate-controlled graphene channel will lead to band bending near the edge of the contacts, as illustrated in Fig. 2.11. This band bending creates the built-in electric field, which can dissociate the electron-hole pair and induce photocurrent generation. Importantly, the polarity of the photocurrent is determined by the direction of the electric field and can be flipped by modulating the doping level of the graphene channel by applying gate voltages.

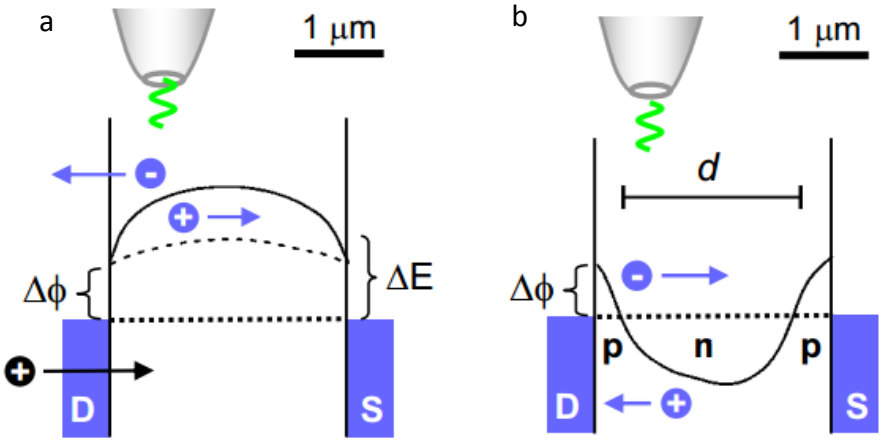

Figure 2.11 Photocurrent generation induced by the photovoltaic effect. The two figures demonstrate that the polarity of the photocurrent can be reversed by tuning the band bending [31].

2.5.2 Photo-thermoelectric Seebeck effect

Photocurrent generation from graphene induced by the thermoelectric effect was first identified in graphene single-bilayer junctions as well as p-n junctions [32-34]. When the junctions are heated with light, the local electron temperature will be thermally decoupled from the lattice temperature. The electronic temperature gradient produces a thermoelectric field (E_{T}) due to the Seebeck effect and thereby drives the photocurrent flow:

$E_{\mathrm{T}} = S\Delta T$ (2.6)

where S is the Seebeck coefficient (also called the thermoelectric power) and ΔT is the difference in electron temperature between the excitation area and its surroundings. However, if the laser spot is focused onto homogeneous graphene (an area with a homogeneous S), an isotropic photocurrent flowing away from the excitation spot will yield no net photocurrent (Fig. 2.12a) [35]. In contrast, when illuminating a junction with light, a photocurrent can be generated because the symmetry of the Seebeck coefficient across the junction is broken (Fig. 2.12b). In this situation, the photovoltage (V_{T}) across the junction can be built-up and written as [35]

$V_{\mathrm{T}} = (S_2 - S_1)\Delta T,$ (2.7)

where S_2 and S_1 represent the Seebeck coefficients at the two ends of the junction, and these coefficients could be derived by measuring the electrical gate response of graphene and using Mott's formula [36-37]:

$\mathrm{S} = \frac{\pi^2 k_B^2 T}{3e} \frac{1}{\mathrm{G}} \frac{\mathrm{d}G}{\mathrm{d}V_g} \frac{\mathrm{d}V_g}{\mathrm{d}E}\Big|_{\mathrm{E}=\mathrm{E}_f},$ (2.8)

where k_B is Boltzmann constant, e is the electron charge, G is the conductance and E_f is the Fermi energy. From the above equations, we can see that the amplitude of photocurrent is proportional to the difference in temperature (ΔT) as well as the Seebeck coefficients ($S_2 - S_1$).

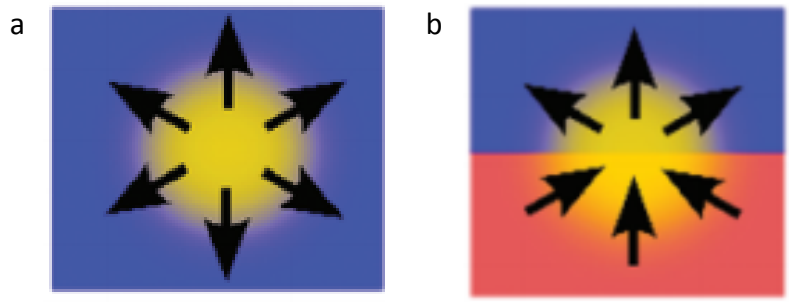

Figure 2.12 The direction of thermoelectric current flow when heating (a) homogeneous graphene and (b) inhomogeneous graphene junctions [35].

2.5.3 Photoconductivity of graphene

When materials absorb light with sufficient energy, the increase of excited electrons and holes will increase the electrical conductivity of the materials. This phenomenon is called photoconductivity and has been widely observed in semiconductors and a few insulators. The relation between the change of photoconductivity ($\Delta\sigma$) and excited carriers can be expressed via the following equation [38]:

$$\Delta\sigma = e\left(\mu_n \Delta n + \mu_p \Delta p\right) \quad (2.9)$$

where Δn and Δp are the excess electron and hole concentrations, respectively, and μ_n and μ_p are the electron and hole mobilities, respectively. When reaching the steady state, the recombination and generation rate of carriers (G_{opt}) will be equal and the equation can be written as

$$\Delta\sigma = e \cdot G_{opt} \cdot \tau\left(\mu_n + \mu_p\right) \quad (2.10)$$

The photoconductivity in graphene can be quite different. When illuminating doped graphene with light, a decrease in conductivity was observed [39]. This peculiar photoresponse results from the bolometric effect, in which the light absorption in graphene increases its electron

temperature and thereby increases the resistance of the device. This observation of the bolometric effect in graphene not only furthers our fundamental understanding but also provides a basis for developing graphene-based bolometers.

2.6 Hot carrier optoelectronics based on graphene

2.6.1 Graphene photodetectors

Graphene photodetectors have been the subject of extensive research since the discovery of photocurrent generation from graphene. The first graphene photodetector was created using interdigitated metal (Au)-graphene-metal (Ti) structures as illustrated in Fig. 2.13 [40-41]. The asymmetric metallization scheme causes asymmetric band bending. Thus, when the entire device is illuminated, the photocurrent can be detected. The advantages of this graphene photodetector include its high speed (~16 GHz) and broad spectral detection. However, the photoresponsivity is limited to 6.1 mA/W because graphene has a low absorption coefficient (2.3%), and the photoactive areas are limited to the vicinity of metal contacts [42-43].

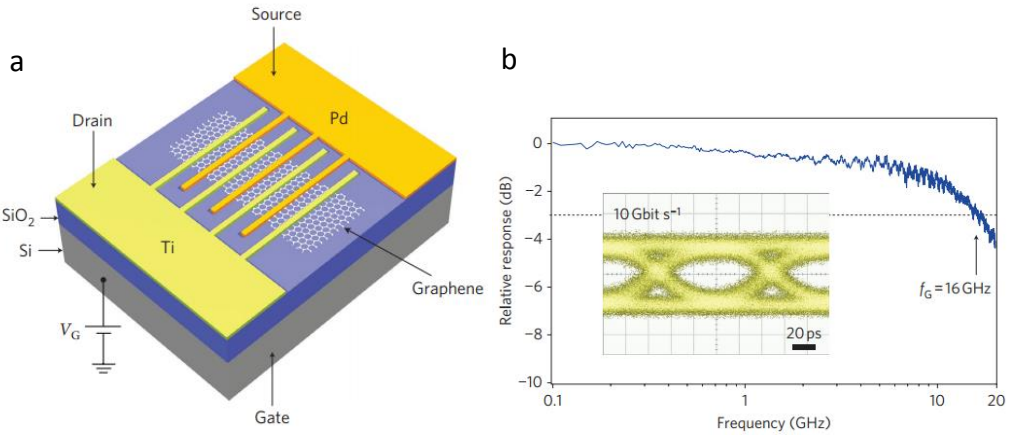

Figure 2.13 A graphene based photodetector. (a) Schematic drawing of the device architecture. (b) The measurement demonstrates that this device can be operated at very high speed [41].

2.6.2 Graphene hot electron bolometers

The working principle of a hot electron bolometer is based on converting photon energy into hot carriers, which are at thermal nonequilibrium with the surrounding phonons. These thermally decoupled hot carriers thereby affect the resistance of materials due to the bolometric effect, yielding a detectable signal. To achieve this effect, conventional hot electron bolometers have to be operated at cryogenic temperature, because the electron gas can easily be decoupled from the phonon vibrations at low temperature.

In contrast, hot carriers under thermal nonequilibrium can easily be achieved in graphene even at room temperature due to the optical phonon bottleneck effect. This effect, combined with its broadband light absorption property, makes graphene an extremely attractive candidate for broad spectral bolometer applications. An initial measurement utilized a graphene bolometer to detect infrared light [44]. The reported voltage responsivity was $\sim 2 \times 10^5\, VW^{-1}$, which is comparable to commercial silicon bolometers. A more recent study exploited an impedance-matching scheme and noise thermometry to further push the photodetection of graphene bolometers to the microwave regime at a high speed of 1.2 GHz [45].

2.7 Conclusions

In this chapter, we presented a brief review of the hot carrier photoresponse in graphene. We began with a discussion of the energy relaxation pathways of hot carriers and their dynamical timescales. Within these relaxation processes, we further described various phenomena induced by hot carriers in graphene, including photoluminescence, carrier multiplication and efficient diffusion. These unusual responses are directly related to the unique electronic properties of graphene. For optoelectronic applications, we also described recent fundamental studies that utilized graphene p-n or graphene/metal junctions to convert excited carriers into an electric current. Based on these fundamental investigations, we also see that diverse graphene-based hot carrier devices, such as bolometers or ultrafast photodetectors, have been further developed recently. We described these devices at the end of this chapter. These promising observations and developments motivated us to perform further explorations. In chapter 5, we will further examine the hot carrier photoresponse in graphene devices and provide different perspectives. In chapter 6, we will elaborate on how hot carriers can be employed to create ultra-broadband and high responsivity graphene photodetectors.

References:

[1] W. Shockley, and H. J. Queisser, J. Appl. Phys. 32, 510 (1961).

[2] M. A. Green, Springer (2006).

[3] M. A. Green, Prog. Photovoltaics 9, 123 (2001).

[4] A. J. Nozik, Annu. Rev. Phys. Chem. 52, 193 (2001).

[5] G. J. Conibeer et al., Thin Solid Films 516, 6968 (2008).

[6] G. J. Conibeer et al., Thin Solid Films 516, 6948 (2008).

[7] N. M. Gabor et al., Science 325, 1367 (2009).

[8] W. A. Tisdale et al., Science 328, 1543 (2010).

[9] J. B. Sambur, T. Novet, and B. A. Parkinson, Science 330, 63 (2010).

[10] R. D. Schaller, and V. I. Klimov, Phys. Rev. Lett. 92 (2004).

[11] A. J. Nozik, Nano Lett. 10, 2735 (2010).

[12] G. Conibeer et al., Sol. Energy Mater. Sol. Cells 93, 713 (2009).

[13] L. M. Malard et al., Phys. Rep.-Rev. Sec. Phys. Lett. 473, 51 (2009).

[14] M. Lazzeri et al., Phys. Rev. B 78, 081406 (2008).

[15] J. Maultzsch et al., Phys. Rev. Lett. 92, 075501 (2004).

[16] J. M. Dawlaty et al., Appl. Phys. Lett. 92, 042116 (2008).

[17] H. N. Wang et al., Appl. Phys. Lett. 96, 081917 (2010).

[18] M. Breusing, C. Ropers, and T. Elsaesser, Phys. Rev. Lett. 102, 086809 (2009).

[19] J. H. Strait et al., Nano Lett. 11, 4902 (2011).

[20] M. W. Graham et al., Nat. Phys. 9, 103 (2013).

[21] R. Bistritzer, and A. H. MacDonald, Phys. Rev. Lett. 102, 206410 (2009).

[22] J. C. W. Song, M. Y. Reizer, and L. S. Levitov, Phys. Rev. Lett. 109, 106602 (2012).

[23] A. C. Betz et al., Nat. Phys. 9, 109 (2013).

[24] W. T. Liu et al., Phys. Rev. B 82, 081408 (2010).

[25] C. H. Lui et al., Phys. Rev. Lett. 105, 127404 (2010).

[26] K. J. Tielrooij et al., Nat. Phys. 9, 248 (2013).

[27] B. A. Ruzicka et al., Phys. Rev. B 82, 195414 (2010).

[28] E. J. H. Lee et al., Nat. Nanotechnol. 3, 486 (2008).

[29] J. Park, Y. H. Ahn, and C. Ruiz-Vargas, Nano Lett. 9, 1742 (2009).

[30] F. N. Xia et al., Nano Lett. 9, 1039 (2009).

[31] T. Mueller et al., Phys. Rev. B 79, 245430 (2009).

[32] X. D. Xu et al., Nano Lett. 10, 562 (2010).

[33] N. M. Gabor et al., Science 334, 648 (2011).

[34] M. C. Lemme et al., Nano Lett. 11, 4134 (2011).

[35] J. C. W. Song et al., Nano Lett. 11, 4688 (2011).

[36] M. Cutler, and N. F. Mott, Phys. Rev. 181, 1336 (1969).

[37] P. Wei et al., Phys. Rev. Lett. 102, 166808 (2009).

[38] A. Rose, Robert E. Krieger Publishing (1978).

[39] M. Freitag et al., Nat. Photonics 7, 53 (2013).

[40] F. N. Xia et al., Nat. Nanotechnol. 4, 839 (2009).

[41] T. Mueller, F. N. A. Xia, and P. Avouris, Nat. Photonics 4, 297 (2010).

[42] R. R. Nair et al., Science 320, 1308 (2008).

[43] K. F. Mak et al., Phys. Rev. Lett. 101, 196405 (2008).

[44] J. Yan et al., Nat. Nanotechnol. 7, 472 (2012).

[45] K. C. Fong, and K. C. Schwab, Phys. Rev. X 2, 031006 (2012).

Chapter 3

Instrumentation

3.1 Introduction

The successful development of optoelectronics requires a comprehensive characterization of their optical-to-electrical responses. This chapter will introduce the experimental infrastructures, used to investigate the nanoscale junctions in this thesis. In section 3.2, we will describe our method of electrical measurements, and in section 3.3, we will introduce the light sources used for our optical measurements. Additionally, the calibration of optical power within different spectrum regimes will be addressed. We also used the scanning photocurrent spectroscopy and ultrafast pump-probe spectroscopy. These two measurement techniques incorporate various electronics and optics and could provide a powerful method for characterizing the spatio-temporal properties of devices. We will describe these two setups in detail in sections 3.4 and 3.5.

3.2 Electrical instruments

For purely electrical characterizations, devices can be examined using either a room temperature probe station or a low temperature probe station. As shown in Fig. 3.1a, our probe station includes four passive probes (tungsten needle). Each probe can be independently moved by its manipulator to contact the surface of devices. These probes can either provide or receive

electrical signals, such as voltage or current. Based on this setup, the electrical properties of various devices can be rapidly tested without requiring any wire-bonding process.

To measure the electrical response of the devices under light illumination, the devices were glued and wire-bound to an Oxford optical cryostat (Fig. 3.1b). The light was coupled into the cryostat from the top window, which is transparent from ultraviolet to mid-infrared light. The devices in the cryostat chamber could be maintained under low vacuum using a turbo pump and under low temperature by injecting liquid helium or nitrogen. Electronic feed-throughs allow for electrical access to the device. Thus, the optoelectronic properties of devices can be characterized.

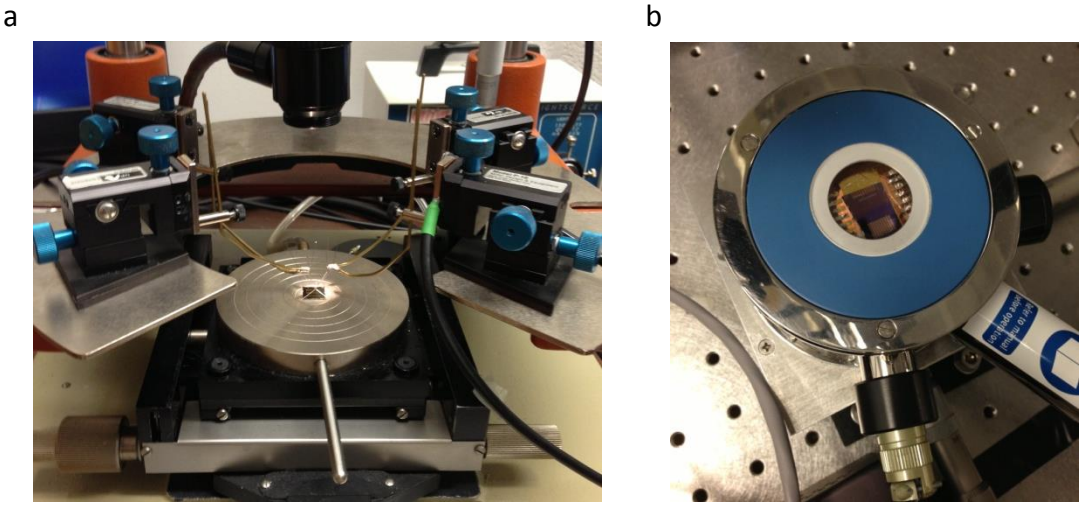

Figure 3.1 Instruments for characterizing the electrical properties of devices. (a) Room temperature probe station. (b) A sample mounted in an Oxford optical cryostat.

3.3 Light sources and power calibration

Continuous wave light sources

In our experiments, we can couple various wavelengths (532 nm, 800 nm, 900 nm, 1550 nm) of continuous wave (CW) light into our measurement setup. These light sources are provided by different semiconductor laser diodes. Each laser diode emits only single wavelength, and the output power is controlled by the current controller. The laser power in the visible region

is calibrated using a Si photodiode (Newport 918D-SL-OD3R), while in the near-infrared region, the power is calibrated using an InGaAs photodiode (Newport 918D-IR-OD3).

Near-infrared femtosecond light pulse

To generate near-infrared light pulses, we use a Coherent Ti:sapphire oscillator that is optically pumped by a Verdi 10 Watt green laser. The duration of each pulse is ~150 fs, and the pulse repetition frequency is 76 MHz. The central wavelength of the light pulses can be tuned continuously from 700 nm to 1000 nm, with the most efficient output at 800 nm. In our measurements, we calibrate the output power using the Si photodetector.

Near to mid-infrared femtosecond light pulse

For the longer wavelength regime, the light source is provided by optical parametric amplification (OPA) and difference frequency generation (DFG). OPA is pumped by a 250 kHz amplified Ti:sapphire laser (Coherent, RagA 9000), generating a signal and idler waves at wavelengths of 1.3 μm and 2.1 μm, respectively. Both waves are sent to DFG to produce light with a wavelength of 3.2 μm. A zinc selenide aspherical lens is used to focus the infrared light to the device. The power is measured by an InGaAs detector (Thorlabs DET10D) at 1.3 μm and 2.1 μm, and by an InSb detector (Infrared Associates, IS-2.0) at 3.2 μm. Both detectors are calibrated using a thermopile broadband power meter (Melles Griot, 13PEM001).

3.4 Scanning photocurrent spectroscopy

Scanning photocurrent spectroscopy is a powerful technique that can spatially resolve the electronic band profile of semiconductors. In this section, we will introduce this technique in detail.

Fig. 3.2 presents a schematic of the scanning photocurrent experimental setup. To scan the laser spot, high speed scanning galvo mirror systems are implemented before the objective

lens. This galvo system consists of two mirrors, and the angular orientation of each mirror can be precisely controlled using its servo controller. Rotating these two mirrors on a dual axis changes the incident angle of the laser beam relative to the objective. Thus, the focused laser spot can be spatially scanned at the surface of devices in two dimensions. By placing the device underneath the objective, we can probe its spatial photoresponse.

For typical aspherical lenses, however, if the collimated light is not at normal incidence, the focused laser spot will be significantly distorted due to optical aberrations. Thus, we incorporate a near-infrared Mitutoyo objective (50x) to focus the light. This objective includes multiple lens sets to minimize aberrations and distortions. Additionally, this objective has a long working distance (13.8 mm) while maintaining a high numerical aperture (N.A. = 0.5).

To image the measured sample, two beam splitters (BS, 98% transmission, 2% reflection) are incorporated into the setup. One of the beam splitters couples the reflected light from the devices into the CCD camera, while the other couples the reflected light into the photodiode. The image captured by the CCD camera (Fig. 3.3a) and the scanning image measured by the photodiode (Fig. 3.3b) could provide information about the position of the laser spot.

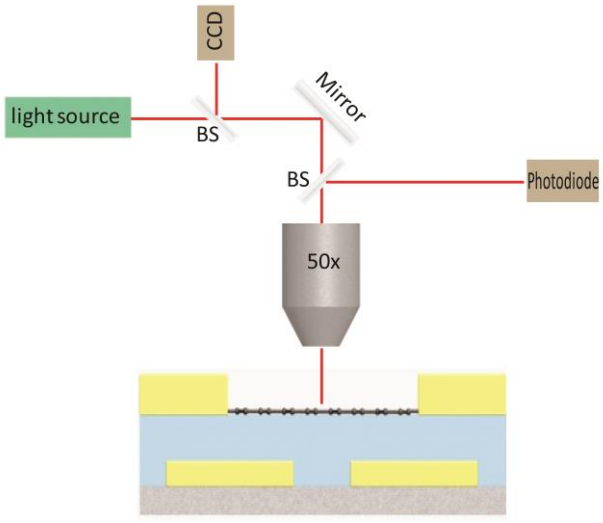

Figure 3.2 Schematic drawing of the scanning photocurrent spectroscopy setup.

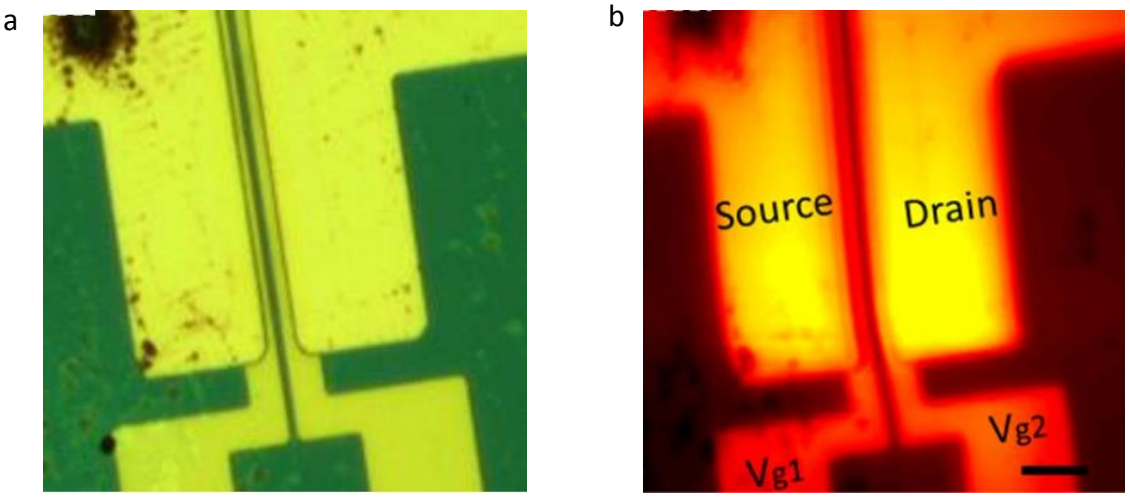

Figure 3.3 (a) The image captured by the CCD camera. (b) The scanning image resolved by the photodiode.

3.5 Ultrafast pump-probe spectroscopy

As discussed in chapter 2, the ultrafast pump-probe technique has been frequently used to investigate the dynamics of photocarriers. The underlying principle of this technique is based on repeatedly illuminating the sample with two pulses separated by an adjustable time delay. The first pulse used to excite the sample is called the pump pulse, while the second pulse is called the probe pulse. If these two pulses are sufficiently temporally separated, the two pulses will not affect each other because the system has completely relaxed before the arrival of the probe pulse. In contrast, if the two pulses are close enough that the electrons excited by the pump pulse have not completely decayed, the signal induced by the probe pulse would be correlated to the pump pulse. Therefore, by monitoring the signal as a function of the time delay, the temporal dynamics of hot carriers initiated by the pump pulse can be obtained. This section will introduce our pump-probe measurement setup.

Fig. 3.4 presents a schematic diagram of our ultrafast pump-probe setup. Laser pulses are

generated from a Ti-sapphire laser with a repetition rate of 76 MHz, and the central wavelength is 800 nm. The duration of each pulse is 150 fs, which is also the limit of the temporal resolution. The generated femtosecond pulse train is then split into the probe and pump beam by a beam splitter (BS, 50% transmission, 50% reflection). The pump beam is reflected by a fixed mirror (M1), while the probe beam is reflected by another mirror (M2), which is mounted on a linear motorized stage. Moving this stage varies the optical path length of the probe beam and thereby changes the delay time between the pump and probe pulses when hitting the sample. Both reflected beams are collinearly combined and focused on the samples in a cryostat. Thus, we can detect the electrical signal from the devices as a function of the time delay between the two pulses.

Notably, in this optical setup, only 50% of the light is sent to the measured sample, while the other 50% is reflected back to the Ti-sapphire cavity. This reflected beam would significantly disturb the mode-locked pulses. Therefore, a Faraday isolator must be placed at the exit of the cavity to block the reflected beam. In addition, a quarter waveplate is placed in this setup to rotate the polarization of the pump beam by 90 degrees with respect to the probe beam to suppress the effect of laser interference on the measured signal.

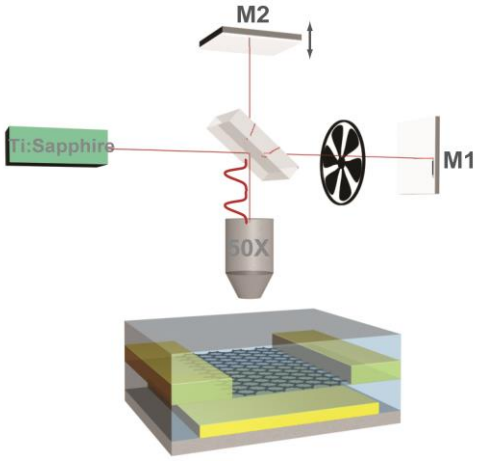

Figure 3.4 Schematic drawing of the ultrafast pump-probe spectroscopy setup.

3.6 Conclusions

In this chapter, we described our experimental instruments, setups and measurement techniques. We will see in the remaining chapters that the scanning photocurrent technique can be a powerful tool for acquiring spatially resolved photoresponse measurements. Meanwhile, the ultrafast pump-probe technique provides a route for measuring carrier dynamics with femtosecond-scale temporal resolution. By combing the spatial and temporal information, we are able to examine our device properties in-depth.

Chapter 4

A Fully Tunable Single-Walled Carbon Nanotube Diode

4.1 Introduction

Integrated electronics and optoelectronics of the coming generation can benefit from actively tunable device components, where a single device can be programmed to embody different device concepts to achieve high packing density, diverse functionalities, and low power consumption [1]. However, for conventional bulk devices, their electronics performances are predetermined by material properties such as band gap energy, doping level and metal-semiconductor interfaces. As a result, active tuning of individual device becomes extremely challenging. In contrast, a device integrated with nanomaterials might potentially exhibit diverse functionalities, since electronic density of states as well as Femi energy of nanomaterials are highly tailorable.

Among diverse nanomaterials, a single-walled carbon nanotube (SWNT) emerges as a powerful class of material due to its extraordinary electrical and optical properties [2-4]. Thus far, a wide variety of device concepts have been realized by using SWNTs. For example, ideal diode behavior has been demonstrated on suspended SWNTs with electrostatic p-n doping [5-7], and

efficient light emission and photocurrent generation have also been shown in SWNT diodes [8-10]. In addition, strong band-to-band tunneling across a nanotube Schottky junction or p-n junction [11-13] has led to SWNT tunneling diodes exhibiting negative differential resistance with high peak to valley ratio [14]. However, all previous nanotube device designs can only exhibit one specific device concept [15].

In this chapter, we will present a tunable SWNT diode. Specifically, the diode's turn-on voltage under forward bias can be continuously tuned up to 4.3 V by simply controlling dual-gate voltages. Furthermore, the same device design can be configured into a backward diode by tuning the band-to-band tunneling current with gate voltages. A nanotube backward diode is demonstrated for the first time with nonlinearity exceeding the ideal diode. Our model suggests this unique backward diode property is related to the 1D density of state of SWNT.

4.2 Device fabrication and electrical characterization

4.2.1 Device fabrication

To fabricate a pristine device is central for achieving high performance electronics. In this regard, we adopted a novel one step transfer technique [7] to fabricate ultraclean and fully suspended SWNT devices. The advantages of adopting this technique include: (1) The grown SWNTS are not contaminated by any physical or chemical fabrication process. (2) The grown SWNTS can be precisely transfer to the selected locations. (3) The transfer technique is conducted under room temperature. Therefore, device architectures and materials are not limited by high growth temperature.

The fabrication processes can be divided into three steps. The first step is to prepare the underlying split-gate structure. As shown schematically in Fig. 4.1., SiO_2/Si_3N_4 = 750 nm/750 nm were deposited on the Si wafer using plasma enhanced chemical vapor deposition (PECVD).

Following photolithography processes defined the cathode and anode electrodes. To achieve a suspended structure, two electrode areas were dry etched to form pillars and then followed by BHF wet etching to create the undercuts. So, when depositing Cr/Au metals onto this substrate, the top electrode metals do not short with the bottom metal. Finally, another photolithography and metal wet etching processes were adopted to define the bottom split gate electrodes.

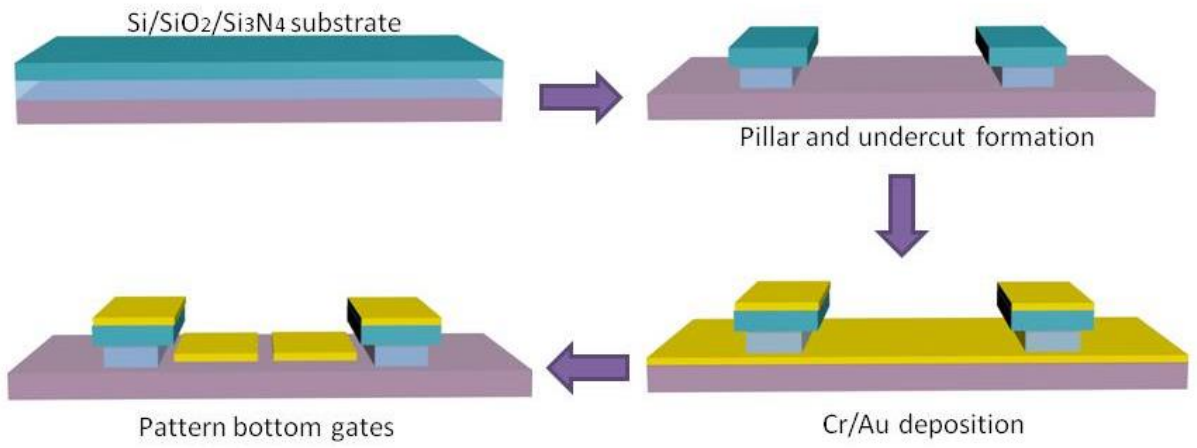

Figure 4.1 Fabrication procedure of the pre-patterned substrate.

The second step is to grow SWNTs on the other double side polished quartz substrate. As shown in Fig.4.2, we first created a pair of pillars on the quartz substrate using the dry etching and then deposited 3 Å Fe on this substrate as catalysts. For nanotube growth, the flying catalyst CVD recipe was used so that the grown SWNTs can suspend between two pillars.

After preparing the above two substrates, the last step is to directly transfer SWNTs from the growth substrate to the device substrate with pre-patterned cathode, anode, and gate electrodes. This transfer process is shown in Fig. 4.3a. By aligning these two substrates and bringing them into contact, SWNTs could be transferred and span across the metal electrodes. As a result, a fully suspended nanotube device is formed as shown in the SEM image (Fig. 4.3b).

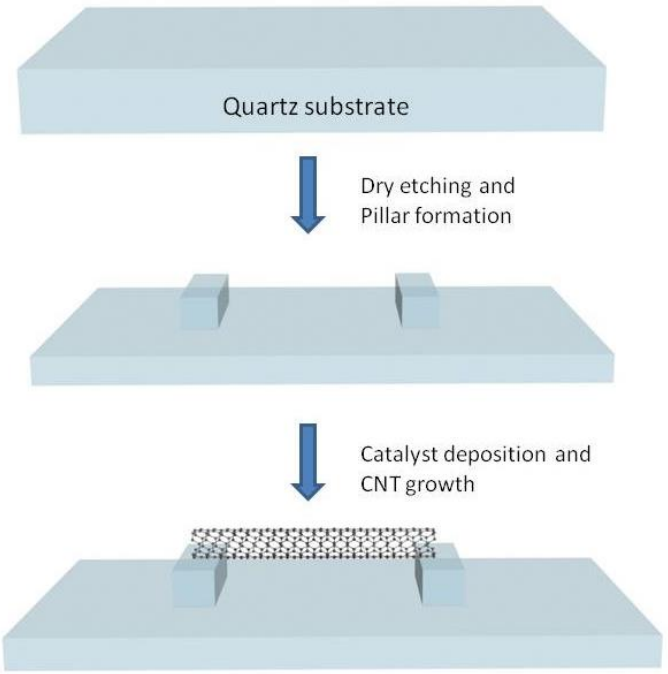

Figure 4.2 Synthesis of SWNTs across the quartz pillars.

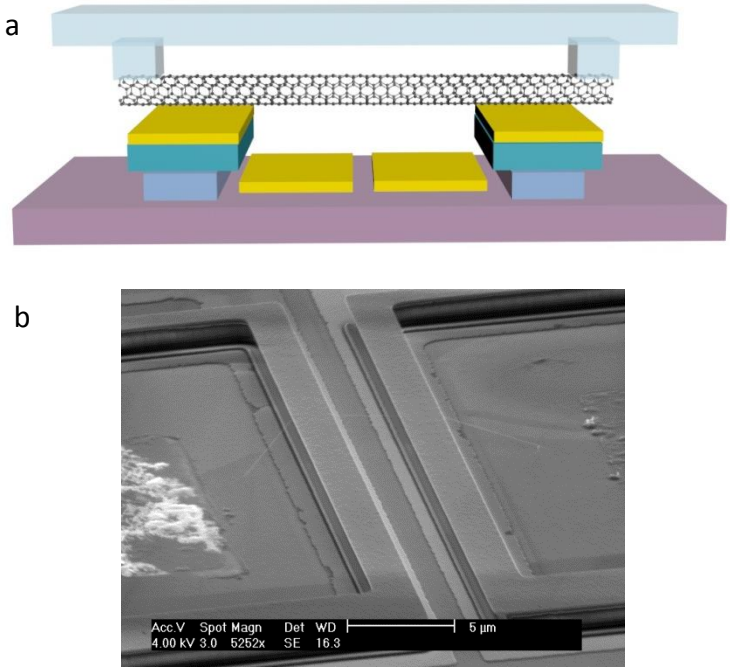

Figure 4.3 One step direct transfer technique [7]. (a) This schematic drawing shows the procedure of transferring a SWNT from the quartz pillars to the pre-patterned substrate. (b) SEM image of the suspended SWNT device fabricated by our one step transfer technique.

4.2.2 Electrical characterization

We first characterize electrical gate response of our fabricated devices. By sweeping bottom gate voltages, metallic nanotube devices demonstrate ambipolar behavior (Fig. 4.4a), while semiconducting nanotube devices show unipolar p-type FET transport with ON/OFF ratio larger than 4 orders of magnitude (Fig. 4.4b). This unipolar electrical response stems from nanotube/metal Schottky barriers, which block the transport of electrons. Importantly, all the devices show negligible hysteresis, indicating the suspended SWNTs are not affected by the surface states. In addition, all the devices are very conducting when operated at the ON state. This suggests the transferred SWNTs could have good electrical contact without requiring any additional annealing process. In this work, we will concentrate on utilizing this special device structure and semiconducting SWNTs to demonstrate diverse device concepts.

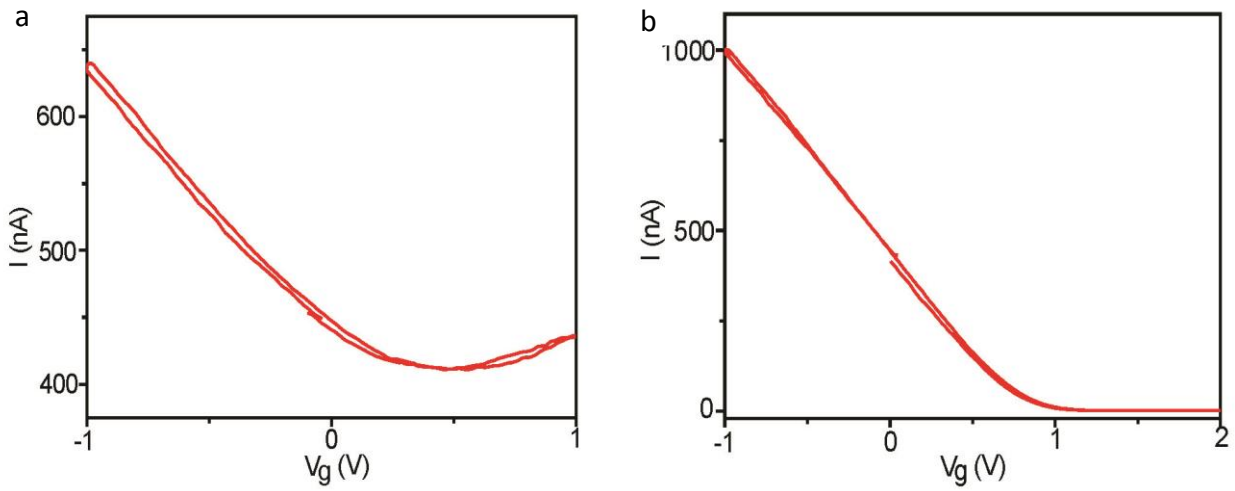

Figure 4.4 The measured electrical gate responses from (a) a metallic SWNT and (b) a semiconducting SWNT device respectively. Both devices show negligible hysteresis due to the fully suspended structure.

4.3 Carbon nanotube p-n diode

4.3.1 Tunable turn-on voltages in the forward bias region

Fig. 4.5a schematically shows our fully suspended SWNT diode. As we can see, the nanotube is suspended between cathode and anode electrodes and located 1.5 μm above the bottom gate electrodes. 30-nm-thick gold is used as a nanotube contact metal. A pair of split gates V_{g1} and V_{g2} are separated by 4 μm and used to electrostatically dope the SWNT.

This proposed device structure can be configured as a p-n diode. Positive V_{g1} and negative V_{g2} electrostatically dope nanotube sections above the split gates into n and p type, respectively. The formation of the p-n junction leads to the rectified *I-V* curves which turn on at forward bias direction. Interestingly, when holding V_{g2} at a constant voltage of 4 V and increasing V_{g1} from 2 to 9 V, the rectified *I-V* curves shift gradually toward higher turn-on voltages while maintaining the same nonlinearity (Fig. 4.5b). The extracted turn-on voltages show linear dependence on the split gate voltage V_{g1} (Fig. 4.5c), with maximum value exceeding 4.3 V. The average diameter of our CVD synthesized SWNTs is around 1 nm, corresponding to a electronic band gap energy ~0.7 eV. Thus, the turn-on voltage of a SWNT diode can exceed 6 times the nanotube band gap voltage. We also studied the diode characteristics under constant V_{g1} of 4 V and varying V_{g2} from -2 to -9 V (Fig. 4.5d). As V_{g2} decreases to more negative voltages, the turn-on voltages drop from 2.6 to 0.5 V. The extracted turn-on voltages again show linear dependence on the amplitude of split gate voltage, V_{g2}, but with a negative slope (Fig. 4.5e). Importantly, the observed gate-controlled tunability and the beyond-band-gap voltage rectification are not possible in conventional diodes.

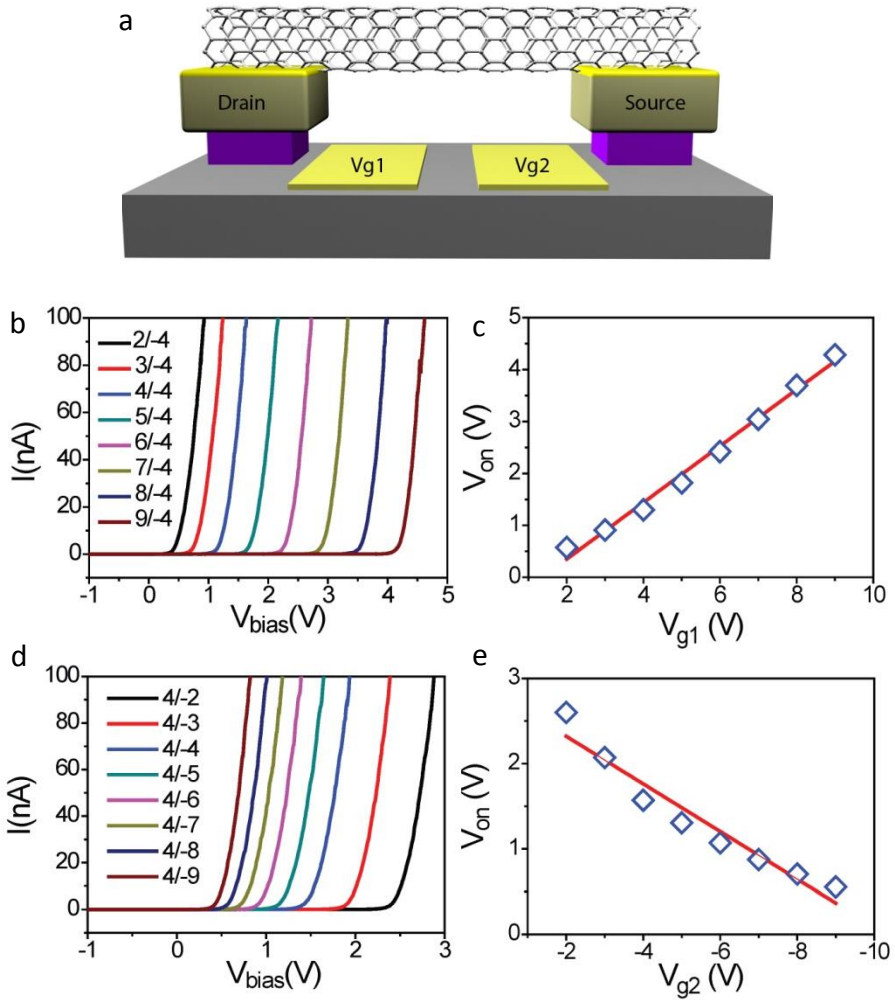

Figure 4.5 A fully suspended SWNT diode with tunable turn on voltages. (a) Schematic drawing of a fully suspended SWNT diode. (b) *I-V* characteristics of the SWNT diode measured for different V_{g1} gate bias voltages. V_{g2} is biased at constant voltage of 4 V, with V_{g1} voltage increasing from 2 to 9 V. (c) The dependence of turn-on voltages on V_{g1} gate voltages. (d) *I-V* characteristics of the SWNT diode measured for different V_{g2} gate bias voltages. V_{g1} is biased at constant voltage of 4 V, with V_{g2} voltage decreasing from -2 to -9 V. (e) The dependence of turn-on voltages on V_{g2} gate voltages.

4.3.2 Device physics of the tunable turn-on property

In order to understand the unique adjustable turn-on voltages in a SWNT diode, we first evaluate the possibility of a tunable and above-band-gap built-in junction potential due to electrostatic gating. For a typical p-n diode, the built-in potential is determined by the Fermi-level difference across the junction, which in our case can be tuned by the split gate voltages. As a result, a greater potential difference between V_{g1} and V_{g2} will induce a higher built-in potential barrier and hence a larger diode turn-on voltage. This prediction agrees with the results shown in the Fig. 4.5b but opposes the results shown in the Fig. 4.5d. Furthermore, the turn-on voltage of the nanotube diode can exceed 4 V. To achieve this high built-in potential, the nanotube would have been degenerate doped into a third subband in both n and p sections. However, with the small gate capacitance of our fully suspended device, $\sim 7 \times 10^{-18}$ F/μm estimated by the geometry, the Fermi level can only be shifted to the first subband edge under 10 V gate voltage. Therefore, the nanotube diode turn-on voltage cannot be simply explained by the junction built-in potential as in a conventional semiconductor diode. In order to understand the *I-V* characteristics of our devices, it is necessary to examine the injected carriers from the complete band diagram including metal/nanotube contacts. For a fully suspended nanotube diode, the p-n junction can be formed by electrostatic doping using the split gates, and in addition, the Schottky junction will be also formed at the metal/nanotube interfaces. With high work function metal Au as the contact, there will be a Schottky barrier for electron injection while hole injection remains Ohmic. Previous studies have shown that the Schottky barrier width of the metal/SWNT interface can be significantly reduced when the nanotube is coupled with the gate electrode through thin high-κ dielectrics [12, 16-17]. Thus, thermally assisted tunneling for both electrons and holes can be enhanced for a thin enough barrier. However, strong electron tunneling through

Schottky barrier is less likely for our fully suspended nanotube devices with small gate capacitance and weak gate coupling. As a consequence, holes injected from the anode are the dominating carriers for current flow under forward bias.

The energy band diagram under equilibrium is illustrated in Fig. 4.6a (black). For a conventional diode with Ohmic contact, forward bias voltage reduces the potential barrier for carrier injection across the junction and leads to exponential increase in diode current. In our device, however, forward bias voltage first drops across the n-side Schottky junction instead of the p-n junction. The diode current is determined by the recombination of injected holes with electrons in the n-region. When the effective length of the n-region *ln* is much greater than the hole minority carrier diffusion length *Lp*, the diode current will remain more or less constant. Further increase in forward bias will reduce *ln*, and when *ln* approaches *Lp*, *ln*~ *Lp*, the injected holes can be swapped across the Schottky junction under large field, and the diode will start turning on (Fig. 4.6b). To confirm this prediction, we plot diode *I- V* curves in log scale, and as shown in Fig. 4.6c, the diode current indeed remains roughly constant until forward bias reaching the turn on threshold voltage. Furthermore, *ln* can also be modulated by the effect of fringing field from V_{g1} and V_{g2}. More positive V_{g1} increases the electron doping concentration, and at the same time increases *ln* (Fig. 4.6a, blue), leading to a larger diode turn-on voltage. On the other hand, more negative V_{g2} increases the hole doping concentration but reduces *ln* (Fig. 4.6a, yellow), leading to a smaller turn-on voltage. Our experimental results presented in the Fig. 4.5b-e once again agree with the prediction. These results confirm that the turn-on voltage tuning in the fully suspended SWNT diodes is achieved by modulating hole extraction in the n-doped region.

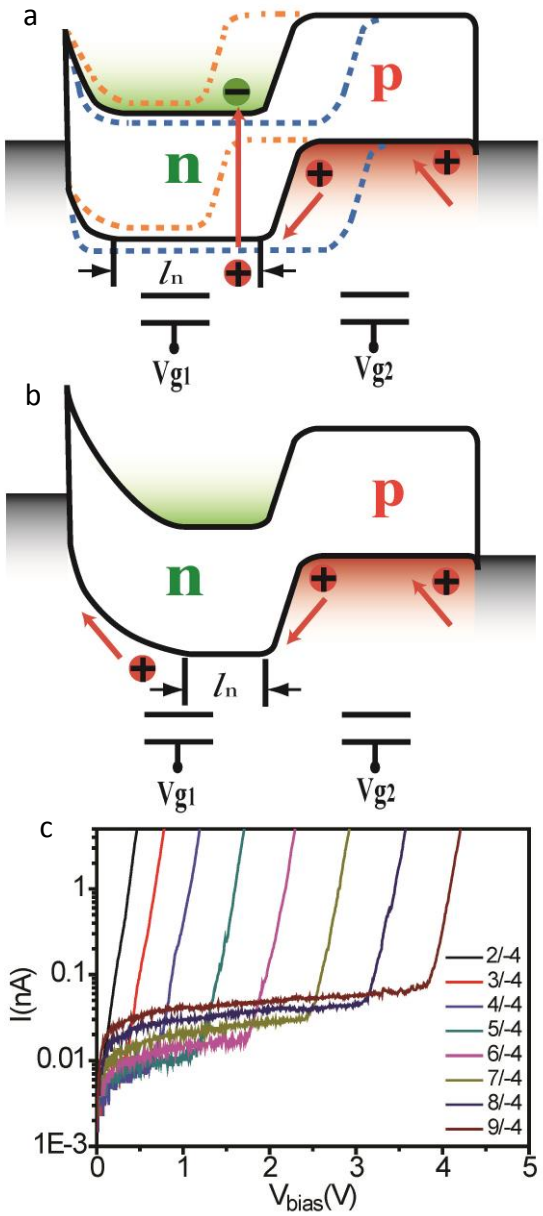

Figure 4.6 Band diagram of a fully tunable SWNT diode. (a) Energy band diagram of the SWNT diode under equilibrium (black line). *ln* denotes the n channel length. *ln* increases with higher V_{g1} gate voltage (blue line), and decreases with lower V_{g2} gate voltage (yellow line). When *ln* is much greater than the hole minority carriers diffusion length *Lp*, the hole injected across the junction is recombined with an electron. (b) Energy band diagram under forward bias voltage. The external bias voltage causes band bending in the n section and reduces *ln*. Once *ln* becomes comparable to *Lp*, the injected hole will be swapped to the left contact by the electric field, and the p-n junction will be turned on. (c) Log scale plot of the same *I-V* curves shown in Fig. 4.5b.

4.4 Carbon nanotube backward diode

4.4.1 Tunable leakage current in the reverse bias region

We also explored the tunability of reverse bias characteristics for the fully suspended SWNT diode. For conventional p-n diodes, tunneling current is usually suppressed due to the width of space charge region, which is made out of immobile donor and acceptor ions. In contrast, for electrostatically doped nanotube p-n diodes, all charges are mobile carriers and they tend to accumulate at the interface. Therefore, by bringing two split gates closer and/or applying higher gate voltages to create a sharper p-n junction, it is possible to strongly enhance the band-to-band tunneling current [13, 18].

Fig. 4.7 shows the *I-V* curves for another fully suspended SWNT diode with split gate separation of 1 μm. V_{g2} is held at constant potential of 3 V, while V_{g1} is increased from 6 to 10 V. In the forward bias region, this diode exhibits similar tunability as the device shown earlier. However, the reverse bias leakage current is strongly enhanced by 50 times compared to previous device with 4 μm split gate separation. Moreover, leakage current increases with increasing gate voltage of V_{g1}. These results agree with enhanced band-to-band tunneling across a sharper p-n junction under reverse bias. More careful examinations of reverse bias *I-V* reveal that the tunneling current increases exponentially from 0 to 0.2 V and then grows linearly at higher reverse bias voltage (Fig. 4.7, inset).

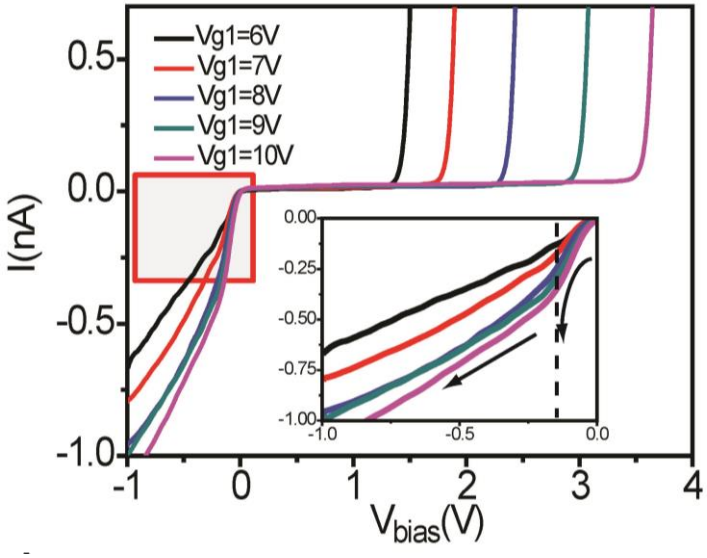

Figure 4.7 Tunable leakage current in the reverse bias region. The inset shows the zoom-in view of the reverse bias region.

4.4.2 Device physics of tunable leakage current

To explain this unusual *I-V* relation, we use Fermi's golden rule to model the band-to-band tunneling current in SWNTs. Fig. 4.8a depicts the simulated band diagram under different equilibrium. Fermi level is initially near the band edge of the p side, and by changing V_{g1} gate voltage, doping level in the n side (ΔE) can be modulated. When applying reverse bias voltage, the system is out of equilibrium and band-to-band tunneling current can be modeled as below:

$$I_{\text{tunneling}} \alpha \int_{E_{cn}}^{E_{vp}} \big(F_c(E) - F_v(E)\big) T N_c(E) N_v(E) dE \quad (4.1)$$

Here, $F_c(E)$ and $F_v(E)$ are Fermi-Dirac distribution functions at room temperature, and T is the tunneling probability through the junction potential barrier. $N_c(E)$ and $N_v(E)$ are DOS of carbon nanotube for the conduction band and valence band, respectively.

From the equation, we can see that tunneling current is determined by the overlap integral

of DOS ($\int N_c(E)N_v(E)$), modulated by Fermi energy difference ($\int F_c(E)-F_v(E)$) between p and n side. The overlap DOS has maximum value at the band edge due to Van Hove singularity. Therefore, under small reverse bias voltage, Fermi-level of p side (E_{Fp}) shifts across the region with high overlap DOS. The tunneling junction is highly conducting. As reverse bias increases, E_{Fp} shifts into the low overlap DOS region, causing tunneling current increases linearly with increasing bias. Our simulation results are plotted in Fig. 4.8b. The curve shows similar *I-V* characteristics, with a nearly exponential current increase due to larger DOS at van Hove singularity, and then followed by linear dependence under higher reverse bias voltage. In addition, *I-V* curve shifts toward downward direction by increasing doping level in the n side (Fig. 4.8c), which is in good agreement with our experimental curves as shown in Fig. 4.7.

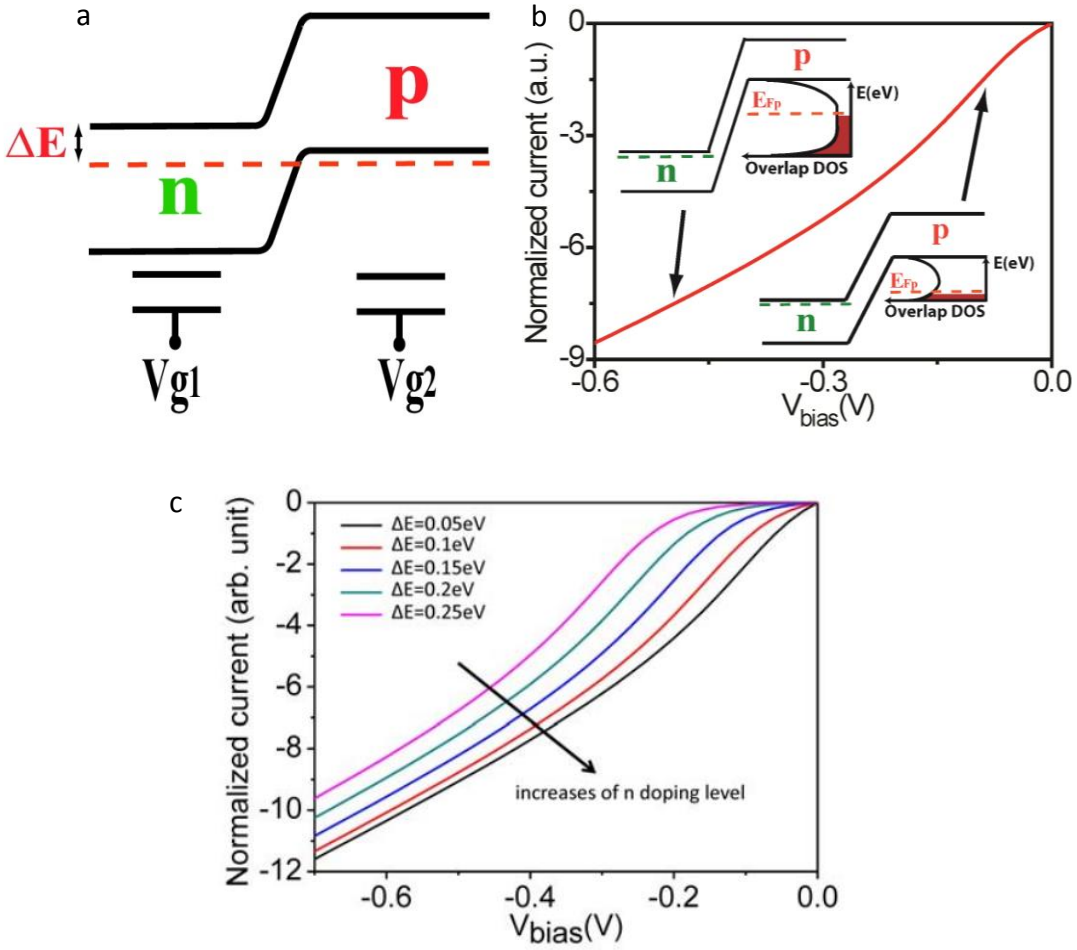

Figure 4.8 Simulation of band to band tunneling in a SWNT. (a) Energy band diagram under equilibrium with gate-controllable n doping level (ΔE). (b) Simulated band-to-band tunneling current for the one-dimensional SWNT diode. The inset shows the overlap DOS under small and large reverse bias voltages, respectively. (c) Simulated band-to-band tunneling current under different n doping levels.

4.4.3 Electrical characteristics of a carbon nanotube backward diode

Another peculiar consequence arising from the enhanced band-to-band tunneling is that, the reverse bias current can be much greater than forward bias current within small voltage range. One representative *I-V* curve is shown in Fig. 4.9 with V_{g1} = 6 V and V_{g2} = -6 V. The forward bias current is suppressed below 10 pA with V_{bias} up to 1 V, the consequence of minimized hole extraction. Interestingly, the reveres bias current increases exponentially to 150 pA at V_{bias} = -0.23 V, which is 30 times greater than the forward bias current. The results are in strong reminiscence of a backward diode [15], which is highly resistive under forward bias but conducts under reverse bias. It is notable that our SWNT backward diode has large turn-on voltage (~1 V) and small leakage current (~5 pA) in the forward bias region, both of which are desirable for backward rectification. Most importantly, fast increasing tunneling current in the reverse bias region leads to large zero-bias nonlinearity, which is especially challenging to achieve for conventional semiconductor backward diodes [15]. We further calculate the nonlinear curvature coefficient, γ, which is defined as $\gamma = (\frac{\partial^2 I}{\partial^2 V})/(\frac{\partial I}{\partial V})$ (Fig. 4.9, inset). At zero bias voltage, the nanotube backward diode exhibits a curvature coefficient of 34.3 V, approaching the thermionic limit value of γ = q/KT = 38.5 V at 300 K. At V_{bias} ~ 15 mV, γ can even go beyond the thermionic limit and reach a maximum value of 46.4 V. These results suggest a remarkable potential for SWNT backward diode applications in high-speed switching, microwave mixing and detection, and small amplitude rectification [19-20].

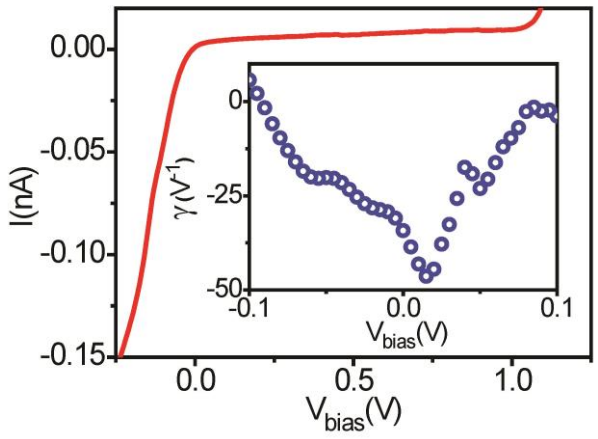

Figure 4.9 The backward diode with curvature coefficient exceeding an ideal diode. By applying proper gate voltages, the *I-V* characteristics of the SWNT diode show backward rectification behavior. The inset shows the measured curvature coefficient γ versus bias voltage. The maximum curvature coefficient exceeds the theoretical value for an ideal diode.

4.5 Conclusions

In this chapter, we presented fully tunable single-walled carbon nanotube diodes fabricated by the simple one-step transfer technique. By characterizing their electric properties, we have seen that these devices could show gate-controlled tunability in both forward and reverse bias regions and we also found these tunable behaviors are directly related to the properties of nanoscale junctions in a SWNT. Importantly, the development of these tunable diodes would open up new opportunities for programmable nanoelectronic or nanophotonic circuits in the near future.

References:

[1] R. Chau et al., Nat. Mater. 6, 810 (2007).

[2] G. D. Dresselhaus, G. Dresselhaus, and P. Avouris, Springer-Verlag: Berlin (2001).

[3] P. Avouris, Z. H. Chen, and V. Perebeinos, Nat. Nanotechnol. 2, 605 (2007).

[4] P. Avouris, M. Freitag, and V. Perebeinos, Nat. Photonics 2, 341 (2008).

[5] J. U. Lee, Appl. Phys. Lett. 87, 073101 (2005).

[6] J. U. Lee, Phys. Rev. B 75, 075409 (2007).

[7] C. C. Wu, C. H. Liu, and Z. H. Zhong, Nano Lett. 10, 1032 (2010).

[8] J. Chen et al., Science 310, 1171 (2005).

[9] T. Mueller et al., Nat. Nanotechnol. 5, 27 (2010).

[10] N. M. Gabor et al., Science 325, 1367 (2009).

[11] J. Appenzeller et al., Phys. Rev. Lett. 93, 196805 (2004).

[12] J. Appenzeller et al., Phys. Rev. Lett. 92, 048301 (2004).

[13] D. Jena et al., Appl. Phys. Lett. 93, 112106 (2008).

[14] F. Leonard, and J. Tersoff, Phys. Rev. Lett. 85, 4767 (2000).

[15] S. M. Sze. and K. K. NQ, Wiley:New York (2006).

[16] S. Heinze et al., Phys. Rev. Lett. 89, 106801 (2002).

[17] J. Appenzeller et al., Phys. Rev. Lett. 89, 106801 (2002).

[18] J. Knoch, and J. Appenzeller, Phys. Status Solidi A-Appl. Mat. 205, 679 (2008).

[19] J. N. Schulman, and D. H. Chow, IEEE Electron Device Lett. 21, 353 (2000).

[20] S. Y. Park et al., Electron. Lett. 43, 295 (2007).

Chapter 5

Hot Carrier Generation and Extraction from Graphene

5.1 Introduction

Converting the photon energy into an electrical current is a multistep process, which involves the interactions between photons, electrons and phonons. Understanding these energy conversion processes is at the heart of developing optoelectronics. Thus far, a variety of research groups studied the mechanisms of photocurrent generation from either graphene p-n junctions or graphene/metal junctions under CW laser excitation [1-6]. Their studies revealed that photocurrent generation could be governed by two mechanisms: Photovoltaic effect and Photo-thermoelectric effect (PTE) as described in chapter 2. On the other hand, femtosecond techniques have been constantly adopted to probe hot carrier dynamics within the graphene junctions in order to understand the process of the energy of a photon into electricity [7-11].

In this chapter, we will look into the hot carrier photoresponse from the graphene junctions further. We first present our measured photoresponse from graphene p-n and graphene/metal junctions under CW and femtosecond pulse laser excitation. Interestingly, we see the striking differences between CW and pulse excitation. This indicates the mechanism of

photocurrent generation could be strongly altered by hot carrier population and dynamics. Furthermore, we observe the formation of photo-Dember field when exciting graphene/metal interfaces with the pulse laser. We will elaborate that when photocurrent generation is mainly contributed by the photo-Dember field, the polarity of photocurrent is related to electron-hole mobility of graphene and the amplitude of photocurrent is determined by hot carrier cooling rate. These signatures are significantly different from the conventional mechanisms of photocurrent generation from graphene.

5.2 Device fabrication and electrical characterization

Our present graphene devices consist of a pair of split bottom gates, which can electrostatically dope the graphene in the above sections respectively, and form the p-n junction in between. In this section, we introduce the fabrication steps of graphene devices.

As shown in Fig. 5.1, we first patterned the two split bottom gates on top of 300-nm-thick silicon dioxide. The pair of split gates is separated by 1 μm and is composed of 5 nm/30 nm Ti/Au metals. This substrate was then covered by 50-nm-thick Al_2O_3 deposited by atomic layer deposition (ALD). Here, Al_2O_3 serves as the back gate oxide and its high dielectric constant ($\varepsilon \sim 7.5$) leads to a strong gate coupling, which can efficiently tune the Fermi energy of graphene. After fabricating this pre-patterned substrate, the next step was to transfer single layer graphene on top of it. The graphene was synthesized by CVD method and single-layer nature of the graphene was identified by Raman spectroscopy [12-13]. We then patterned the transferred graphene into an array of rectangular channels using lithography and a 30 second oxygen plasma etch. The remaining photoresist on graphene channels was removed by soaking the samples in acetone for 4 hours, then in PRS2000 for another 10 minutes. To make electrodes to contact the

graphene channels, a third step photolithography was used to pattern source and drain contacts, and Ti/Au (5/50 nm) was deposited by electron beam evaporation. Finally, the entire graphene device was covered by 50-nm-thick Al_2O_3 deposited by ALD. The purpose of depositing this passivation layer is to prevent the graphene channels from absorbing ambient moisture. Notably, this not only can suppress the hysteresis of electrical gate response but also can shift the doping level to the neutral point.

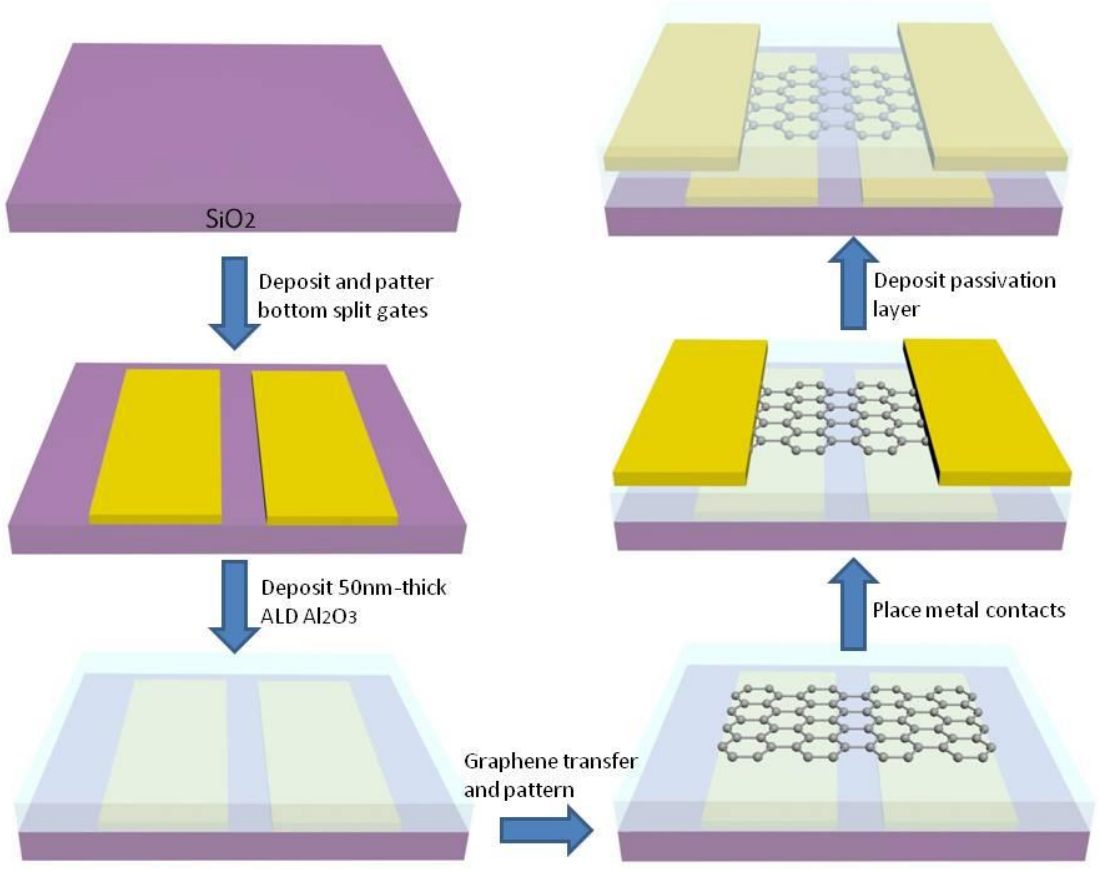

Figure 5.1 Fabrication procedure of the split-gate graphene device.

We further characterize electrical properties of our dual-gate devices. Fig. 5.2 shows the change of resistance, R, as a function of bottom gate voltages, V_{g1} and V_{g2}, indicating two buried

gates can independently control carrier type and density in their above graphene sections. The straight horizontal and vertical gray dashed lines correspond to charge neutrality points of graphene and these lines divide the entire resistance plot into four regions, denoted as p-p, p-n, n-p and n-n junctions.

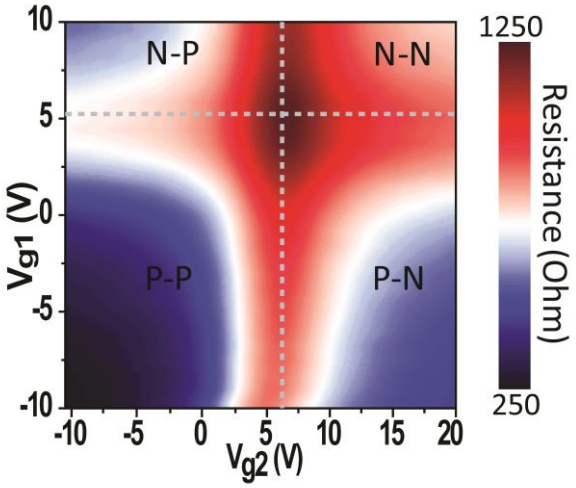

Figure 5.2 The measured resistance as a function of V_{g1} and V_{g2}.

5.3 Scanning photocurrent spectroscopy of graphene devices

We next utilize the scanning photocurrent spectroscopy as described in section 3.4 to explore the photoreponse of our graphene devices under different gate bias conditions. Fig. 5.3a shows the schematic of our experimental setup. We raster scan the excitation laser across the device and simultaneously measure the photocurrent and reflected light intensity. Both CW (λ= 900 nm) and femtosecond pulsed laser (λ = 800 nm) are used, and the focused laser spot sizes are around 1.5 μm. The top inset in Fig. 5.3b shows a spatially resolved photocurrent map with CW excitation under zero source-drain and gate bias voltage. Photocurrent peaks at the source and drain metal-graphene contacts, confirmed by overlapping with the reflected light intensity

mapping (Fig. 5.3b, bottom inset). The electrical gate response of the studied device is also measured. As shown in Fig. 5.3b, resistance versus split gate voltage scans exhibit consistent ambipolar gate responses for both gates and a Dirac point gate voltage of ~4.8 V.

We then turn our attention to the gate-dependent photocurrent mapping across the length of the device (dotted line in the top inset of Fig. 5.3b) with both CW and pulse laser excitation. Fig. 5.3c-d show photocurrent versus V_{g2} and laser position for CW and femtosecond pulse excitation, respectively. V_{g2} is scanned from -10 to 20 V with V_{g1} grounded during the measurement, modulating the graphene device from p-p junction to p-n junction. Significantly, two distinct differences are observed by comparing the CW versus pulse laser excited photocurrent maps. First, photocurrent peaks at the p-n junction between the split gates with CW excitation (Fig. 5.3c, position = 2.5 μm) but disappears when excited with pulse laser (Fig. 5.3d, position = 2.5 μm). Second, photocurrent near the left metal/graphene junction also shows drastic difference for CW and pulse excitation. Under CW excitation, photocurrent switches sign at V_{g2} =7.5 V (Fig. 5.3c, position = 0 μm). Surprisingly, with pulse excitation, photocurrent remains positive, and peaks at V_{g2} = 5 V (Fig. 5.3d, position = 0 μm). The same phenomena are also observed at the right metal/graphene contact when tuning V_{g1} gate voltages with V_{g2} grounded and reproducible among all devices tested. In the following sections, we will explain these observations in detail.

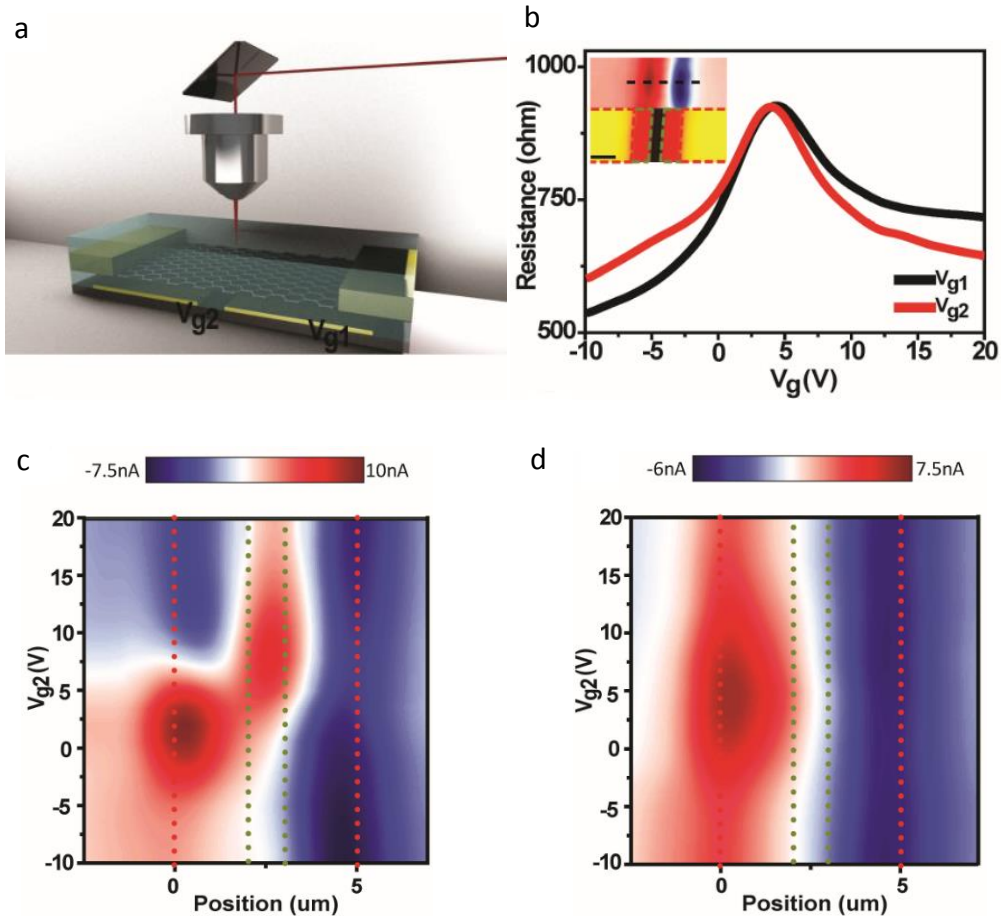

Figure 5.3 Striking difference for photocurrent generation in graphene between CW and pulse laser excitation. (a) Schematic drawing of the graphene device and experimental setup. (b) Gate response of the device with V_{sd} = 1 mV. The black curve shows V_{g1} gate dependence with V_{g2} grounded, and the red curve shows V_{g2} gate dependence with V_{g1} grounded. The top inset shows a spatially resolved two-dimensional photocurrent map with zero source-drain and gate bias voltage. The bottom inset shows optical reflection intensity map of the same graphene device. The red dashed lines indicate the boundary of the source and drain contacts, and the green dashed lines indicate the boundary of split bottom gates. Scale bar, 2 μm. (c) Gate-dependent photocurrent map under 3.8 mW CW laser excitation. (d) Gate-dependent photocurrent map under 3.8 mW pulse laser excitation. In both panels c and d, the red dotted lines indicate the source and drain contacts edges, and the green dotted lines indicate the bottom gates edges.

5.4 CW versus pulse excitation in graphene

The significant differences of photoresponse as described above reveal pulse excitation is different from CW excitation in nature. Under pulse excitation, a high flux of photon excitation will suddenly create an excess amount of hot carriers. The relaxation of these hot carriers through scattering with optical phonon will quickly raise the optical phonon temperature to near hot carrier temperature (~hundreds to thousands of Kelvin), which becomes the bottleneck for thermal relaxation of hot carriers [8, 14]. These processes lead to nonequilibrium hot carriers with elevated quasi-Fermi level right after the excitation (Fig. 5.4a). Eventually, hot carriers relax back to thermal equilibrium via acoustic phonon emissions before the next pulse arrives. In contrast, under CW illumination, excitation energy is averaged over the period of time instead of being confined within femtosecond pulses. As a result, the system is operated under the steady state and photocarriers relax rapidly and accumulate near the equilibrium Fermi level, resulting in lower electron temperature (Fig. 5.4b).

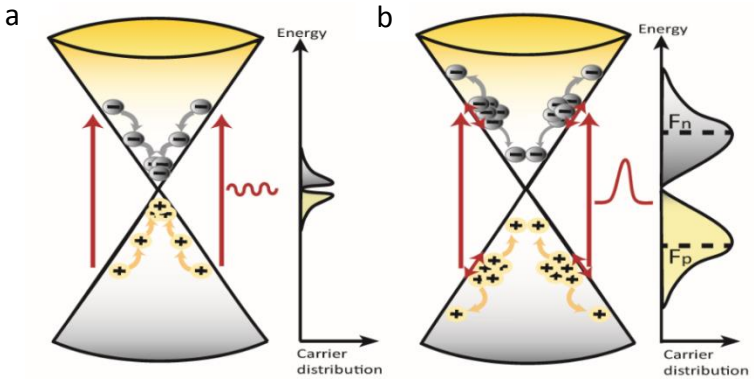

Figure 5.4 Hot carrier dynamics under CW and pulse excitation. (a) Schematic drawing of near equilibrium carrier distribution under CW laser excitation. (b) Schematic drawing of nonequilibrium hot carrier distribution under pulse laser excitation.

5.5 Mechanisms of photocurrent generation from graphene p-n junctions

CW excitation

In this section, we focus on understanding the mechanisms of photocurrent generation from graphene p-n junctions. To clarify this, we first compare the experimental data with simulations of field-driven carrier transport and PTE-originated transport. Based on the split gate responses of the device, we can calculate gate-dependent thermopower (Fig. 5.5a) using the Mott formula [4, 6, 15]:

$$S = \frac{\pi^2 k_B^2 T}{3e} \frac{1}{G} \frac{dG}{dV_g} \frac{dV_g}{dE}\Big|_{E=E_f} \quad (5.1)$$

where S is thermopower and G is conductance. If photocurrent is originated from PTE effect, then it is expected that photocurrent is proportional to the thermal power difference, ΔS, across the p-n junction, as plotted in Fig. 5.5b. However, if the photocarrier transport is field-driven, then the photocurrent is expected to follow the Fermi energy difference across the p-n junction. The relation between gate voltage (V_g) and graphene Fermi energy (E_f) is as below:

$$E_f = \hbar v_F \left(\sqrt{\pi C (V_g - V_g^0)/e} \right) \quad (5.2)$$

where v_F is the Fermi velocity, C is back gate capacitance and V_g^0 is denoted as gate voltage at the Dirac point. Based on these equations, we simulated the Fermi energy difference across the junction under different gate voltages using the split gate responses and plotted it in Fig. 5.5c.

The measured split gate voltage-dependent photocurrent under 2 mW CW excitation is plotted in Fig. 5.5d. Clearly, the change of photocurrent polarity and peak show excellent agreement with the simulation result of Fig. 5.5b, indicating PTE dominates photocurrent generation in the graphene p-n junction.

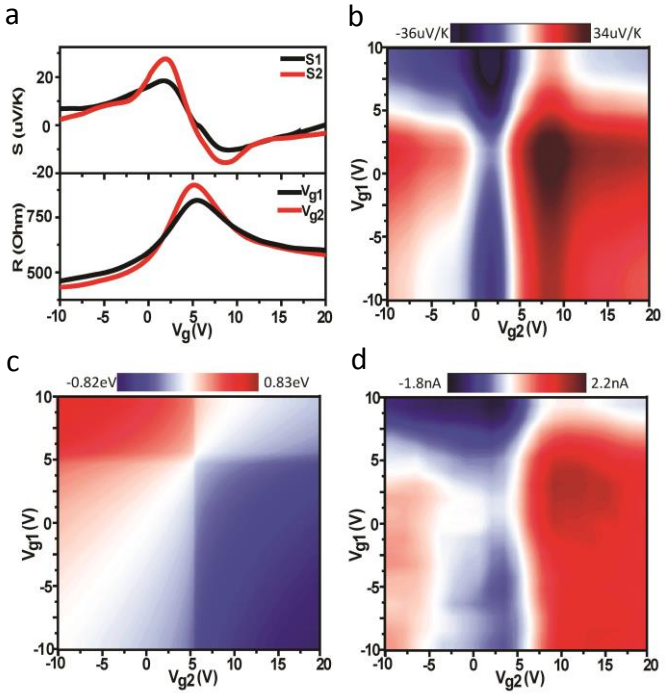

Figure 5.5 Gate-dependent photocurrent generation at the graphene p-n junction under CW excitation. (a) Split gate responses of the device (bottom panel) and the calculated gate-dependent thermopower (top panel). (b) Thermopower difference across the p-n junction under different split gate voltages. (c) Fermi energy difference across the p-n junction under different split gate voltages. (d) Measured gate-dependent photocurrent at the graphene p-n junction under 2 mW CW excitation.

Pulse excitation

We also investigated the disappearance of photocurrent at the graphene p-n junction under femtosecond pulse laser excitation, as previously shown in Fig. 5.3d. To exclude the effect of gate biasing, we reversed the gate biasing condition by sweeping V_{g1} with V_{g2} fixed at 0 V. Again, there is no photocurrent generation from the p-n junction (Fig. 5.6a). Complete dual gate sweeps with pulse laser excitation at the p-n junction show almost no photocurrent regardless of the dual gate voltages, as evident in Fig. 5.6b. This result further corroborates the hot carrier nature of the photocurrent generation in graphene. Under pulse excitation, there is no hot carrier

temperature gradient across the p-n junction due to the overheating phonon temperature, and PTE photocurrent is significantly suppressed as a result [16].

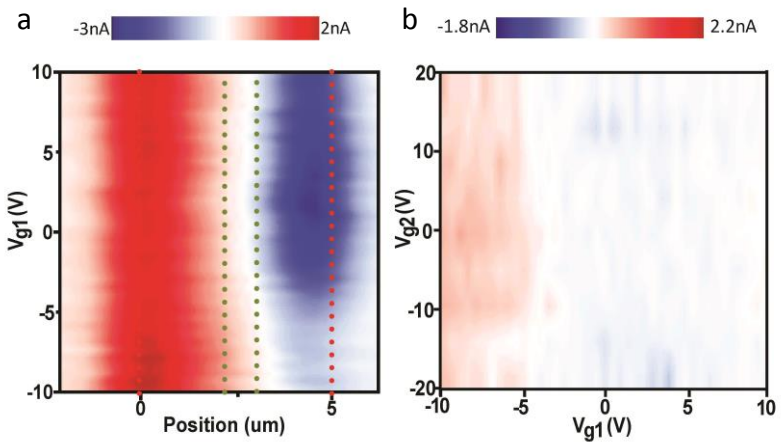

Figure 5.6 Gate-dependent photocurrent generation at the graphene p-n junction under pulse excitation. (a) V_{g1} gate-dependent photocurrent map of the device under 2 mW pulse excitation. Here V_{g2} is grounded. (b) Dual gate-dependent photocurrent map with pulse laser excitation at the graphene p-n junction.

5.6 Mechanisms of photocurrent generation from graphene/metal junctions

CW excitation

We next focused our attention on the photocurrent at the metal/graphene contact under CW laser excitation. Fig. 5.7 shows the gate-dependent photocurrent at the contact edge extracted from Fig. 5.3c at position = 0 μm. From here, we can see the photocurrent excited by the CW laser switches sign at V_{g2}= 7.5 V, agreeing with the literature where work function difference between graphene and metal determines the sign of photocurrent [2-3, 5, 17]. On the basis of the thickness of the gate dielectric (50 nm Al_2O_3, ε ~ 7.5) and the Dirac point voltage, we estimate a metal work function of 4.3 eV, consistent with the typical value for our contact metal Ti. Therefore, we conclude that built-in field is the dominated mechanism for photocurrent

generation.

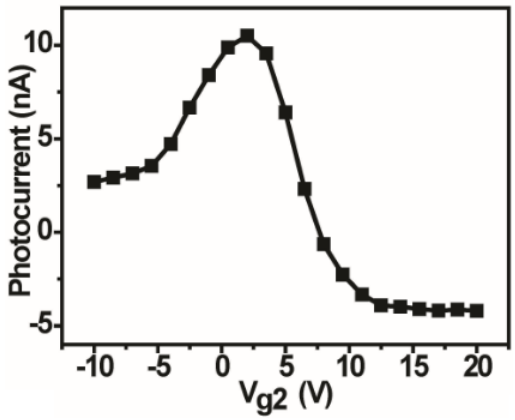

Figure 5.7 Gate-dependent photocurrent at the metal contact edge under CW laser excitation.

Pulse excitation

In comparison, photocurrent excited by the pulse laser shows significant difference from CW laser excitation. We again extract the gate-dependent photocurrent at the contact edge from Fig. 5.3d at position = 0 μm and show it in Fig. 5.8. Importantly, photocurrent remains positive throughout the gate voltage sweep and peaks at V_{g2} = 5 V, which coincides with the Dirac point gate voltage. Furthermore, the photocurrent curve exhibits nearly symmetrical decay around V_{g2} = 5 V by increasing either hole density or electron density. The signature lacking of photocurrent polarity reversal hints a different mechanism of hot carrier extraction. In the next section, we will explain this unusual photoresponse is related to the formation of ultrafast Photo-Dember field in detail.

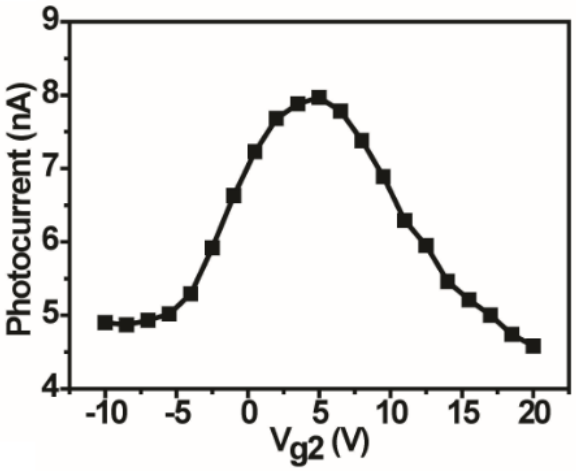

Figure 5.8 Gate-dependent photocurrent at the metal contact edge under pulse laser excitation.

5.7 Hot carrier extraction induced by the ultrafast photo-Dember electric field

5.7.1 Formation of the photo-Dember electric field in graphene

The photo-Dember effect is a transient dipole radiation process, typically applied for terahertz (THz) generation [18]. The most common experiment is to excite a freestanding bulk GaAs ($\mu_e = 8500\ {}^{cm^2}/_{Vs}$, $\mu_h = 400\ {}^{cm^2}/_{Vs}$) or InAs ($\mu_e = 30000\ {}^{cm^2}/_{Vs}$, $\mu_h = 240\ {}^{cm^2}/_{Vs}$) with the femtosecond laser. Due to inhomogeneous light absorption and inherently mobility asymmetry, excited hot electrons and holes will diffuse from the surface toward inside with different velocities. This spatial charge separation builds up a transient photo-Dember field, inducing the subsequent dipole radiation perpendicular to the excited surface (Fig. 5.9).

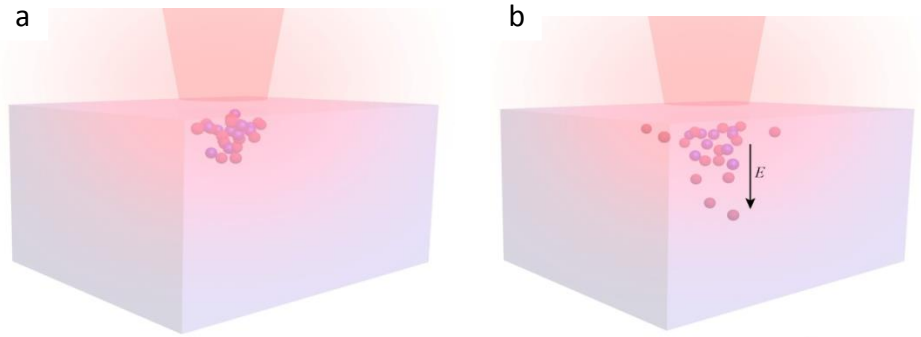

Figure 5.9 Schematic drawing of the formation of photo-Dember field in a bulk semiconductor. (a) Hot carriers initially created by a laser pulse near the excitation surface. (b) After a time delay, hot electrons and holes diffuse into the semiconductor with different velocities, creating a transient photo-Dember field.

In graphene, the same physical picture could not be applied, since photocarriers cannot diffuse out of the graphene plane to build up charge gradient, and importantly, the distinction between electron and hole mobility is insignificant [19-20]. Despite these intrinsic inhibitions, we predict the possibility of creating photo-Dember field when exciting the graphene-metal interface with femtosecond laser. This can be understood via Fig. 5.10 in combination with the following key properties: (1) The incident light partially shadowed by the metal establishes a sharp photocarrier density gradient near the metal edge. This sharp gradient together with 2D spatial confinement cause the hot carriers diffuse into the lateral metal-covered area efficiently [21]. (2) Low electronic specific heat of graphene favors high carrier temperature after excitation [22]. This combined with high carrier mobility will enhance the diffusion coefficient of hot carrier. In fact, these parameters can be connected together through Einstein relation [20]: $D = \frac{\mu K_B T}{2q}$ (5.3)

where D stands for diffusion coefficient, μ is carrier mobility, T is carrier temperature, and K_B is Boltzmann constant. From this relation, we can also see that high temperature is key to increase the difference between electron and hole diffusion coefficient. (3) Strong light coupling within the single atomic layer [23] results in high carrier density in graphene, which could be 1-3 orders higher than other low band gap materials [24]. Importantly, this property will enhance photocarrier density gradient and the ensuing diffusion process. Taken all together, the dynamics of nonequilibrium hot carriers could induce the transient photo-Dember field near the metal contact edge and thereby drive photocurrent flow.

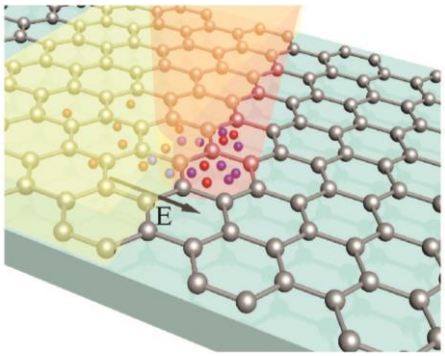

Figure 5.10 Schematic drawing of the formation of photo-Dember field at the graphene-metal interface.

5.7.2 Electron-hole mobility of graphene versus photoresponse

To evidently confirm the formation of photo-Dember field, we utilize scanning photocurrent spectroscopy to study the photoresponse from three graphene devices (A-C) with different electrical properties. Their electrical transport I-V_g curves are shown in Fig. 5.11. From these curves, we can see these devices show slightly electron-hole mobility asymmetry. To gain further insight, we fit each I-V_g curve and extract electron mobility, hole mobility and intrinsic

doping level from each device. The extracted results are summarized in table 1 [25-26]. Specifically, both device A and B are contacted with low working function metal Ti while device C is contacted with high working function metal Pd. Furthermore, device A and C show higher hole mobility than their electron mobility, while device B shows the opposite of property.

Here the asymmetry of electron-hole mobility could be caused by several reasons. One possibility is that the pinning of the charge density below the metal contact leads to a junction at the graphene/metal interface, which affects the electron-hole transport properties [26]. The other possible reason causing the electron-hole asymmetry could stem from the charged impurity scattering. During the fabrication processes, these impurities might be located above or below the graphene layer or even within the substrate. Also, they could be positive or negative charged. But if these positive and negative impurities are in unequal numbers, the different impurity scattering rate between electrons and holes would lead to the asymmetry between electron-hole conductivities [27-28].

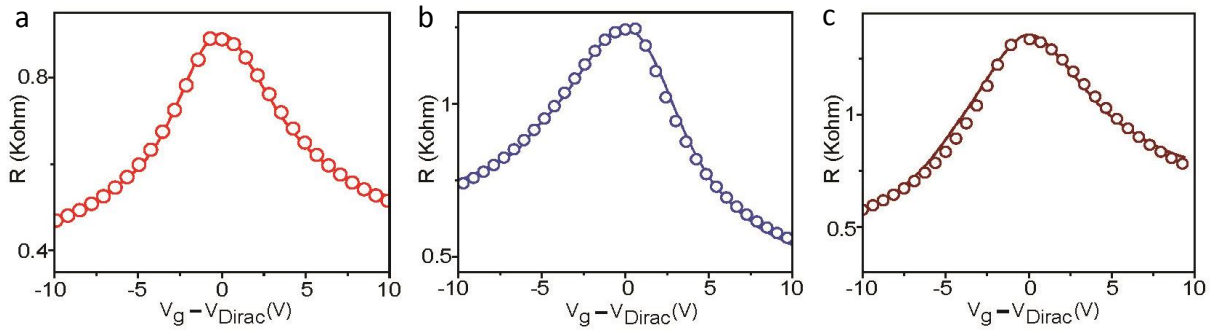

Figure 5.11 Resistance as a function of gate voltage (solid line) and its fitting (round symbols) of the (a) device A (red) (b) device B (blue) and (c) device C (Brown).

Table 1 Electrical properties of the tested devices

	Mobility (cm^2/Vs)			
	μ_e	μ_h	E_f^0 (eV)	Contact metal
Device A	1095	1289	4.72	Titanium
Device B	820	611	4.28	Titanium
Device C	751	925	4.75	Palladium

μ_e, electron mobility; μ_h, hole mobility; E_f^0, instrinsic Fermi level of graphene.

Table 5.1 Electrical properties of graphene transistors shown in Fig. 5.11.

We then focus on probing the photoresponse from these three devices under femtosecond laser excitation. Fig. 5.12a-c are gate-dependent photocurrent maps measured from device A, B and C respectively. By comparing these maps, we not only observe photocurrent generation near the contact edge (position = 0 and 5 um) but also observe three major features. First of all, gate-dependent photocurrent does not show polarity reversal. Second, the polarity of photocurrent from device B is completely opposite to device A and C. Third, regardless of the polarity of photocurrent, the magnitude of photocurrent peaks near the graphene Dirac gate voltage, and decreases by increasing doping concentration. These can be obviously seen by extracting gate-dependent photoresponse from the contact edge (position = 0 um) from three different photocurrent maps as demonstrated in Fig. 5.12d-f.

Notably, these features provide the evidence of creating ultrafast photo-Dember field. For the device A and C, photoexcited hot holes diffuse faster than hot electrons into the metal-covered area due to higher hole mobility, building up a transient photo-Dember field. Essentially, this field drives electrons to the contact, resulting in photocurrent generation. In contrast, holes will be driven to the contact due to higher electron mobility of the device B. Therefore, regardless the contact metals and doping concentration of graphene, the polarity of photocurrent

is decided by the electron-hole mobility, providing a clear evidence of forming the photo-Dember field.

Moreover, when the photo-Dember field is a dominant mechanism for driving photocurrent flow, the amplitude of photocurrent would increase with the hot carrier lifetime. This is not only because the duration of this transient field increases with the lifetime, but also keeping excited carriers at the hot state is central to create a spatial charge distribution. In fact, recent theoretical works predict hot carrier energy relaxation through electron-electron and electron-phonon coupling will be faster by increasing doping concentration in graphene [29-30]. This qualitatively interprets the feature of our gate-dependent photocurrent measurements and we will experimentally confirm the above argument in section 5.7.5.

In addition to pulse excitation, we also study the photoresponse from graphene-metal interfaces under CW laser excitation for comparison. As shown in Fig. 5.12g-i and the inset, photoresponse from these three devices consistently exhibit polarity reversal, in agreement with the photovoltaic effect [2-3]. Importantly, the lack of similar features induced by pulse laser indicates that steady CW excitation would lead to low photocarrier temperature and photocarrier density in graphene. Therefore, the steady photo-Dember field will be insignificant.

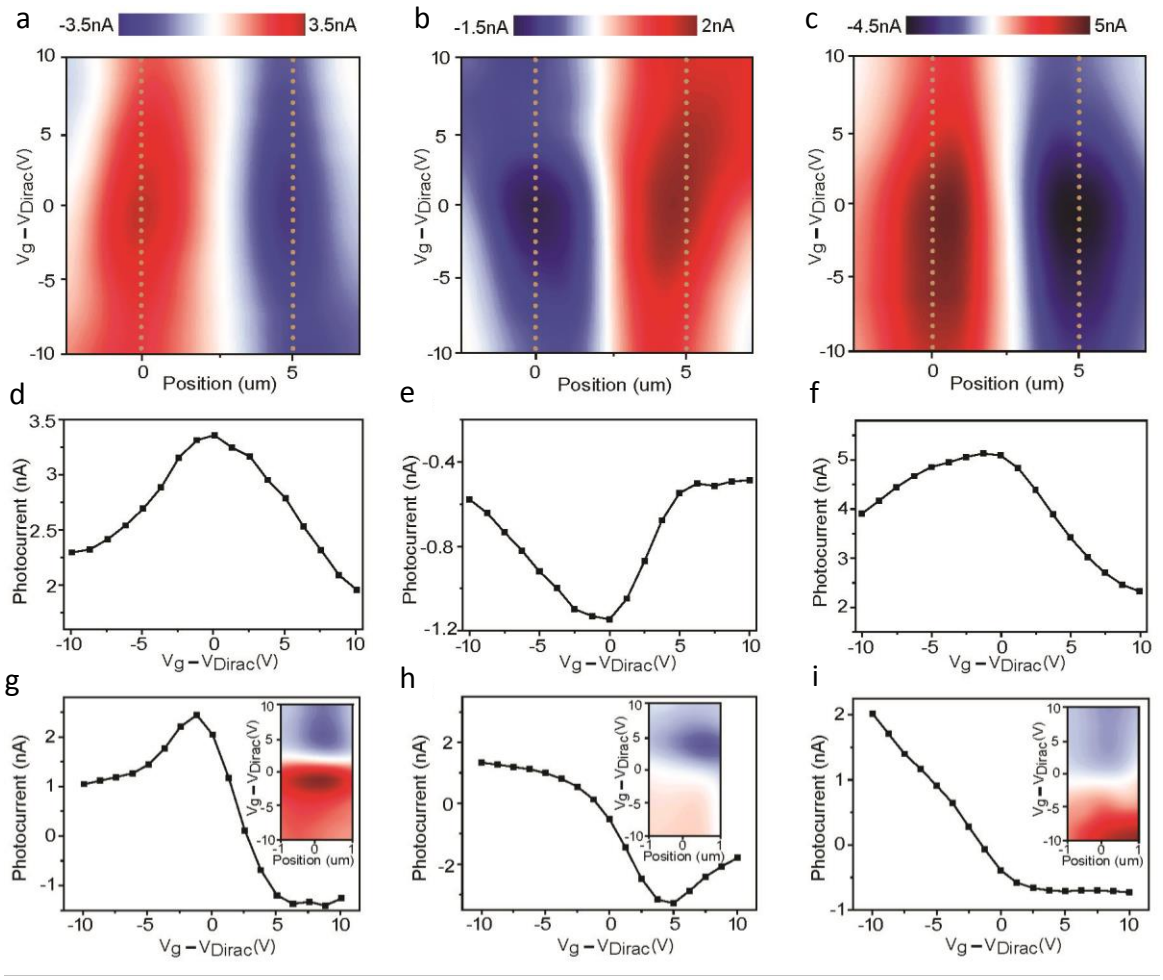

Figure 5.12 The evidence of forming photo-Dember electric field. (a-c) Gate-dependent photocurrent map under pulse laser excitation measured from (a) Device A, (b) Device B and (c) Device C respectively. The excitation pulse energy is ~19.7 pJ. The dotted lines at position = 0 and 5 μm represent the boundary of metal contact edges. (d-f) Extracted gate-dependent photocurrent from the graphene-metal interface (position= 0 μm) from maps a-c respectively. (g-i) Photoresponse of graphene-metal interface under 1.2 mW CW laser excitation. The gate-dependent photocurrent map (the inset) near the contact and the extracted gate-dependent photocurrent from the graphene-metal interface (position= 0 μm) are measured from (g) Device A, (h) Device B and (i) Device C respectively.

5.7.3 Pulse laser power versus gate-dependent photoresponse

As described in section 5.7.1, the photo-Dember field is attributed to the asymmetric electron-hole diffusion and this diffusion process is enhanced under high carrier temperature. Therefore, it is expected that pulsed laser excitation power would determine the characteristics of photoresponse. For clarity, we studied the gate-dependent photocurrent at the metal/graphene junction under different pulse laser excitation power. Fig. 5.13a-c shows three representative photocurrent maps measured at 580 μW, 930 μW, and 3.49 mW pulse laser power, respectively. Significantly, photocurrent switches sign as the pulse laser power drops (Fig. 5.13a), reminiscent of the case under CW excitation. More detailed power-dependent photocurrent curves obtained at the contact edge are shown in Fig. 5.13d with the zoom-in view shown in Fig. 5.13e. At a low power of 145 μW, photocurrent switches sign, suggesting that built-in field dominate current generation [2-3, 5]. By increasing power to 580 μW, photocurrent amplitude increases in both positive and negative regions. However, at 930 μW, photocurrent becomes entirely positive and peaks at 2 V, indicating hot carrier extraction induced by the photo-Dember field also contributes to photocurrent generation. With further increasing of the laser power, positive photocurrent peak gradually shifts to 5 V (Dirac point gate voltage), at which point hot carriers dominate transport (Figure 3e, inset). The results confirmed the formation of photo-Dember field under high pulse excitation power.

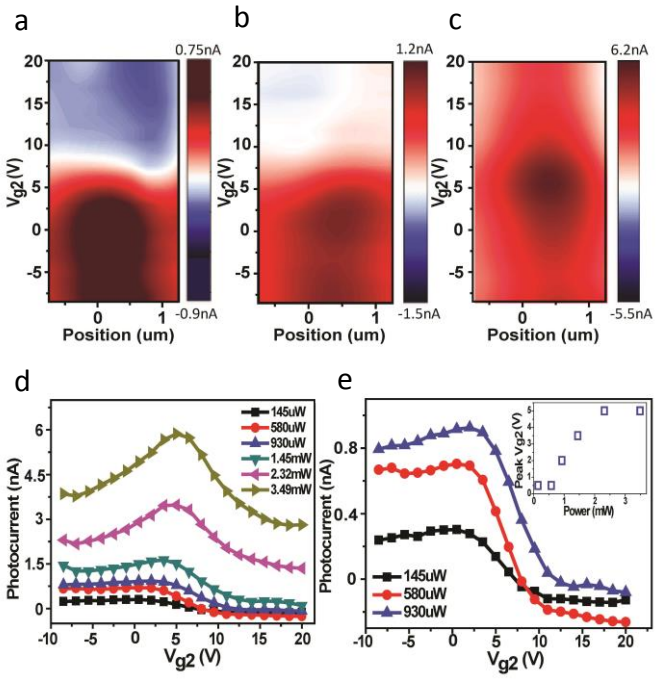

Figure 5.13 Power-dependent hot carrier photocurrent. (a-c) Gate-dependent photocurrent map under 580 μW (a), 930 μW (b), and 3.49 mW (c) pulse laser excitation. Position zero corresponds to the metal contact edge. (d) Gate-dependent photocurrent at the metal contact edge, excited by different pulse laser power. (e) Zoom-in view of the low photocurrent amplitude region. The inset shows the relation between photocurrent peak and pulse laser power.

5.7.4 Model: Dynamics of hot carrier diffusion and photo-Dember field

There are several methods for simulating the photo-Dember effect such as Monte Carlo method, drift-diffusion equation and quantum mechanics. Here, we use drift-diffusion equations to model the dynamics of carrier diffusion and photo-Dember field at the graphene/metal interface. The equations include the continuity equation of the carriers and the Poisson equation as follow:

$$\frac{\partial n_i}{\partial t} = G \pm \mu_i \frac{\partial (n_i E)}{\partial x} + D_i \frac{\partial^2 n_i}{\partial x^2} - \frac{n_i}{\tau} \quad (5.4)$$

$$\frac{\partial E}{\partial x} = \frac{q(n_h - n_e)}{\varepsilon_0 \varepsilon_r} \quad (5.5)$$

where the photoexcited charge density is n (i= e,h represent electrons and holes respectively), E is the photo-Dember field. In the model, we assume hot carrier lifetime τ= 1.5 ps, μ_e = 2000 $cm^2/_{VS}$, μ_h = 1600 $cm^2/_{VS}$, and hot carriers diffuse only in the direction perpendicular to the metal edge due to the sharp photocarrier density gradient. The relative permittivity (ε_r) is ~7.5, since graphene is immersed between two Al_2O_3 dielectric layers. Also D is related to μ via the Einstein relation (Equation 5.3).

Fig. 5.14a demonstrates the simulated ultrafast diffusion process of hot electrons and holes. Strikingly, the asymmetric distribution near the vicinity of contact builds up the intense photo-Dember field, and the dynamical evolution of field is shown in Fig. 5.14b. Furthermore, our model predicts that increasing the asymmetry of electron-hole mobility as well as device mobility will enhance the field. More importantly, the strength of field increases super-linearly with the pulse energy ($E \alpha P^{1.13}$) as shown in Fig. 5.14c. Intuitively, this nonlinear nature origins from higher photocarrier density, charge gradient, temperature (Fig. 5.14c, inset) together with higher diffusion coefficient when increasing the pulse energy.

To experimentally verify the simulation results, we measured the power-dependent photocurrent at the graphene-metal interface. As shown in Fig. 5.14d, the photocurrent also grows super-linearly in the low pulse energy region, and then transits into the sub-linear region under strong excitation due to Pauli blocking [31-32]. Interestingly, the super-linear region can be fitted well by $I_{pc} \alpha P^{1.13}$ (Fig. 5.14d, inset), in good agreement with our simulations.

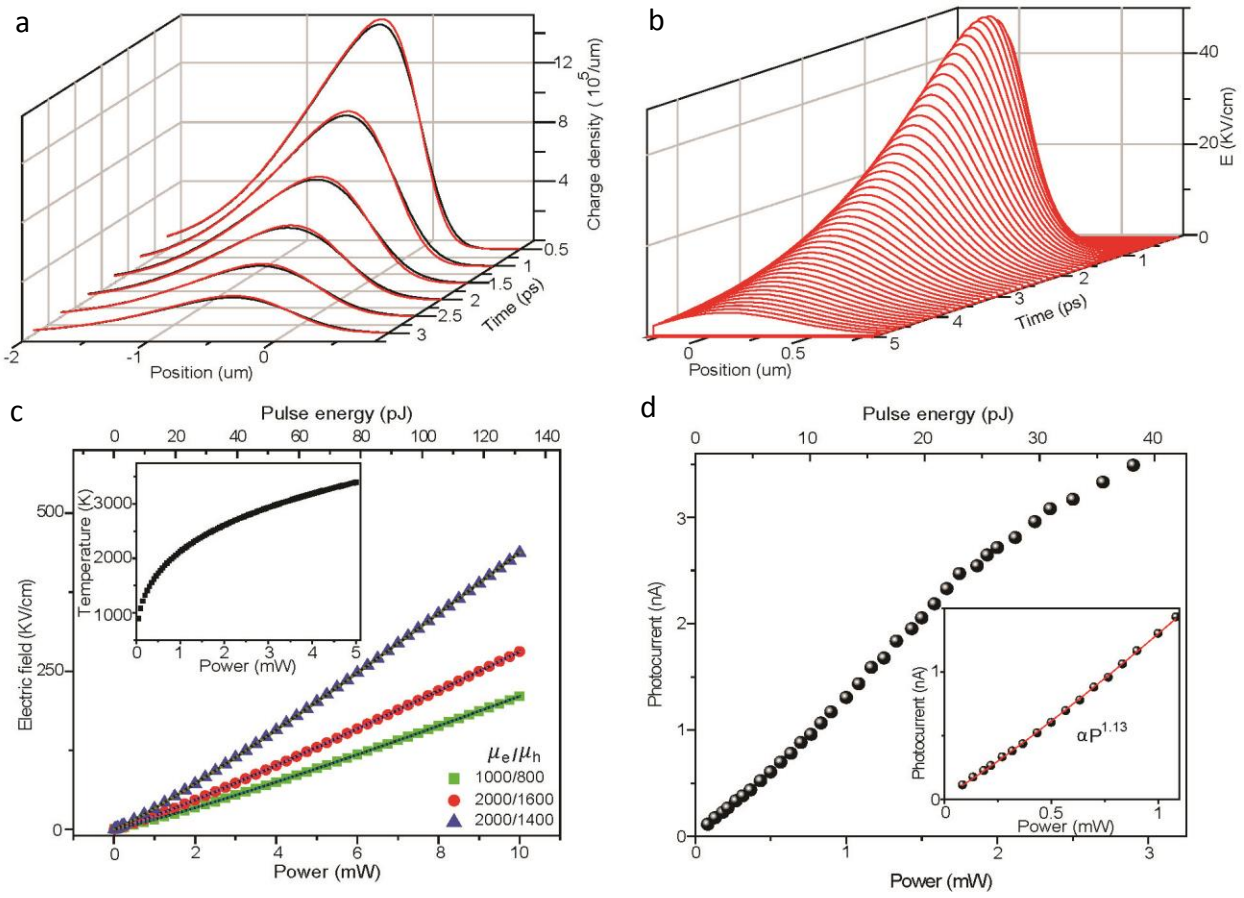

Figure 5.14 Simulation of ultrafast hot carrier dynamics. (a) Simulation of spatial and temporal evolution of hot electrons (black lines) and holes (red lines) after the pulse (26 pJ) laser excitation. Position$\geq$ 0 μm represents the metal-covered area. (b) Simulation of spatial and temporal evolution of the photo-Dember electric field after the pulse (26 pJ) laser excitation. Position$\geq$ 0 μm represents the metal-covered area. (c) Simulation of power-dependent photo-Dember electric field under different electron-hole mobility (μ_e/μ_h). The unit for mobility is cm^2/Vs. Each simulated power-dependent electric field is fitted by the power law: $E \alpha P^{1.13}$ (black lines). The simulated electric field here is at the graphene-metal interface and 1 ps after the pulse excitation. The inset shows the simulated power-dependent hot carrier temperature. (d) Experimental measurement of power-dependent photocurrent from the graphene-metal interface under pulse excitation. The inset shows zoom-in view and fitting curve in the low excitation power region.

For comparison, we also measure the power dependence of photocurrent generation from graphene-metal interface under CW laser excitation. As exhibited in Fig. 5.15, the magnitude of photocurrent shows linear dependence to the excitation power. Notably, this observation is totally different from the measurements under pulse laser excitation (Fig. 5.14d). This again suggests photocurrent driven by the photo-Dember field can occur only under intense pulse excitation.

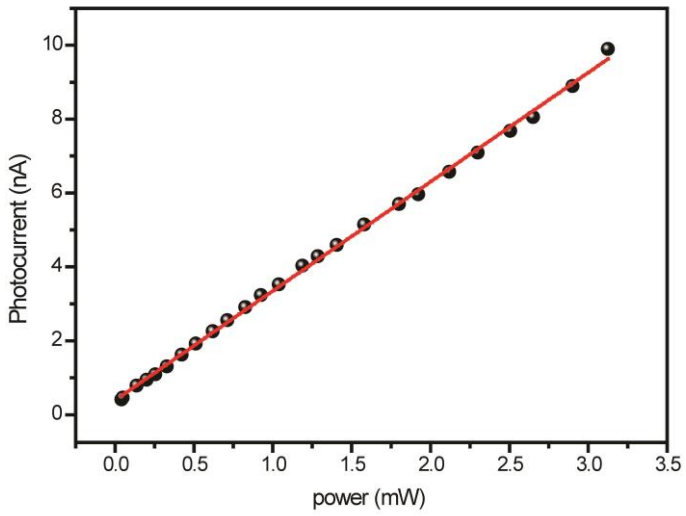

Figure 5.15 Experimental measurement of power-dependent photocurrent from the graphene-metal interface under CW excitation.

5.7.5 Measuring photocurrent at ultrafast time scales

Finally, we exploit ultrafast pump-probe technique [10] to study the effect of doping concentration on hot carrier cooling in graphene. According to the drift-diffusion model, the magnitude of photocurrent could be closely related to hot carrier cooling rate, via two parameters: diffusion coefficient and hot carrier concentration. Therefore, measuring photocurrent decay as a function of the time delay between two pulses provides a route for probing the timescale of hot

carrier relaxation.

Fig. 5.16a shows the results of pump-probe measurements under different doping level. The presence of dip at time delay = 0 results from the saturation absorption induced by pump pulse. From each pump-probe result, we extracted the response time (τ) by fitting each curve with a single exponential decay. The summary of the extracted gate-dependent response time is shown in Fig. 5.16b. Importantly, the response time is maximum at the Dirac point gate voltage, suggesting inefficient hot carrier cooling at low doping concentration. This also agrees with the recent theoretical predications [29-30].

Additionally, the result of pump-probe measurement could qualitatively explain our gate-dependent photocurrent measurements (Fig. 5.12a-f). Since slower hot carrier cooling in graphene would enhance hot carrier diffusion process and lead to longer duration of the transient photo-Dember field, it is expected that the gate-dependent photocurrent should also peak at the Dirac point gate voltage as shown in Fig. 5.12a-f. In addition to gate-dependent hot carrier cooling, it is worth noting that cold carriers might screen the photo-Dember field. In other words, increasing carrier concentration in graphene would weaken the transient photo-Dember field and reduce the amplitude of photocurrent generation.

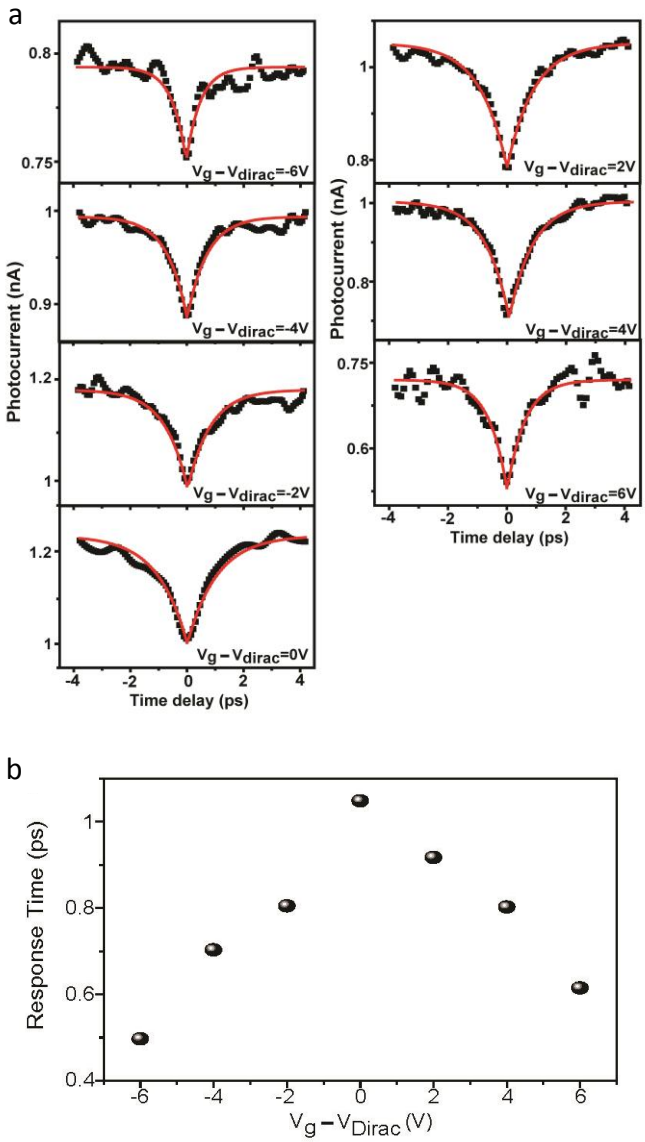

Figure 5.16 Ultrafast pump-probe measurements on the graphene/metal interface. (a) Gate-dependent ultrafast photoresponse in graphene. (b) Response time (τ) as a function of back gate voltage.

5.8 Conclusions

In summary, we systematically study the photocurrent generation at the graphene-metal contact and graphene p-n junction. The striking difference between CW and pulse laser excitation reveals that graphene photoresponse is closely related to the illumination intensity, device electrical characteristics and the doping level. These fundamental understandings are crucial for developing graphene-based hot carrier optoelectronics. Additionally, our study also reveals the formation of photo-Dember field induced by nonequilibrium hot carriers. This provides further insight of ultrafast photoresponse in graphene. For realistic applications, graphene could be integrated with nanostructures to develop graphene-based terahertz emitters [21], and to further enhance the photo-Dember field, effective engineering graphene with substrates to achieve unipolar transport [33] or high mobility [34] might be the potential route.

References:

[1] M. C. Lemme et al., Nano Lett. 11, 4134 (2011).

[2] F. N. Xia et al., Nano Lett. 9, 1039 (2009).

[3] J. Park, Y. H. Ahn, and C. Ruiz-Vargas, Nano Lett. 9, 1742 (2009).

[4] X. D. Xu et al., Nano Lett. 10, 562 (2010).

[5] E. J. H. Lee et al., Nat. Nanotechnol. 3, 486 (2008).

[6] N. M. Gabor et al., Science 334, 648 (2011).

[7] M. Breusing, C. Ropers, and T. Elsaesser, Phys. Rev. Lett. 102 , 086809 (2009).

[8] H. N. Wang et al., Appl. Phys. Lett. 96 (2010).

[9] J. M. Dawlaty et al., Appl. Phys. Lett. 92, 042116 (2008).

[10] D. Sun et al., Nat. Nanotechnol. 7, 114 (2012).

[11] A. Urich, K. Unterrainer, and T. Mueller, Nano Lett. 11, 2804 (2011).

[12] X. Li et al., Science 324, 1312 (2009).

[13] S. Lee et al., Nanoscale 4, 639 (2012).

[14] J. H. Strait et al., Nano Lett. 11, 4902 (2011).

[15] M. Cutler, and N. F. Mott, Phys. Rev. 181, 1336 (1969).

[16] J. C. W. Song et al., Nano Lett. 11, 4688 (2011).

[17] T. Mueller et al., Phys. Rev. B 79, 245430 (2009).

[18] X. C. Zhang and J. Xu, Springer (2010).

[19] K. S. Novoselov et al., Nature 490, 192 (2012).

[20] B. A. Ruzicka et al., Phys. Rev. B 82, 195414 (2010).

[21] G. Klatt et al., Opt. Express 18, 4939 (2010).

[22] C. H. Lui et al., Phys. Rev. Lett. 105, 127404 (2010).

[23] F. Bonaccorso et al., Nat. Photonics 4, 611 (2010).

[24] E. D. Palik, Academic Press (1985).

[25] S. Kim et al., Appl. Phys. Lett. 94, 062107 (2009).

[26] B. Huard et al., Phys. Rev. B 78 (2008).

[27] E. H. Hwang et al., Phys. Rev. Lett. 98 (2007).

[28] J. H. Chen et al., Nat. Phys. 4, 377 (2008).

[29] W. K. Tse et al., Phys. Rev. Lett. 99, 236802 (2007).

[30] J. C. W. Song et al., Phys. Rev. B 87, 155429 (2013).

[31] Q. L. Bao et al., Adv. Funct. Mater. 19, 3077 (2009).

[32] Z. P. Sun et al., ACS Nano 4, 803 (2010).

[33] H. Li et al., ACS Nano 5, 3198 (2011).

[34] C. R. Dean et al., Nat. Nanotechnol. 5, 722 (2010).

Chapter 6

Graphene-based Hot Carrier Photodetectors

6.1 Introduction

Today, different technologically important wavelength regimes are detected by separate photoactive semiconductors. For example, GaN, Si and InGaAs are typically exploited for sensing the ultraviolet, visible and near-infrared light respectively. Photodetection of mid-infrared regime generally relies on the low bandgap compounds, such as HgCdTe, PbS or PbSe, and thermal sensing techniques are utilized for detecting the far-infrared range. In contrast, graphene is a tantalizing optoelectronic material for developing ultra-broad spectral photodetectors due to its gapless band structure [1-3]. The difficulty with utilizing graphene in standard photodetector structures is that the lifetime of photo-generated carriers is very short; it is thus necessary to separate the electrons and holes on a sub-picoscond time scale in order to efficiently generate a photocurrent and avoid simple heating of the graphene layer. So far, nearly all graphene-based photodetectors focus on exploiting graphene-metal junction or graphene p-n junction for extracting photocurrent [4-10]. However, this sensing scheme relies on the small effective junction areas, giving rise to the limited responsivity of devices (~mA/W, Fig. 6.1a). Integrating graphene with plasmonic nanostructures [11-13] or microcavities [14-15] can enhance the light-graphene interaction and improve responsivity to tens of mA/W (Fig. 6.1b-d);

however, the enhancement can only be achieved at the designed resonant frequencies, restricting their applications for broadband photodetection. Band structure engineering in graphene has also recently been explored for photoresponsivity enhancement [16], but efficient photodetection can only be achieved below about 150 K due to the short electron life time in midgap states at elevated temperatures.

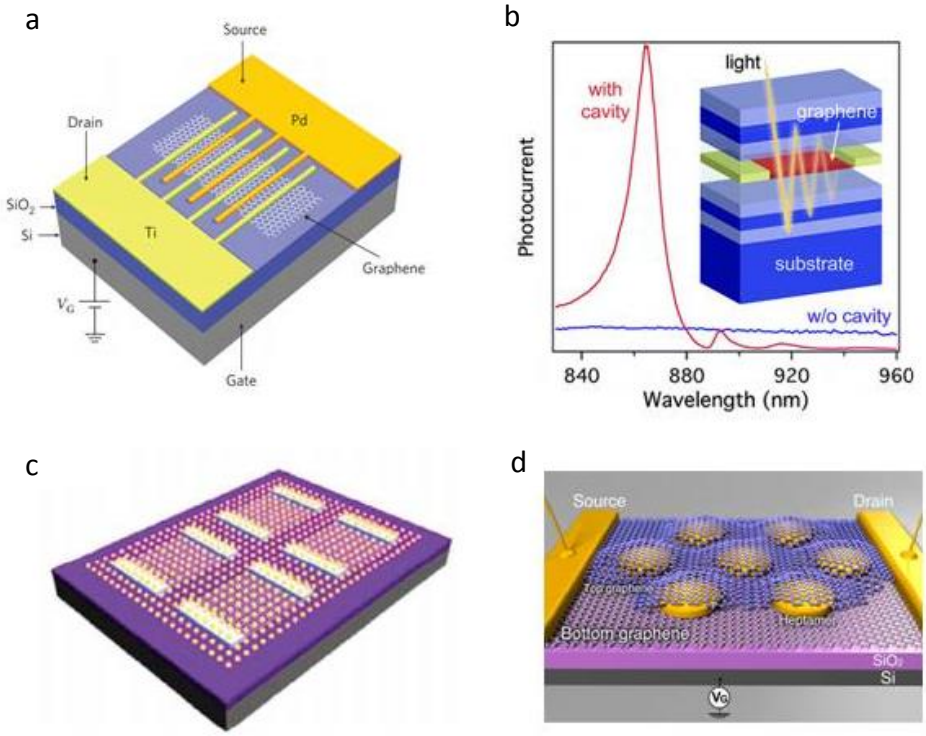

Figure 6.1 The device structures of diverse graphene-based photodetectors. (a) The interdigitated metal-graphene-metal photodetector [7]. (b) The microcavity-integrated graphene photodetector [14]. (c-d) Plasmon resonance enhanced graphene photodetectors [11-12].

An alternative approach is to exploit the photoconductive gain from graphene. Although graphene intrinsically is not an ideal photoconductor owning to its ultrafast hot carrier recombination [17-19], recent studies demonstrated the hybridized graphene-quantum dots photodetectors can achieve high photoconductive gain (Fig. 6.2) [20-21]. This sensitive detection

scheme is attributed to the strong photogating effect, induced by trapped photocarriers in quantum dots. Despite its excellent responsivity, light absorption relies on quantum dots instead of graphene restricting the spectral range of photodetection.

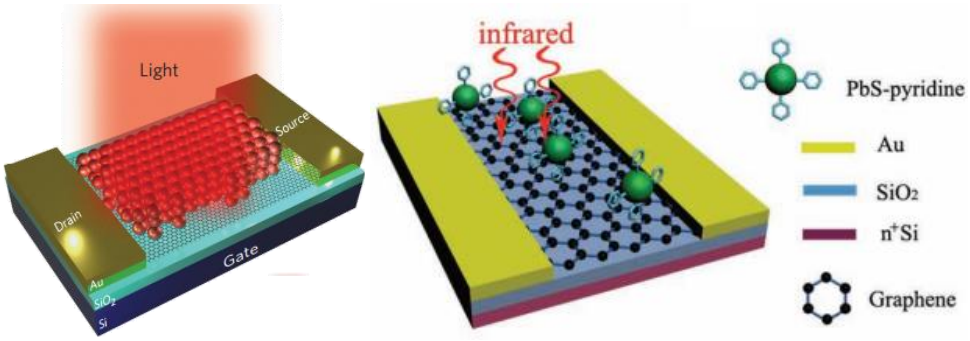

Figure 6.2 Graphene-quantum dots hybrid photodetectors [20-21].

In this chapter, we present a graphene-based hot carrier photodetector, composed of two spatially closed graphene layers sandwiched in a thin tunneling barrier. The operation principle of this light sensitive photodetector relies on the selective quantum tunneling of photoexcited hot electrons or holes between two graphene layers, from which the selected hot carriers transport to the nearby graphene layer resulting in a strong photogating effect. Further scanning photocurrent together with photon energy-dependent measurements confirm hot carrier can be extracted vertically through tunneling, which distinguishes from the recent investigations on graphene hot carrier effects in the lateral direction. By engineering the dielectric barrier, the proposed device structure could even detect light into the mid-infrared domains, with the responsivity comparable with the state-of-the-art infrared photodetectors operating at low temperature [22].

6.2 Device structure and fabrication

Fig. 6.3 schematically shows the device structure of our graphene photodetector. The proposed device composed of two graphene layers encapsulates a thin Ta_2O_5 dielectric layer. To fabricate this sandwich structure, we first transferred the graphene film onto a 285-nm-thick SiO2, thermally grown on a degenerate p-doped Si substrate [23-24]. The used graphene films here were grown by CVD method on copper foil and single-layer nature of the graphene was also identified by Raman spectroscopy. The following photolithography, graphene plasma etching, and metal lift-off processes were used to fabricate the bottom graphene transistor. This bottom graphene transistor was then entirely covered by a thin dielectric layer, deposited by RF sputtering to serve as the tunneling barrier. In this work, we choose Ta_2O_5 and Si as dielectric layer for performing photodetection. Finally, the top graphene layer was transfer onto this dielectric thin film, and the subsequent photolithography, graphene etching, and metal lift-off processes were used again to fabricate the top graphene transistor.

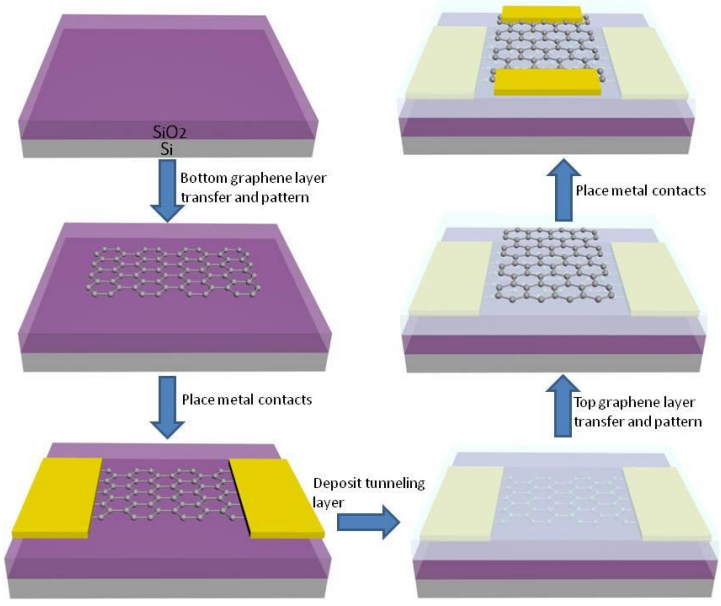

Figure 6.3 Fabrication procedures of the graphene double-layer heterostructures.

6.3 Electrical characteristics

In this section, we describe the electrical characteristics of graphene double-layer heterostructures (graphene/Ta_2O_5/graphene) without light illumination. Fig. 6.4a shows the gate transfer curves of the bottom and top graphene layer for a typical device. By applying voltage on the silicon backgate *(V_{gb}),* bottom layer graphene exhibits ambipolar gate response (red), while top layer graphene shows weak gate dependence (black) due to partial screening of electric field by the bottom layer. Importantly, these two closely-spaced graphene layers are electrically isolated with the interlayer resistance >4 GΩ. Dark tunneling current can be measured by applying a bias voltage across the graphene double layer, as shown in Fig. 6.4b. The *I-V* characteristics show larger magnitude of tunneling current in the negative bias region than the positive bias region, indicating that top graphene layer is degenerate p doped relative to bottom graphene layer under equilibrium.

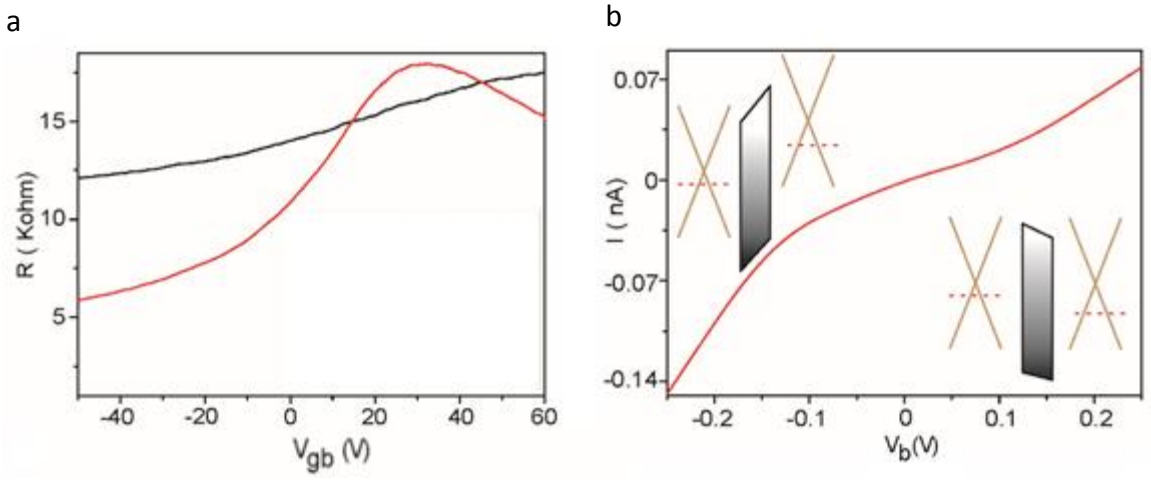

Figure 6.4 Electrical characteristics of the graphene double-layer heterostructures. (a) Resistance as a function of back gate voltages for the bottom layer graphene transistor (red) and top layer graphene transistor (black). (b) Electrical tunneling current as a function of bias voltage applied across two graphene layers. Bottom layer is grounded with bias voltage applied to the top layer. Inset, schematic band diagrams under forward and reverse bias.

6.3.1 Measuring the intrinsic doping level of top and bottom graphene layers

To evidently confirm that top graphene is degenerate p doped relative to bottom graphene layer, one of the easiest approaches is to measure the ambipolar I-V_g transfer curves of two graphene layers and then calculate their intrinsic doping concentration based on the equation:

$$E_F = \hbar v_F \sqrt{\pi C \frac{(V_g - V_g^{CNP})}{e}} \quad (6.1)$$

where $\hbar v_F$ = 5.52 eVÅ and C is the gate capacitance for V_g.

For the bottom graphene layer, its ambipolar I-V_g transfer curve can be readily derived by sweeping the silicon backgate voltage (V_{gb}) (Fig. 6.5, black curve). For the top graphene layer, we can operate the bottom layer graphene as a gate (V_{gm}), and measure its gate effect on the top layer graphene (Fig. 6.5b, red curve).

However, to apply equation 6.1 and get E_F, it is necessary to know the capacitance of SiO_2 and Ta_2O_5 dielectric layers. In this regard, we configure our graphene double layer heterostructure device as a dual gate field-effect transistor (Fig. 6.6a). Here, the Si substrate is used as the backgate and top graphene layer is served as the top-gate. Sweeping both top-gate voltage (V_{gt}) and the backgate voltage (V_{gb}) can modulate the channel conductance of bottom layer graphene. A 2D color plot of bottom layer graphene resistance versus both V_{gt} and V_{gb} are shown in Fig. 6.6b. It is apparent that ambipolar transfer characteristics can be observed with both gate voltage sweeps, with the charge neutrality point ($V_{gb}^{CNP}, V_{gt}^{CNP}$) identified as the local peak in resistance. More importantly, the slope of $\frac{V_{gb}^{CNP}}{V_{gt}^{CNP}} \sim 74$ in the 2D plot gives a direct measurement of the ratio between top-gate capacitance and backgate capacitance. The backgate dielectric is thermal oxide (ε_{SiO_2} = 3.9, Thickness of SiO_2 = 285 nm) with a backgate capacitance

of 1.2×10^{-8} F/cm^2. Hence, the gate capacitance of the Ta_2O_5 dielectric layer is calculated to be 8.9×10^{-7} F/cm^2.

With the above information, we then estimate the Fermi energies of top and bottom layer graphene are 4.756 eV and 4.655 eV respectively. Importantly, this result agrees with the *I-V* measurement as shown in Fig. 6.4b, indicating top graphene is degenerate p doped relative to bottom graphene layer under equilibrium.

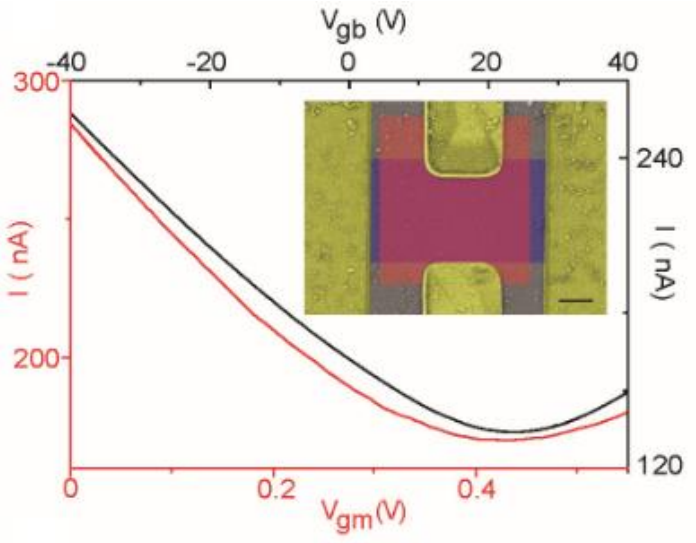

Figure 6.5 Transfer curve for bottom layer graphene using Si backgate (V_{gb}) is shown in black. Transfer curve for top layer graphene using bottom layer graphene as gate (V_{gm}) is shown in red. The inset shows the false-color SEM image of the device. The purple and red areas represent the bottom and top graphene layers, respectively. Scale bar is 1 μm.

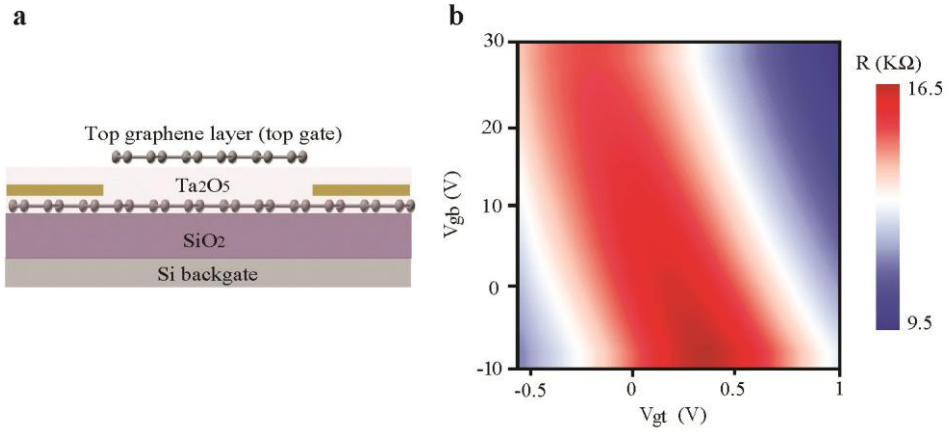

Figure 6.6 Characterization of the gate capacitance of Ta_2O_5 layer. (a) Device structure of a graphene heterostructure photodetector. Here we operate the device as a dual-gate field effect transistor, with silicon substrate as the backgate (V_{gb}), and top graphene layer as the top gate (V_{gt}). (b) Two dimensional plot of the resistance of the bottom graphene layer as a function of V_{gb} and V_{gt}.

6.4 Principles of photodetection

The working principle of the graphene double-layer heterostructure photodetector can be understood through the device schematic and band diagram (Fig. 6.7a and 6.7b). Graphene here is not only the charge transport channel but also used as the light absorber, while Ta_2O_5 serves as the tunneling barriers. Since the top graphene layer is degenerate p doped relative to bottom graphene layer as discussed in section 6.3, the energy band of the tunneling barrier is thereby tilted in order to equilibrate Fermi level (Fig. 6.7b). Under optical excitation, both graphene layers generate electron-hole pairs. However, this asymmetric tunneling barrier selectively facilitates hot electrons tunnel from top to bottom graphene layer with the oppositely positive charges accumulated in the top graphene layer. As a result, these trapped positive carriers will lead to a photogating effect, which changes the conductance of bottom graphene transistor

through the capacitive coupling. In particular, graphene channel is very sensitive to external electrostatic perturbation, and the usage of thin oxide film here not only favors hot carrier tunneling, but also induces high interlayer dielectric capacitance. All of these factors contribute to the strong photogating effect and lead to efficient photodetection.

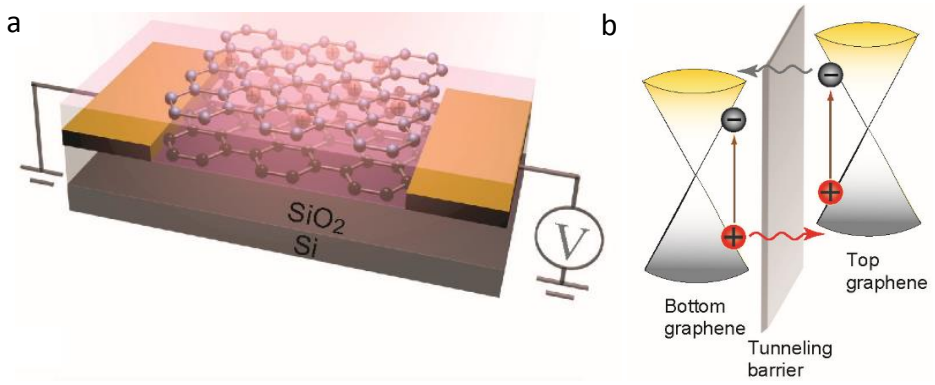

Figure 6.7 The working principle of our graphene photodetector. (a) Schematic illustration of the device structure. (b) Schematic illustration of band diagram and photo-excited hot carrier transport under light illumination.

6.5 Interlayer hot carrier tunneling

To evidently confirm that hot carrier could tunnel between graphene layers, we exploit the scanning photocurrent spectroscopy to investigate photoexcited hot carrier transport [4-5, 8]. Fig 6.8a shows the schematic of our experimental setup and Fig. 6.8b shows scanning photocurrent image of the device under 900 nm light excitation. The measurement was conducted under the short-circuit condition with the bottom graphene layer connected to the ground. The result clearly shows photocurrent is generated within the overlapped region of two graphene layers, suggesting photocurrent generation arises from hot carrier tunneling between graphene interlayers. Additionally, the polarity of photocurrent is negative. This direction preference indicates the asymmetry of tunneling barrier facilitates hot electrons transport from the top to bottom graphene layer (Fig. 6.7b).

In addition, we excite the same device with the shorter irradiation wavelength at 800 nm, and the result shows photon-induced photocurrent is nearly six times larger, compared with 900 nm light at the same laser intensity (Fig. 6.8c). The dependence of photocurrent on photon energy provides further support for hot carrier tunneling, since carriers excited to higher energies should have a higher injection rate through the barrier [25].

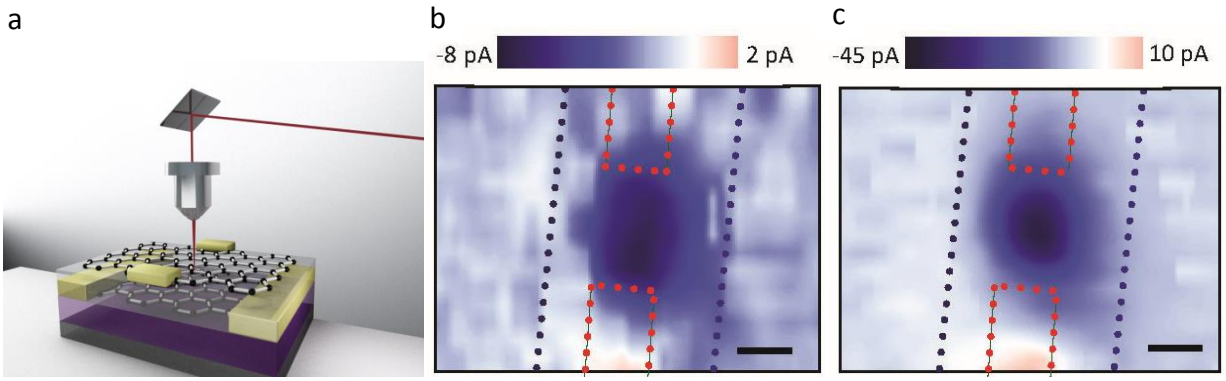

Figure 6.8 Photo-excited hot carrier tunneling in graphene double-layer heterostructures. (a) Schematic drawing of our experimental setup. (b-c) Scanning photocurrent images of the graphene double-layer heterostructures at excitation wavelength of (b) 900 nm and (c) 800 nm. Vertical tunneling current across the heterostructures was measured under the short-circuit condition with the bottom layer graphene grounded. The laser spot sizes in these scanning measurements are ~ 1.5 μm, and the laser power is 1 mW. Scale bars represent 2 μm.

For comparison, we also utilize scanning photocurrent spectroscopy to measure the short-circuit photocurrent generation from the top and bottom graphene transistor respectively. In this measurement, the laser excitation wavelength is at 900 nm and excitation power is 600 μW. The measured scanning photocurrent images are shown in Fig. 6.9. From these two figures, we can see two photocurrent peaks near the metal/graphene contact edges with opposite polarity, suggesting photocurrent generation is due to the built-in electric field at the metal/graphene junction. These spatial features are drastically different from the photocurrent images in Fig. 6.8, where hot carrier tunneling current is generated at the overlapped region of two graphene layers.

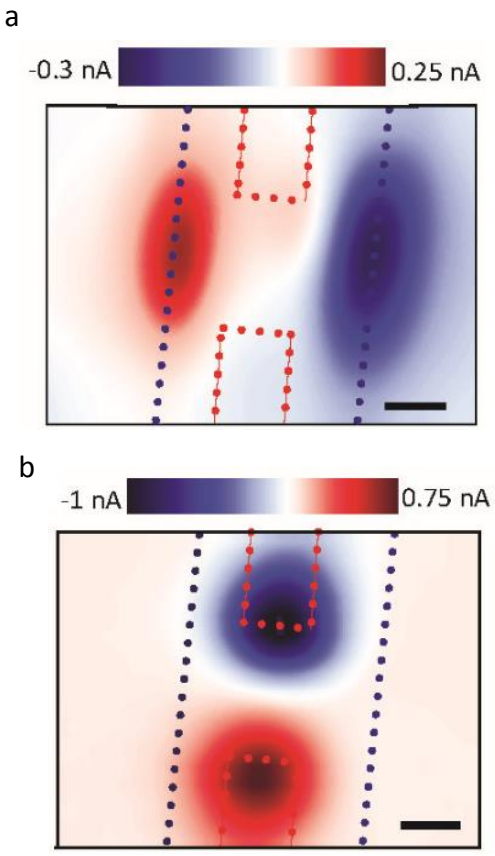

Figure 6.9 Scanning photocurrent measurements of (a) top and (b) bottom layer graphene transistors respectively. In both panels, the blue dotted lines indicate the metal/graphene contact edges of bottom graphene transistor, and the red dotted lines indicate the metal/graphene contact edges of top graphene transistor. Scale bars represent 2 μm.

6.6 Photodetection in the visible to near-infrared regimes

After characterizing the working principles of this heterostructures, we then describe its photoresponse. Fig. 6.10a shows the effect of light illumination on electrical gate response of the bottom graphene transistor over a four orders of magnitude range of optical powers (λ= 532 nm). Interesting, by increasing the laser power, the Dirac point gate voltage dramatically shift toward the lower value of V_{gb} (Fig. 6.10c, inset). This observation indicates efficient tunneling of high

energy hot carrier, which induces positive photocarriers trapped in the top graphene layer, giving rise to n doping of the bottom graphene channel through capacitive coupling. This physical picture is also in good agreement with our scanning photocurrent and electrical transport measurements.

By exploiting the change of conductivity in bottom graphene transistor, we can detect the photocurrent (I_{light}- I_{dark}) from the device. As plotted in Fig. 6.10b, the magnitude of photocurrent increases with excitation power, and more importantly, this photosignal can be gate-modulated. To gain further insight into the characteristics of this photodetector, we extract the power dependence of photocurrent (Fig. 6.10c), and calculate the responsivity of the device (Fig. 6.10d). Under low excitation power, the device shows responsivity higher than 1000 A/W, suggesting the built-in amplification mechanism of this device can significantly convert photon energy into electrical signal. To further enhance the photosignal, higher source-drain voltage could be applied to the bottom graphene transistor, and our device shows photocurrent could increase linearly with the bias voltage (Fig. 6.10d, inset).

We also measure the photoresponse of the same device under longer wavelength light illumination (800 nm and 900 nm) as demonstrated in Fig. 6.11. From here, we can see the shift of Dirac point and the amplitude of photosignal drop a lot compared with 532 nm illumination. More importantly, the measured responsivity under 800 nm light excitation is nearly six times higher than 900 nm excitation as shown in Fig. 6.11e. This ratio consists with the difference of scanning photocurrent measurements between 800 nm and 900 nm light excitation (Fig. 6.8), implying the responsivity of photodetector is closely related to hot carrier injection rate.

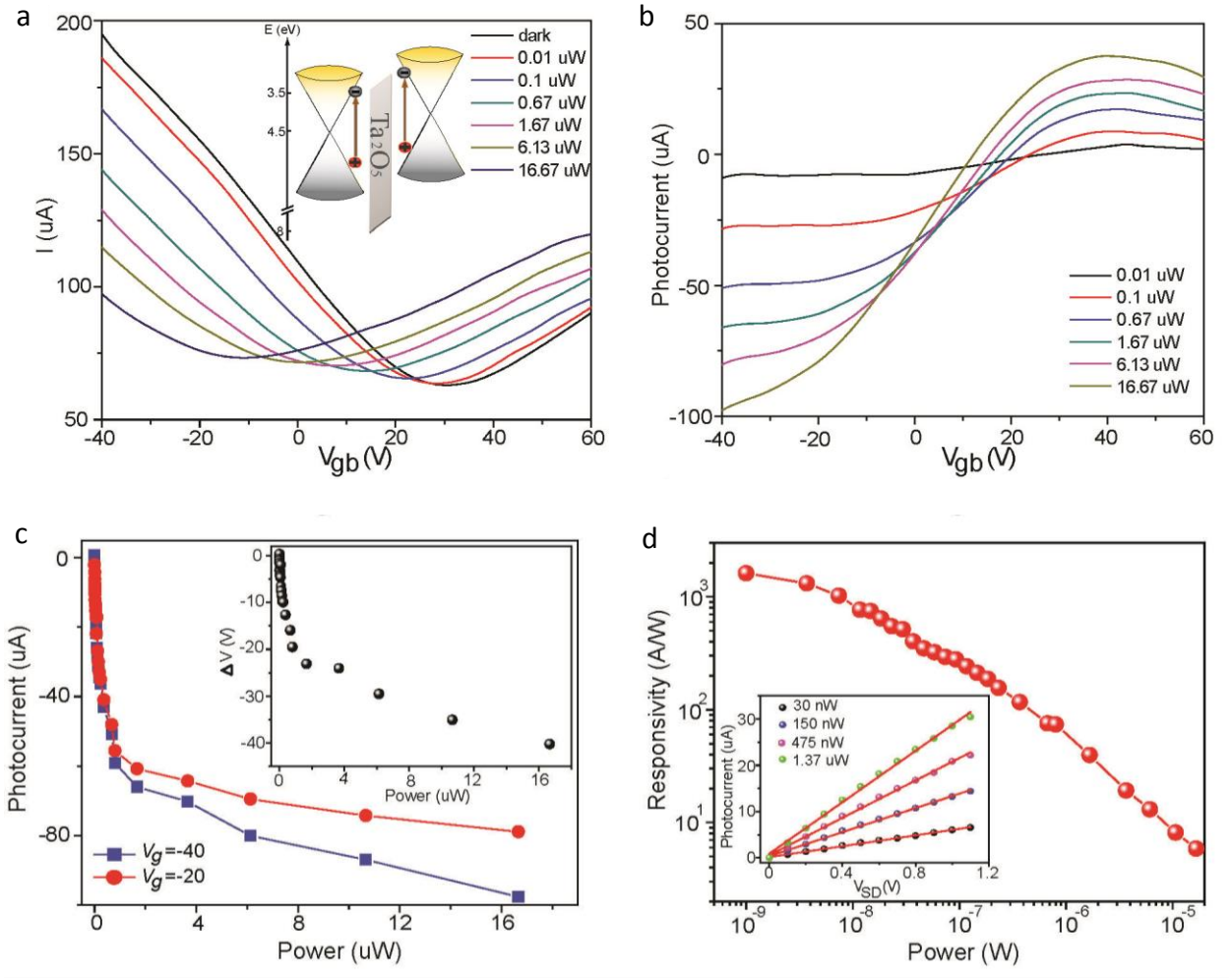

Figure 6.10 Photoresponse of the graphene double-layer heterostructures in visible region. (a) *I*-V_{gb} characteristics of the measured graphene photodetector under different laser power. The potential of the top graphene layer was floated, while the current of bottom graphene transistor was measured under 1 V source-drain bias voltage. The laser wavelength is 532 nm with a spot size of 10 μm, covering the entire graphene photodetector. The inset shows the energy band diagram of the graphene/Ta_2O_5/graphene heterostructures. (b) Gate dependence of photocurrent under different laser power. (c) Power dependence of photocurrent at different backgate voltages. The inset shows the shift of Dirac point gate voltages as a function of the illumination power. (d) The measured photoresponsivity versus illumination power. The inset shows the magnitude of photocurrent increases linearly with the source-drain bias voltage of bottom layer graphene transistor.

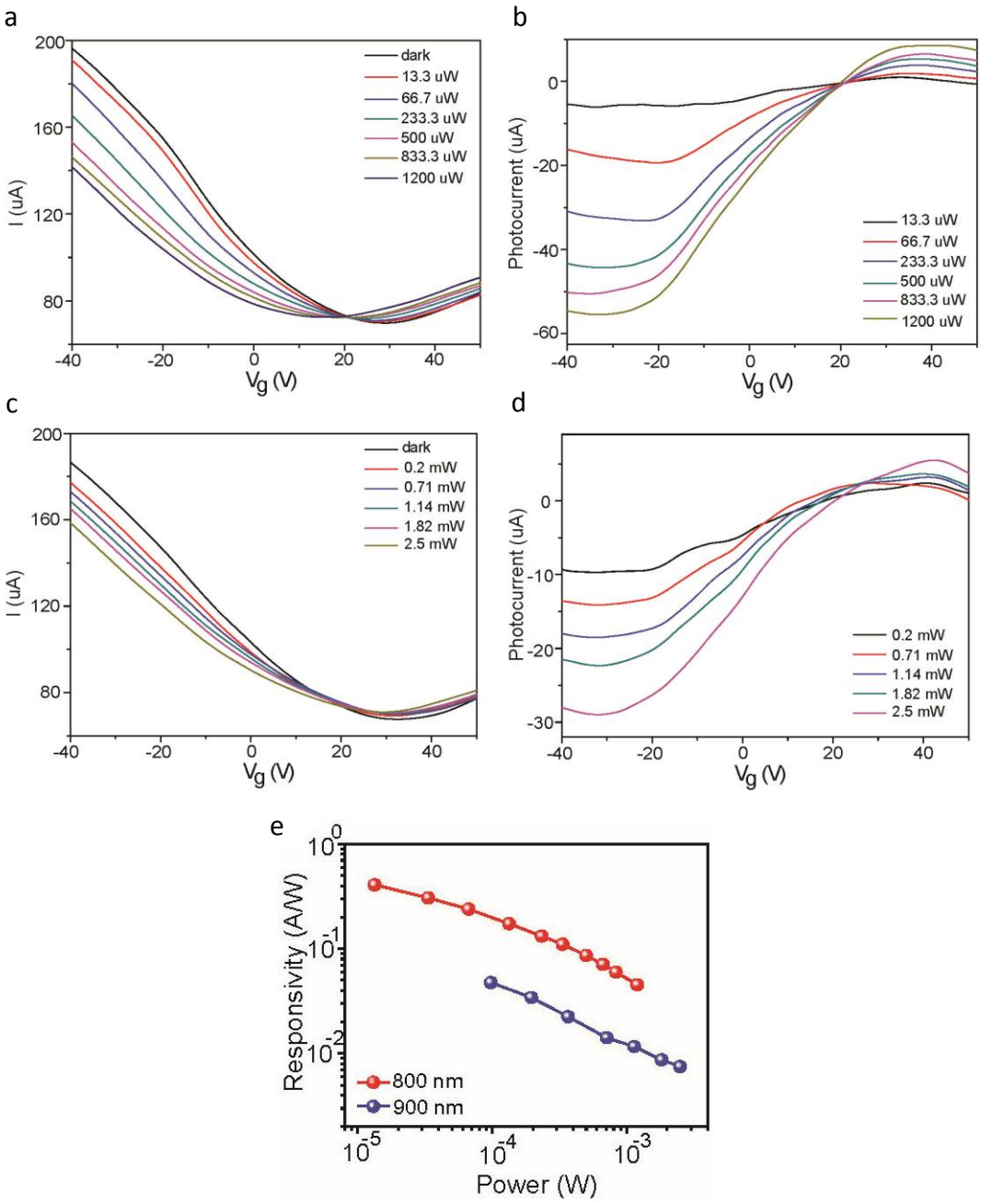

Figure 6.11 Near-infrared photoresponse of the graphene/Ta_2O_5/graphene heterostructure photodetector. (a) I-V_g characteristics of the measured graphene photodetector under different illumination power with the excitation wavelength at 800 nm. V_{SD} = 1 V. (b) Extracted gate dependence of photocurrent (I_{light}- I_{dark}) from results in (a). (c) I-V_g characteristics of the measured graphene photodetector under different illumination power with the excitation wavelength at 900 nm. V_{SD} = 1 V. (d) Extracted gate dependence of photocurrent (I_{light}- I_{dark})

from results in (c). (e) Responsivity comparison of graphene photodetector at wavelengths of 800 nm (red) versus 900 nm (blue).

As control experiments, we also measured the photoresponse of a graphene transistor covered by 5-nm-thick Ta_2O_5 but without the top graphene layer. As shown in Fig. 6.12, the transfer curve shifts are much smaller and, most importantly, in the opposite direction when compared with the photoresponse of graphene double-layer photodetector. This striking difference reveals that having top graphene layer is important for both light absorption and inducing photo-gating effect.

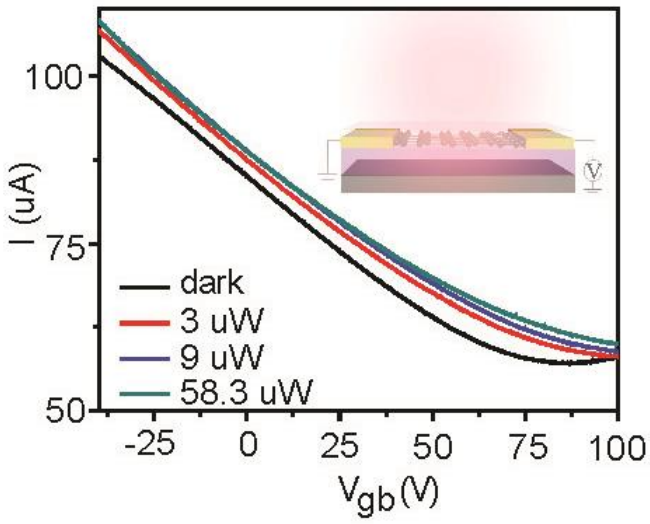

Figure 6.12 Photoresponse of a control device with identical design except the top graphene layer. The inset is schematic of the control device.

6.7 Photodetection in the near to mid-infrared regimes

To further expand the range of photodetection into the infrared regime with high responsivity, we fabricated similar device structures, but incorporating intrinsic silicon as the

tunnel barrier, in place of the wide bandgap Ta_2O_5 layer; the Si conduction band is ~ 0.5 eV above the Fermi level of intrinsic graphene (Fig. 6.13d, inset) [26-27], enabling tunneling of lower energy electrons. The infrared photoresponse of the graphene/Si/graphene heterostructures are similar to our previous measurements, displaying large shifts of the transfer curve and Dirac point voltage toward negative V_{gb} with increasing illumination power (Fig. 6.13). Fig. 6.14a-c shows the extracted gate dependence of photocurrent under 1.3 μm, 2.1 μm and 3.2 μm wavelength light illumination, respectively. Strong photo-gating effect and gate modulation of photo-signal are again clearly observed in both near-infrared and mid-infrared regimes. Power-dependent photocurrent curves are extracted from Fig. 6.14a-c and plotted in Fig. 6.14d-f, respectively. Significantly, the near-infrared responsivity of the device reaches 4 A/W at λ = 1.3 μm (Fig. 6.14d) and 1.9 A/W at λ = 2.1 μm (Fig. 6.14e) at room temperature. These values are more than three orders of magnitude higher than the responsivity of graphene/Ta_2O_5/graphene heterostructures at the near-infrared wavelengths. Furthermore, our prototype graphene photodetector exhibits room temperature mid-infrared responsivity of 1.1 A/W at λ = 3.2 μm (Fig. 6.14f), rivaling state-of-art mid-infrared detectors without the need for cryogenic cooling.

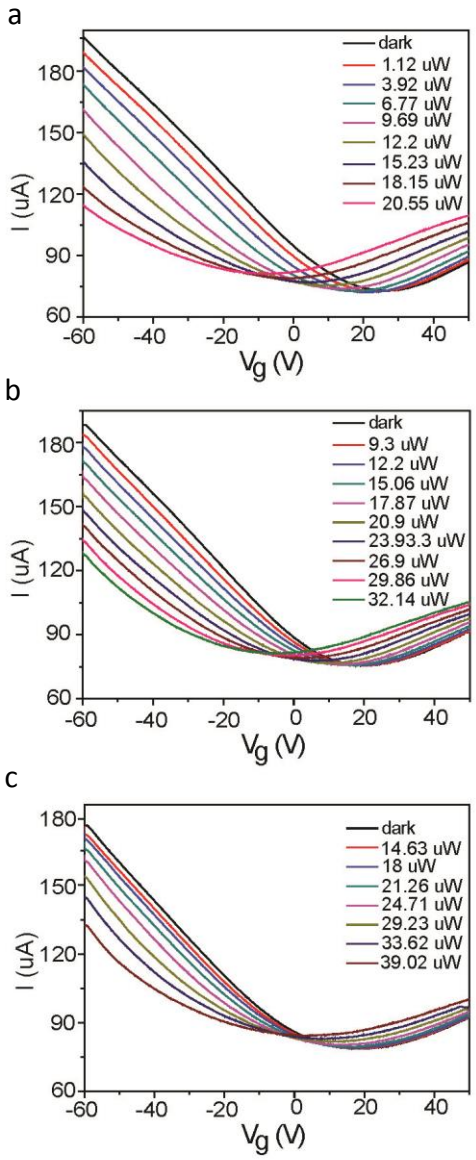

Figure 6.13 Near to mid-infrared photoresponse of the graphene/Si/graphene heterostructure photodetector. I-V_{gb} characteristics of graphene photodetector under different illumination power with the excitation wavelength at (a) 1.3 μm, (b) 2.1 μm, and (c) 3.2 μm, respectively. V_{SD} = 1.5 V.

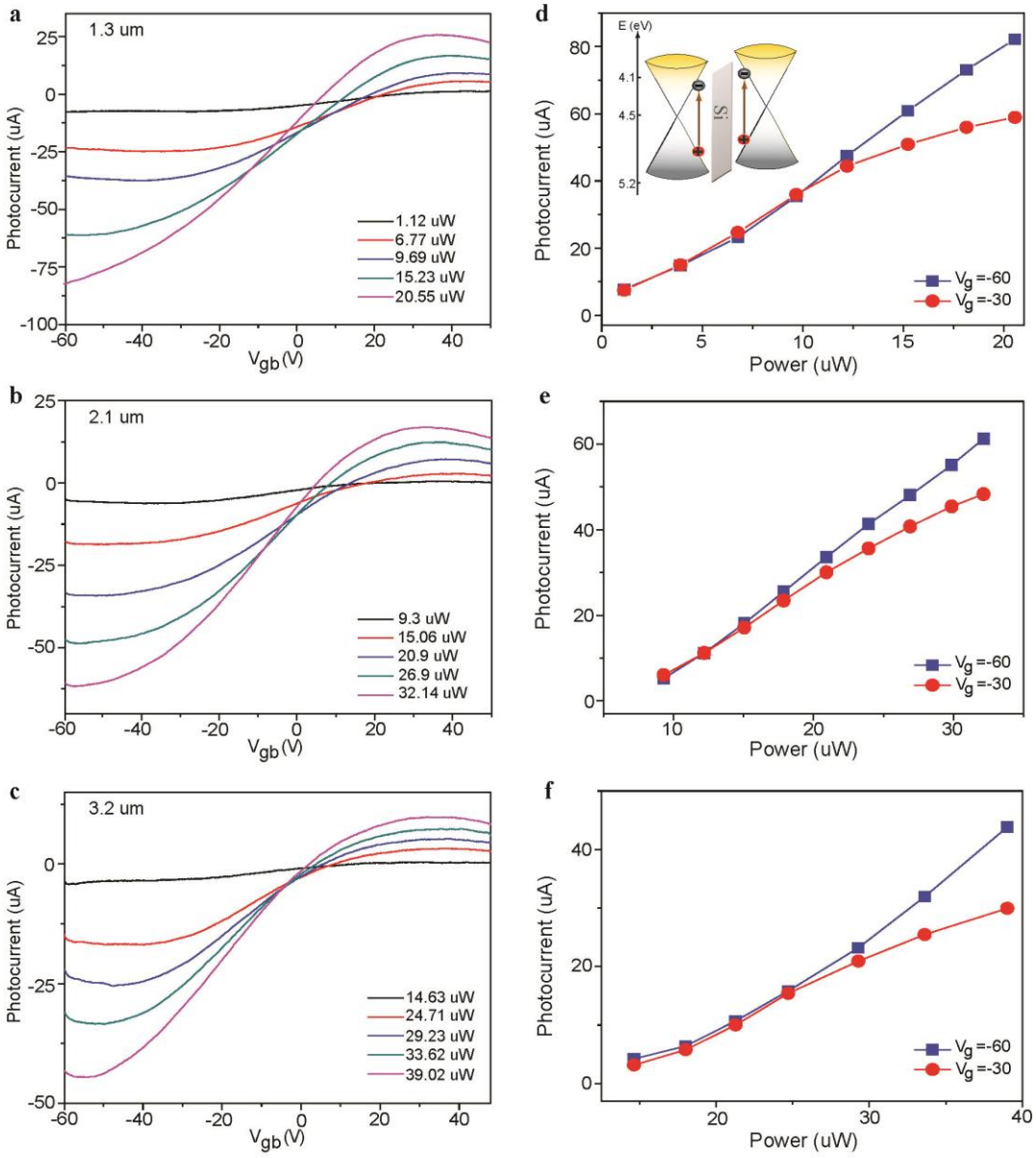

Figure 6.14 Near to mid-infrared photoresponse of the graphene/silicon/graphene heterostructure photodetector. a-c, Gate dependence of photocurrent under different illumination power with the excitation wavelength at (a) 1.3 μm, (b) 2.1 μm, and (c) 3.2 μm, respectively. These measurements were conducted by applying 1.5 V bias voltage to the bottom graphene transistor, and the laser spots were focused to ~ 20 μm, covering the entire graphene photodetector. d-f, Photocurrent versus illumination power under excitation wavelength of (d) 1.3 μm, (e) 2.1 μm, and (f) 3.2 μm, respectively. Inset in (d) shows the band diagram of graphene/silicon/graphene heterostructures.

6.8 Device operation speed

In addition to responsivity and wide detection spectrum, high speed photodetection is also required for some technological applications. For example, optical communication systems require photodetectors with speed higher than GHz. For imaging applications, the detectors are usually operated at a frame rate of ~60 Hz. For our proposed photodetectors, the intrinsic operation speed would be limited by the recombination time of the trapped carriers on top graphene layer. In this regard, we introduce the reset protocol to enhance the operation speed of our photodetectors. Specifically, we synchronize the laser on/off with the reset gate voltage pulses. Each gate voltage pulse would change the bottom graphene layer from p type to n type, which leads to a faster discharge of trapped carriers on the top graphene layer. Our reset measurement is shown in Fig. 6.15. In this measurement, the time-dependent photo-induced current under on/off light modulation was performed at room temperature with 1 V bias voltage to the bottom graphene layer. As a 10 ms gate voltage pulse is applied to silicon back-gate, we can see that the device reaches back to equilibrium ~100 ms, showing the faster switching speed and we expect this speed could be significantly improved by using the better dielectric layer.

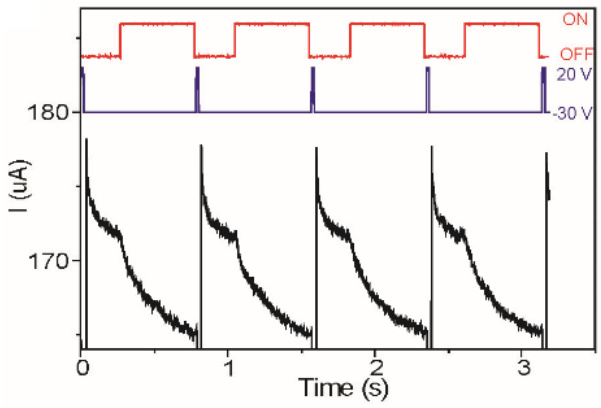

Figure 6.15 Temporal photoresponse of the graphene/Ta_2O_5/graphene photodetector. The illumination power is 0.3 μW and laser wavelength is 532 nm. The laser on-off is controlled by a mechanical shutter synchronized with the reset back-gate voltage pulses.

6.9 Noise equivalent power

Noise-equivalent-power (NEP) is an important figure of merit for photodetectors, and it is defined as the optical power that yields a unity signal-to-noise ratio for a given bandwidth. To obtain NEP, we first analyze the noise in the dark current waveform. As shown in Fig. 6.16a, the dark current waveform was acquired by a current preamplifier and a data acquisition card with a sampling rate of 10 kHz. The source-drain bias voltage applied to the bottom graphene layer was 1 V in this measurement. The noise spectral density is given by

$$S(f) = \lim_{T\to\infty} \frac{1}{\sqrt{T}} \sqrt{\left\langle \left| \int_{-T/2}^{T/2} I(t) e^{-i2\pi ft} dt \right|^2 \right\rangle} \quad (6.2)$$

where $\langle\ \rangle$ denotes the expectation value, and $I(t)$ is the current waveform. The definition can be generalized to discrete finite sampling of the current $I(t_n)$:

$$S(f_n) = \frac{1}{\sqrt{F_s N}} \sqrt{\left\langle \left| \boldsymbol{I}(f_n) \right|^2 \right\rangle} \quad (6.3)$$

where $\boldsymbol{I}(f_n)$ denotes the discrete transform of $I(t_n)$; F_s is the sampling sampling rate; N is the number of data points. Notice that the Fourier transform used here is defined so that $S(f_n)$ is non-zero only at positive frequencies. The unit of $S(f_n)$ is $A/Hz^{1/2}$. Fig. 6.16b shows the noise spectral density of the dark current calculated by Eq. 6.3.

In addition, we also directly measured the noise spectral density of the dark current by using a FFT spectrum analyzer (Stanford Research Systems SR760). The measured noise spectral density is shown in Fig. 6.16c. The results obtained by these two approaches are consistent with each other. NEP can be calculated by dividing the noise spectral density by the responsivity. With visible excitation, the responsivity of graphene photodetector can achieve ~1000 A/W, which corresponds to a NEP of ~ 10^{-11} $W/Hz^{1/2}$ at a modulation frequency of 1 Hz.

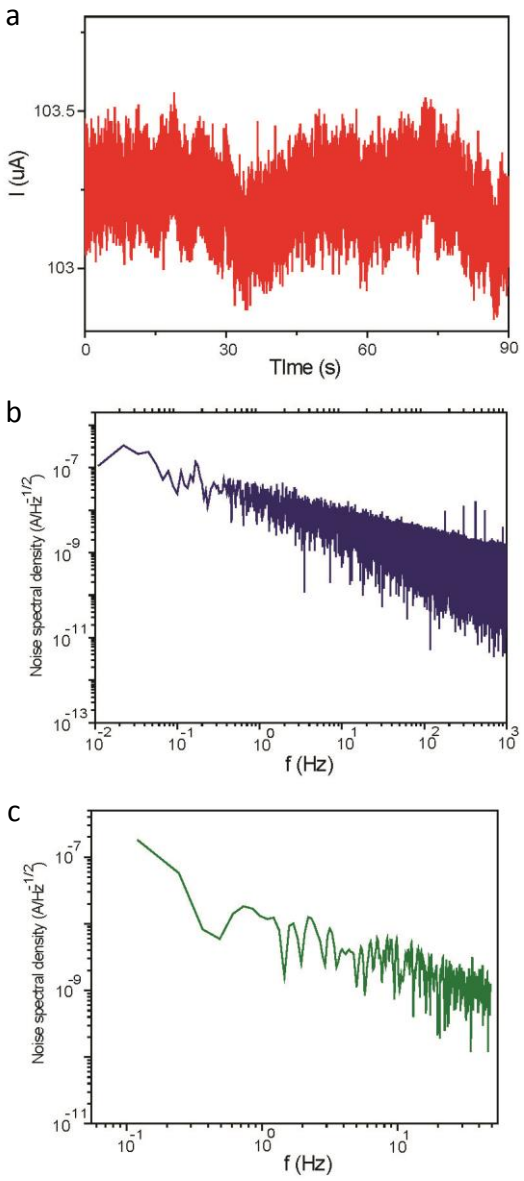

Figure 6.16 Analysis of noise spectral density of the heterostructure graphene photodetector. (a) The dark current waveform of the graphene photodetector with source-drain voltage V_{sd} = 1 V. (b) Analysis of noise spectral density of the graphene photodetector based on the dark current waveform measured in (a). (c) Noise spectral density of the graphene photodetector measured directly by using a commercial FFT spectrum analyzer.

6.10 Conclusions

In summary, we presented photodetectors based on graphene double layer heterostructures. By exploiting the strong photogating effect induced by hot carrier tunneling, we have seen that graphene photodetectors with high photoresponsivity could be realized. Furthermore, since we applied graphene as the photoactive material, our devices can simultaneously exhibit broad spectrum photodetection. To further enhance the device performance, the bottom graphene channel could be replaced with other thin film semiconductors to reduce the dark current. Furthermore, hot carrier tunneling between interlayers could be enhanced by utilizing atomically thin 2D semiconductors, such as MoS_2 or WS_2 as the encapsulated tunneling barrier [28-29].

References:

[1] R. R. Nair et al., Science 320, 1308 (2008).

[2] K. F. Mak et al., Solid State Commun. 152, 1341 (2012).

[3] A. H. Castro Neto et al., Rev. Mod. Phys. 81, 109 (2009).

[4] J. Park, Y. H. Ahn, and C. Ruiz-Vargas, Nano Lett. 9, 1742 (2009).

[5] F. N. Xia et al., Nano Lett. 9, 1039 (2009).

[6] F. N. Xia et al., Nat. Nanotechnol. 4, 839 (2009).

[7] T. Mueller, F. N. A. Xia, and P. Avouris, Nat. Photonics 4, 297 (2010).

[8] C. H. Liu et al., ACS Nano 6, 7172 (2012).

[9] X. D. Xu et al., Nano Lett. 10, 562 (2010).

[10] N. M. Gabor et al., Science 334, 648 (2011).

[11] T. J. Echtermeyer et al., Nature Communications 2 (2011).

[12] Z. Fang et al., Nano Lett. 12, 3808 (2012).

[13] A. N. Grigorenko, M. Polini, and K. S. Novoselov, Nat. Photonics 6, 749 (2012).

[14] M. Furchi et al., Nano Lett. 12, 2773 (2012).

[15] M. Engel et al., Nature Communications 3 (2012).

[16] B. Y. Zhang et al., Nature Communications 4, 1811 (2013).

[17] M. Breusing, C. Ropers, and T. Elsaesser, Phys. Rev. Lett. 102, 086809 (2009).

[18] M. Freitag et al., Nat. Photonics 7, 53 (2013).

[19] M. W. Graham et al., Nat. Phys. 9, 103 (2013).

[20] G. Konstantatos et al., Nat. Nanotechnol. 7, 363 (2012).

[21] Z. Sun et al., Advanced Materials 24, 5878 (2012).

[22] G. Konstantatos, and E. H. Sargent, Nat. Nanotechnol. 5, 391 (2010).

[23] S. Lee, K. Lee, and Z. Zhong, Nano Lett. 10, 4702 (2010).

[24] S. Lee et al., Nanoscale 4, 639 (2012).

[25] P. Thissen et al., New Journal of Physics 12 (2010).

[26] X. Li et al., Advanced Materials 22, 2743 (2010).

[27] E. J. H. Lee et al., Nat. Nanotechnol. 3, 486 (2008).

[28] B. Radisavljevic et al., Nat. Nanotechnol. 6, 147 (2011).

[29] T. Georgiou et al., Nat. Nanotechnol. 8, 100 (2013).

Chapter 7

Conclusions

7.1 Summary

In summary, we have demonstrated novel carbon-based electronics and optoelectronics, which are based on our investigations into the fundamental properties of nanoscale junctions and interfaces.

In Chapter 4, we presented fully suspended carbon nanotube diodes with the split-gate geometry. By creating a p-n junction and a Schottky junction in carbon nanotubes with the gates, we have seen that *I-V* characteristics in forward and reverse bias regions are both gate-controllable. Furthermore, each single carbon nanotube device here could embody different diode concepts, such as p-n diode, tunneling diode and backward diode. This development would be important for the coming generation of integrated circuits, which require diverse functionalities, high packing density and low power consumption nanoelectronics.

In Chapter 5, we focused on characterizing hot carrier photoresponse at graphene p-n and graphene-metal Schottky junctions by using scanning photocurrent spectroscopy. Our studies revealed that photocurrent generation from these nanoscale junctions could be induced by different mechanisms, including the thermoelectric effect, photovoltaic effect and photo-Dember effect. Furthermore, we have seen that the dominant effect could be closely related to the laser

excitation power, intrinsic Fermi level and mobility of graphene devices. These fundamental investigations of the processes of converting light into electricity in graphene would provide the basis for developing graphene-based optoelectronics and ultrafast photonics.

Lastly, in Chapter 6, we performed novel photodetectors based on graphene double layer heterostructures. By exploiting hot carrier tunneling between graphene layers, we have seen that our proposed devices could demonstrate broad spectrum photodetection and high responsivity at room temperature, which are essential for varied scientific and technological applications.

7.2 Future work

Based on our works, it is also worth noting that new device structures, physics and operation principles could be opened up by exploiting 2D graphene. Therefore, the similar concepts demonstrated here might also be applied to other newly developed 2D graphene families, 2D chalcogenides or 2D oxides [1-2], and importantly, these 2D crystals might provide additional benefits for device applications.

For example, the asymmetry of electron-hole mobility is usually negligible in graphene. However, an intense lateral photo-Dember electric field can still be observed in graphene due to the spatial confinement of photocarriers in 2D and its low electronic heat capacity (chapter 5). Based on this observation, we can expect that a stronger photo-Dember electric field might be demonstrated in other 2D systems, which inherently have a strong light absorption coefficient and large electron-hole mobility asymmetry. This finding would be valuable for developing ultrafast terahertz emitters.

Another interesting direction is the construction of high-performance devices achieved by stacking different 2D crystals on top of each other. For instance, we utilized vertically stacked

graphene/Ta_2O_5/graphene and graphene/Si/graphene heterostructures to demonstrate broad spectrum and high responsivity photodetectors (chapter 6). From these devices, we found that having a thin and defect-free tunneling barrier is important for enhancing the hot carrier tunneling rate and device operation speed. Thus, it would be helpful to encapsulate an atomically-thick 2D crystal with an appropriate bandgap between two graphene layers. Additionally, if we replace the bottom graphene layer with other thin film semiconductor crystals, it is expected that the dark current of photodetectors could be reduced, which would be beneficial in improving the sensitivity and noise equivalent power. In short, the possibilities for combining different 2D crystals could expand dramatically, and such atomically thin heterostructures might represent a promising new class of devices.

References:

[1] A. K. Geim, and I. V. Grigorieva, Nature 499, 419 (2013).

[2] K. J. Koski, and Y. Cui, ACS Nano 7, 3739 (2013).